Variations on Acoustophoretic Microchannels: From the Facile to the Highly Capable

by

Champika Samarasekera

A thesis
presented to the University of Waterloo
in fulfillment of the
thesis requirement for the degree of
Doctor of Philosophy
in
Systems Design Engineering (Nanotechnology)

Waterloo, Ontario, Canada, 2018

Examining Committee Membership

The following served on the Examining Committee for this thesis. The decision of the Examining Committee is by majority vote.

External Examiner	CHRISTINE DÉMORÉ Scientist, Physical Sciences, Sunnybrook Research Institute Assistant Professor, Medical Biophysics, University of Toronto
Supervisor	JOHN T. W. YEOW Professor, Systems Design Engineering, University of Waterloo
Internal Member	GLENN HEPPLER Professor, Systems Design Engineering, University of Waterloo
Internal-external Member	SHIRLEY TANG Associate Professor, Chemistry, University of Waterloo
Internal-external Member	VIVEK MAHESHWARI Associate Professor, Chemistry, University of Waterloo
Internal-external Member	CHRISTOPHER J. BACKHOUSE Professor, Electrical and Computer Engineering, University of Waterloo

This thesis consists of material all of which I authored or co-authored: see Statement of Contributions included in the thesis. This is a true copy of the thesis, including any required final revisions, as accepted by my examiners.

I understand that my thesis may be made electronically available to the public.

Statement of Contributions

The acoustic simulations of the CMUT and CMUT-enabled microchannel presented in this thesis were performed, in part, by Jame Sun using the COMSOL Multiphysics software package and working under my direction and supervision as part of his undergraduate co-op term in the Department of Mechanical and Mechatronics Engineering.

Abstract

The lab-on-a-chip toolkit is replete with techniques for microparticle manipulation. The use of ultrasonic waves to impart forces on particles, referred to as acoustophoresis, is one particularly powerful yet gentle option. Traditionally, piezoelectric transducers have been coupled with acoustic resonators in order to sustain standing waves for aggregating, sorting, and sensing applications. However, there are several drawbacks to these setups. First, the construction techniques underpinning resonators tend to be expensive and laborious. Secondly, the acoustic impedance of piezoelectric transducers is much higher than the aqueous medium in which microparticles are suspended. This requires the use of impedance-matching layers to adequately couple acoustic energy into the medium. Finally, piezoelectric materials tend to be incompatible with traditional fabrication methods for microelectromechanical systems (MEMS). This can significantly impact the use of piezoelectric materials in more complex lab-on-a-chip type platforms where many processes beyond sample manipulation may be necessary.

Over the past two decades, another type of transducer, known as the capacitive micromachined ultrasonic transducer (CMUT), has been challenging the dominance of the piezotransducer. However, this competition has been occurring primarily in the arenas of non-destructive testing and medical imaging. Given some of the unique attributes of CMUTs, it is surprising that they have yet to be fully realized in acoustophoresis, especially because acoustophoresis is popularly practiced within a microfluidic setting.

We first present a highly cost-effective and cleanroom-free technique for prototyping piezo-equipped, transversal acoustophoretic resonators. Simple bifurcation and trifurcation microchannels suitable for acoustophoresis in microscopy applications are fabricated and demonstrated. The second focus of our research looks at the suitability of CMUT microarrays as platforms for acoustophoresis. We address the following: issues surrounding their implementation; modeling of potential resonator designs; and possibility of foregoing resonators altogether. Several CMUT devices are then fabricated and tested, using travelling-wave ultrasound to demonstrate aggregation within droplets as well as sequential capture and separation within flows. A unique phenomenon of bead aggregate palpation is encountered, the physical underpinnings of which are attributed to magnitude changes in lateral gradient forces with frequency. Finally, we attempt to perform standing wave manipulations of particles using the CMUT microarray, and describe the difficulties encountered in doing so.

Acknowledgements

Completing this thesis has not at all been a solitary affair, and I would like to recognize some of the people who have helped me in this process. First and foremost on this list, I would like to thank my supervisor Dr. John Yeow, who allowed me to pursue the questions I found most interesting, and showed incredible patience when they took longer than expected to bear fruit. I would also like to thank the other members of my committee, Dr. Christopher Backhouse, Dr. Christine Démoré, Dr. Glenn Heppler, Dr. Vivek Maheshwari, and Dr. Shirley Tang for generously sharing their time and expertise.

To the many current and former members and collaborators of the Advanced Micro-/Nano- Devices Lab, I have relied on you all throughout this endeavour, and I can only give my heartfelt thanks. To Zhenhao Li for demonstrating what it takes to be a conscientious researcher and educating me on denim. To Albert Chen for clarifying what was worth worrying about and what wasn't, then coming to my rescue when I mistook one for the other. To Shuai Na who had advice to provide when I came calling. To Lawrence Wong for answering my asinine CMUT questions. To Zhou Zheng who was always available when something had to be built, tested, or thought about. To Jame Sun who managed to wrangle solutions out of COMSOL time and again. To Limin Lu for giving me the chance to work on an interesting problem outside of CMUTs, and the pleasant conversations in between. To Chen Chen for sticking around even when I led him down dead ends. To Shruti Nambiar for sharing her hard earned knowledge on producing papers and little people in grad school. To Yunhan Li for keeping me company while handling corrosive substances. To Manu Pallapa for showing me around the lab and being so generous with his time. To Mehdi Shahini for getting me started on cutting things with lasers and hitting things with a dodgeball. To Yibei Zhao for keeping my spirits up when things seemed hopeless. To Morteza Ahmadi for explaining the finer points of a weekly report. To Mohamed Aly Saad for telling it like it was. To Siyuan Chen, Mingyu Zhang, and Fred Sun for their good humor in the lab. To Ibrahim Ben Daya of the VIP Group for attempting to tame the machine with me. Finally, to the eminently quotable Leon Mintz, whose insight and friendship made all the difference.

Absolutely none of this would have happened without the love and sacrifice of my mother and father. I am blessed beyond reason to have parents who have believed in and supported me in all my endeavors. To my mother for making sure I come out of situations stronger than when I went in. To my father for teaching me to do the best job possible. To my sister, solver of problems, tamer of egos, and the best sanity check I could have asked for. I have come to believe that truly anything is possible with the three of you in my corner.

To Tara, my partner in every sense of the word. To call your efforts heroic would be an understatement. When this all started you just had to deal with a neurotic graduate student and his dog. A twin pregnancy later, I find myself in awe of your ability to laugh through the tears. Thank you for putting up with the very silly boys in your life, we promise we're worth it.

Dedication

This is dedicated to the generations I find myself between; my parents who encouraged me to ask questions, and my children who will find their own.

Table of Contents

List of Tables

List of Figures

"Would you tell me, please, which way I ought to go from here?"
"That depends a good deal on where you want to get to," said the Cat.
"I don't much care where-" said Alice.
"Then it doesn't matter which way you go," said the Cat."
"-so long as I get SOMEWHERE." Alice added as an explanation.
"Oh, you're sure to do that," said the Cat, "if you only walk long enough."

-Alice's Adventures in Wonderland, Chapter 6

"We must walk in a city of CMUTs"

-L. Mintz

Chapter 1

Introduction

1.1 Motivations

The use of sound to manipulate particles, or acoustophoresis, is a well established technique. The notion that particles in a sound field experience radiation forces has been known since the last half of the 19th century [2]. However, the systematic theoretical development and observation of acoustophoresis began in the 1930s [3, 4]; while the use of higher, MHz, sound frequencies saw acoustophoresis gain adherents among the Lab-on-a-chip community in the early 90s [5, 6]. A cursory examination of the physics involved makes it easy to see why that is. The ultrasonic regime within which acoustophoresis is implemented is ideal for pairing with microfluidics. Furthermore, the gentle, non-contact forces that ultrasound energy can impart is perfectly suited for work with cells and other delicate particles.

The most popular method for generating ultrasound has been, and continues to be, through the use of piezoelectric substrates, these transducers are coupled to acoustic resonators. Resonators have typically been fabricated using microelectromechanical system (MEMS) techniques; unfortunately, such techniques can be prohibitively expensive and require laborious processing methods.

A different source for ultrasound energy is the capacitive microcmachined ultrasonic transducer (CMUT). These devices were originally introduced in the mid 90s and quickly found use in non-destructive testing (NDT) applications [7, 8]. While CMUTs have continued to find use in medical imaging their use in microfluidic applications has been lacking. Indeed, our group has been developing CMUTs for NDT and catheter based biomedical imaging applications for several years.

Thus the motivations behind this thesis were twofold. First, it was deemed that an approach that could drastically simplify the fabrication and prototyping of conventional piezo-equipped acoustic resonators would provide value to researchers and those looking to implement acoustophoretic technology into the broader market. This would also allow the author to become familiar with the limitations of current piezo-equipped acoustophoretic setups. Second, we wished to investigate the use of CMUTs in acoustophoresis. This specific thrust of research seeks to answer the following questions: Why have CMUTs not found their way into acoustophoretic resonators and what are some of the unique characteristics of CMUTs that can be exploited for use in acoustophoresis?

1.2 Contributions

The main contribution of this thesis is the design and implementation of CMUT microarrays in acoustophoretic devices. In so doing, we have identified several unique methods of particle manipulation, previously unreported in acoustophoresis with piezotransducers, and attempted to explain their mechanism. A secondary contribution is a simplified fabrication method for traditional, piezotransducer-equipped, microchannel resonators. Although ultrasound experience within the Advanced Micro/Nano- Devices Lab has grown over the last 12 years, all of it has been in imaging and non-destructive testing applications. Thus, a final contribution of this thesis is to provide an introduction to current and future lab members interested in ultrasonic particle manipulation.

1.3 Thesis Outline

This thesis is presented to the reader in five chapters. Chapter 2 provides contextual information on acoustophoresis and competing methods in non-contact particle manipulation. This is followed by the relevant background in the mechanics of ultrasound as it relates to: particles in a fluid, methods of generation, and the structures typically encountered in acoustophoresis. We also introduce the technology of CMUTs and the basics of transducer array operation.

In Chapter 3 we present a facile fabrication method for acoustophoretic resonators. A pair of resonator designs are tested and observations on their performance are provided. A paper related to this chapter has been previously published as

- C. Samarasekera and J. T. W. Yeow, "Facile microfluidic channels for acoustophoresis on a budget" Biomedical Microdevices, DOI: 10.1007/s10544-015-0006-2

Chapter 4 describes the design, simulation, fabrication, and testing of a CMUT device for both droplet and microfluidic acoustophoresis. Experiments show heretofore unreported acoustophoretic manipulations and explain their possible mechanisms. A paper related to this chapter has been submitted for publication in *Sensors and Actuators B* and is currently undergoing peer review.

The final chapter summarizes the results of this thesis and proposes future avenues of exploration.

Chapter 2

Background

2.1 Non-contact particle manipulation

The physical manipulation of cells and particles is an important step that occurs frequently in biological and industrial settings. Using direct, physical contact to manipulate microparticles has significant disadvantages such as contamination transfer, target vitiation, and inefficient management at high sample populations. With the advent of microfluidics, where fluid samples are confined to the micrometer regime, the sample volumes being processed can determine whether continuous (flow) or batch (droplet) processes are implemented. In either case, today's researcher has a suite of non-contact manipulation methods to choose from, all of which rely on externally-applied fields to induce forces on particles. These forces drive particles to the spatial locations where potential energy is at a minimum. The fields used can be magnetic, electrical, optical, or acoustic. These non-contact techniques have been widely applied to separate, enrich, and precisely transport cells and biomolecules to pre-defined locations. Each method has advantages and disadvantages, and oftentimes techniques are combined to leverage the former and minimize the latter. In this section we will give a brief overview of the first three non-contact methods mentioned, followed in the next section by a much deeper dive into acoustophoresis, the focus of this thesis.

2.1.1 Magnetophoresis

The conventional application of magnets in particle separation requires that the object of interest be attracted to or repulsed by the presence of an external magnetic field. When

a magnetic field causes particles to experience a weak attractive force, they are said to be paramagnetic. However, very few cells are paramagnetic, thus most targets are labeled with paramagnetic particles before they can be manipulated [9]. Likewise, the inherent properties of the target do not play a direct role in their manipulation. Conversely, diamagnetism is the ability of a material to produce a magnetic field that is directly opposed to an externally-applied magnetic field. Most particles and biomolecules experience an extremely weak repulsive force in magnetic fields. To amplify the phenomena to observable levels, paramagnetic salts are introduced to the fluid that the particles or cells are suspended in [10, 11]. As is the caveat when adding anything into solution, the possible interactions of the paramagnetic salts with downstream processes may require their prior removal.

2.1.2 Dielectrophoresis

When polarized particles are introduced to a non-uniform electric field, they experience a force that propels them toward either the stronger or weaker field regions. This effect was first studied by Pohl in 1951, and he coined the phenomenon dielectrophoresis [12]. The direction of the force depends on the polarizability of the particle compared to the conductivity of the medium. Hence the terms *positive* and *negative* dielectrophoresis, where particles may be attracted to or repulsed by the high field region. Dielectrophoresis offers impressive spatial precision, and various arrangements of electrodes have been used to separate, aggregate, and even rotate trapped particles [13, 14, 15]. The high field gradients required for this technique has necessitated a trend toward both smaller electrodes and intra-electrode spacing, the advantage being lower voltage requirements. This, in turn, reduces the Joule heating effect of the particle medium, which can otherwise result in damage to samples [16]. An unfortunate side effect of metal electrodes, however, is electrolysis, which generates gas bubbles in the fluid. Moreover, the electric fields typically encountered in dielectrophoresis have been shown to adversely impact cells [17].

2.1.3 Optical Trapping

Within a decade of the invention of the laser, Ashkin showed that highly focused beams of light could exert two types of forces on small particles [18]: first, a scattering force that pushes the particle in the beam propagation direction; and second, a gradient force that acts in the direction of the intensity field gradient of the beam. The maturation of this technology has evolved from single-beam traps (so-called optical tweezers) working on

single targets to three-dimensional optical lattices operating on multiple targets [19, 20]. The advantages enjoyed by optical trapping include an ability to operate on very small (nm-sized) particles, and to do so with high-degrees of spatial precision. However, the instrumentation required for optical trapping is quite complicated and expensive, making it difficult to simultaneously miniaturize and integrate with microfluidic systems. Also, particle concentrations in optical traps are typically kept intentionally low in order to prevent blockages. Finally, due to the lasers involved, considerable care must be taken around chosen targets since optical damage and thermal heating are possibilities [21, 22]. As an aside, the term 'optophoresis' does not appear to have caught on for this technique, possibly because of a trademarking of the term by a private company in the early 2000s, which has since been abandoned [23, 24].

2.2 Acoustophoresis

Derived from a rather artful combination of the Greek words for hearing, *akoustikós*, and carrying, *foríseos*, acoustophoresis refers to the movement of particles in a medium through the force of sound. Sound is itself the oscillation of the molecules that constitute a medium. Consequently, when these moving molecules come into contact with other particles existing in that same media, they impart a force. Much like its counterpart, optical trapping, the force experienced by a particle in a sound field may be split into a scattering force and a gradient force.

Acoustophoresis as it is practiced today typically employs sound frequencies well beyond the range of human hearing, in the ultrasound regime from one to tens of MHz. Instances of ultrasound being utilized to manipulate particles first appear in the 1930s for moving electrolytic ions in solution [25] and in the creation of coagulants within emulsions [4]. However, from the evidence this author could gather, the term acoustophoresis was not coined until a half-century later by Pen Kem, Inc., when they developed the first commercial electroacoustic instrument for colloids [26, 27].

The *mode du jour* for acoustophoresis is in continuous flow-based systems where particles of interest can be separated within [28], or even trapped against [29], a microfluidic flow. Briefly, when an ultrasound field is introduced to particles in solution, the acoustic waves scatter off the particles, pushing particles in the direction of beam propagation; in acoustic fields with non-uniform intensity distributions, a particle will experience a gradient force that is dependent on several material properties of the particle [30]. In this manner, high frequency, standing-wave ultrasound can be used to separate particles by their physical attributes, such as size [31], density [32], and compressibility [28]. A typical

continuous flow acoustophoresis setup is shown in Figure 2.1. In this example, a suspension of identical particles are introduced to a microchannel. As the particles encounter the ultrasound field, they are driven to the single node of the standing wave at the center of the trifurcating channel.

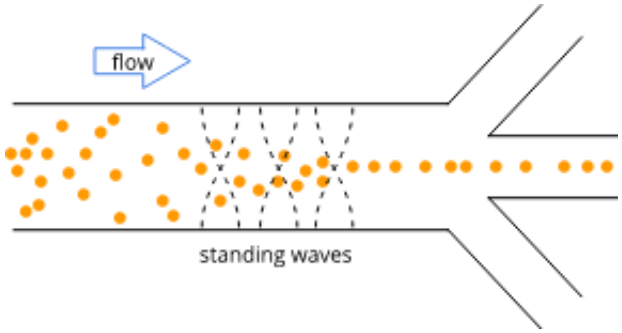

Figure 2.1: A schematic of an acoustophoretic trifurcating microchannel, where particles are driven to the center of a standing wave (dashed lines)

Components common to almost all acoustophoresis setups are the transducers that produce ultrasound energy and the acoustic resonators that enable the establishment of a standing wave. We shall examine these two important elements in further detail and review the essential physics involved.

2.3 Ultrasound

Sound is the mechanical propagation of a wave by the vibrating molecules of some medium. Sound waves outside of the realm of human hearing is what we generally mean when referring to ultrasound. Recall that the fundamental equation of all wave motions can be given by,

$$c = \lambda f \tag{2.1}$$

where c is the speed of the wave in the medium it is travelling, λ is the wavelength, and f is the frequency.

When a transducer of finite dimensions is used to generate sound waves, it can be thought to behave exactly like an aperture through which a plane wave passing will diffract. In the region close to the transducer, referred to as the nearfield, the diffracting wave will

result in substantial phase shifts between sound pressure and velocity. As the wave travels away from the transducer and into the farfield region, these phase differences disappear and the sound pressure level once again obeys the inverse square law. The transition point between nearfield to farfield for a circular transducer of radius, r, is [33],

$$Z_t = \frac{r^2}{\lambda} \tag{2.2}$$

At this transition point, the acoustic beam width minimizes and pressure maximizes, thus Z_t is also called the natural focus.

The commercial application of ultrasound is as varied as the range of frequencies it encompasses. At the lower frequency end (20 kHz), ultrasound can be used to create well-controlled ice crystals, and inactivate bacterial spores for food preservation, or in hastening the low-solvent extraction of food components such as pigments, essential oils, and other compounds [34]. At the middle to higher frequencies (hundreds of kHz to tens of MHz) medical ultrasound for use in diagnostics and therapy has been steadily established over many decades; becoming a key modality in the medical fields of cardiology, oncology, and nephrology [35, 36, 37]. Ultrasound has been widely popularized through its use in obstetrics, where it is standard practice for pregnant mothers in developed nations to be offered routine ultrasound exams [38]. We, however, are interested in the use of ultrasound to physically manipulate particles. This begins with an understanding of how a particle behaves in a sound field.

2.3.1 Acoustic forces

As stated earlier, there are striking similarities between optical and acoustic manipulation techniques. Both techniques involve radiation forces through momentum transfer and also gradient forces caused by variations in field intensity. The literature in optical manipulation has sometimes referred to both types of forces interchangeably [39]. Regrettably, this confusion has also occurred within acoustophoresis; such that researchers have come to use the term acoustic radiation force when describing acoustic gradient forces or a combination of both radiation and gradient forces. In an attempt at accuracy, we shall refer to acoustic radiation forces as those caused by wave scattering, and acoustic gradient forces as those caused by variations in the potential and kinetic energy of the acoustic field. This Thesis concerns the use of acoustic gradient forces, thus we shall provide an introduction to them.

The strength of the gradient force and direction of particle movement depend on the parameters of the sound field, and the relative properties of both the particles being ma-

nipulated and the medium the particles are suspended in. The theory presented in both this section and the next is based on the thorough treatment by Bruus [30] who followed the general summary of work in the field provided by Gor'kov [40]. The most general form of the acoustic gradient force, F_{grad}, acting on a spherical particle can be given by the gradient of an acoustic potential, U,

$$F_{grad} = -\nabla U \tag{2.3}$$

where

$$U = \left(\frac{4\pi a^3}{3}\right)\left(b_1 \frac{\langle p_1^2 \rangle}{2\rho_m c_m^2} - b_2 \frac{3}{4}\rho_m \langle v_1^2 \rangle\right) \tag{2.4}$$

where a is the particle radius, ρ_m is the density of the medium, c_m is the speed of sound in the medium, p_1 is the pressure field, and v_1 is the velocity field. The terms b_1 and b_2 are monopole and dipole coefficients and come from treating the particle as a point-scatterer. These coefficients may be described as

$$b_1 = 1 - \frac{\rho_m c_m^2}{\rho_p c_p^2} \tag{2.5}$$

$$b_2 = 2\frac{\rho_p - \rho_m}{2\rho_p + \rho_m} \tag{2.6}$$

where ρ_p and c_p are the density of and the speed of sound in the particle respectively.

2.3.2 Standing wave

When acoustic standing waves are generated, a particle in the field is driven to the locations of lowest pressure variation (nodes), or of highest pressure variation (anti-nodes). The number of nodes depends on the distance between the resonator surfaces, d, and the resonance mode, N, present in the system. The acoustic frequencies at which these modes occur can be given by,

$$f_N = \frac{N c_m}{2d} \tag{2.7}$$

In acoustophoresis, one of the most commonly encountered setups is the special case of the 1-D planar standing $\lambda/2$ acoustic wave (see Figure 2.2) for which the acoustic potential can be expressed as,

$$U = \left(\frac{\pi a^3 p_a^2}{\rho_m c_m^2}\right)\left(\frac{b_1}{3}cos^2(kz) - \frac{b_2}{2}sin^2(kz)\right) \tag{2.8}$$

which can be differentiated to give a gradient force,

$$F_{grad_z} = 4\pi a^3 E_{ac} k \sin(2kz)\phi \tag{2.9}$$

where E_{ac} is the acoustic energy density, k is the wavenumber, z is the distance from the anti-node in the wave propagation axis, and ϕ is the acoustic contrast factor. The acoustic energy density is given by,

$$E_{ac} = \frac{p_a^2}{4\rho_m c_m^2} \tag{2.10}$$

where p_a is the maximum acoustic pressure. The wavenumber is simply,

$$k = \frac{2\pi f}{c_m} \tag{2.11}$$

where f is the frequency. The acoustic contrast factor determines the sign of the gradient force and can be given as,

$$\phi = \frac{\rho_p + \frac{2}{3}(\rho_p - \rho_m)}{2\rho_p + \rho_m} - \frac{1}{3}\frac{\rho_m c_m^2}{\rho_p c_p^2} \tag{2.12}$$

such that when ϕ is positive the particle will move towards the pressure node and when ϕ is negative the particle will move toward the pressure anti-node.

It must be pointed out that the equations thus far discussed are for a single particle and do not take into account any effects due to the interactions between multiple particles.

2.3.3 Bjerknes force

The scattered sound field due to one particle will influence other particles that are also present in a fluid. This results in a Bjerknes force, also called a secondary radiation force. Weiser and Apfel showed that, for particles separated by a distance, d_p, much smaller than the acoustic wavelength, the force between two spheres of equal radius depends on the angle

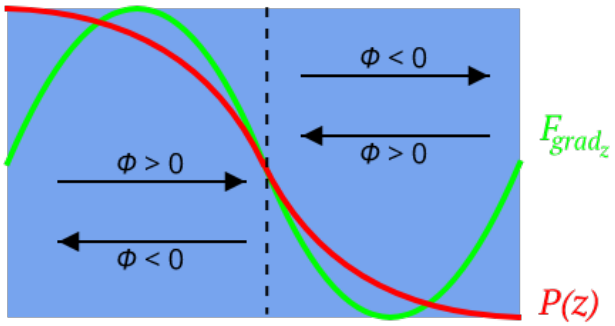

Figure 2.2: Cross-section of a $\lambda/2$ resonator where F_{grad_z} will move particles toward the pressure node plane (dashed black line) when ϕ is positive and away from the node when ϕ is negative

formed between a straight line connecting the particles and the propagation direction of the sound field. Such that the force between particles oriented with the sound field is [41],

$$F_B = \frac{4\pi(\rho_p - \rho_m)^2 v^2 a^6}{3\rho_m d_p^4} \tag{2.13}$$

and for particles perpendicular to the sound field by,

$$F_B = -\frac{2\pi(\rho_p - \rho_m)^2 v^2 a^6}{3\rho_m d_p^4} \tag{2.14}$$

where a negative force is attractive and v is the velocity of the incident acoustic wave at the location of the particles. In the $\lambda/2$ resonator example we have been using, the particles will gather to the node or anti-node locations relatively quickly. Thus the resulting effect of Bjerknes forces should be the creation of stable, tight clusters of particles along the node or anti-node [42]. However, the Bjerknes force is weaker and acts on much shorter distances than the gradient force.

2.3.4 Acoustic streaming

The phenomenon of acoustic streaming can be a boon or hindrance in acoustophoretic settings. Poor design choices can create streaming situations that disrupt desired particle manipulations but with careful consideration, acoustic streaming can be used for mixing,

and aggregating, applications [43, 44]. Streaming can be classified into several different types but it is generally understood to be a fluid flow resulting from the attenuation of an acoustic wave. The velocity, length, and shape of this flow depend on the mechanism behind the acoustic attenuation. The first type of streaming we will consider occurs when acoustic energy is lost through viscous dissipation along a solid boundary. This results in so-called Schlichting streaming where, in the case of standing waves, a vortex is formed between the pressure node and anti-node locations that is confined to the viscous layer formed by the fluid and a wall for instance. The size of this layer is given by [45],

$$\delta_v = \sqrt{\frac{\eta}{\pi f}} \tag{2.15}$$

where η is the dynamic viscosity of the medium.

Vortices can also develop in the bulk of the fluid and is given a different term, Rayleigh streaming (see Figure 2.3a). The underlying mechanism of Rayleigh streaming is believed to be a response to Schlichting vortices [46]. However, given the tiny length scales of Schlichting streaming in comparison to Rayleigh streaming, many acoustophoretic researchers ignore the former altogether.

Finally, the attenuation of acoustic energy as it travels through a fluid medium can cause Eckart streaming. The steadily decreasing energy of the acoustic beam is converted into a fluid flow travelling in the same direction. When this jet is confined to a microfluidic cavity vortices can form (see Figure 2.3b). Thus, significant Eckart streaming will only occur when the frequency of ultrasound is sufficiently high and propagates along a device dimension equal to or greater than the acoustic attenuation length (i.e. much longer than the wavelength of ultrasound in the fluid). This makes maximizing or minimizing Eckart streaming a fairly simple resonator design exercise.

2.3.5 Focused beam ultrasound

The formation of planar standing waves, while a popular option, are not the only method utilized in acoustophoresis. Focused sound beams are often used to levitate and trap objects [47, 48]. Focusing of the beams is accomplished by the use of an acoustic lens or by fabricating curved transducers. Typically, two opposing ultrasonic transducers are used to create a potential well between them. The main advantage over planar standing waves being that the spatial dimensions of the potential well can be larger; a useful feature for containerless transport and processing applications. A newer development has been the

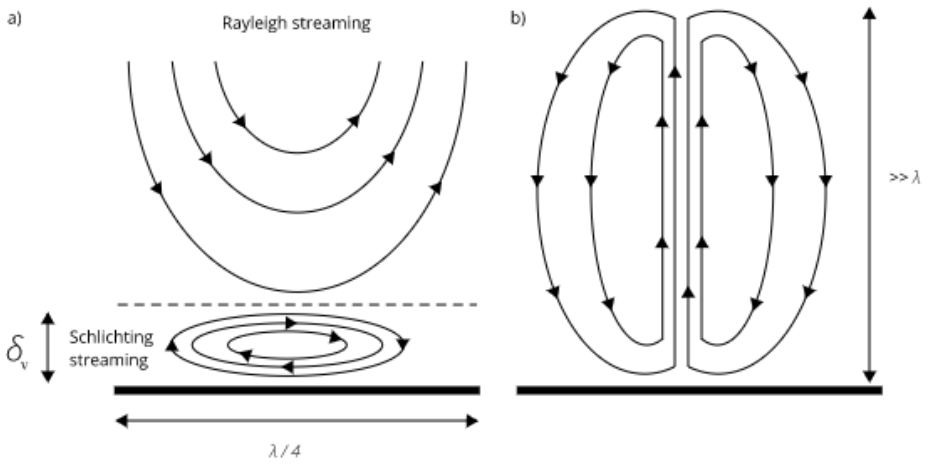

Figure 2.3: A schematic of a) Schlichting and Rayleigh streaming regimes, with the viscous boundary layer, δ_v, forming between the heavy and dashed lines; b) Eckart streaming

single beam trap [49, 50]. While the dual beam technique works in the Rayleigh regime ($a \ll \lambda$), the single beam operates in the ray acoustics regime ($\lambda \ll a$) thus requiring very high frequencies in order to manipulate microparticles. Another interesting focused beam solution is the creation of quasi-standing waves. Here a curved transducer transmits a beam towards a reflector that is placed at the focal point [51]. Microparticles at the focus would experience radiation and gradient forces. Thus, lateral movements of the transducer would then move particles that were trapped to the focal point.

2.3.6 Particle considerations

As Equation 2.9 shows, the gradient force experienced by a particle in a resonator is proportional to the particle radius cubed (i.e. particle volume). Thus, larger particles will require lower operating frequencies than smaller particles to experience the same gradient force. The lower limit of particle size for acoustic gradient forces is around a micron, below which, acoustic streaming effects can dominate. On the opposite end, larger particles begin to deposit as sediment due to gravity. This typically becomes a concern for particles beyond 10 μm in radius but is clearly dependent on the buoyancy of a particle. The timescales for sedimentation can be found by [52],

$$\tau_{sed} = \frac{9\eta h}{2(\rho_p - \rho_m)a^2 g} \tag{2.16}$$

where h is the vertical distance travelled by the particle (i.e. the height of the microchannel), and g is the acceleration due to gravity. To run acoustophoretic experiments longer than the sedimentation time would require counteracting the force of gravity, perhaps with a standing wave such that,

$$F_{grad} = \frac{4\pi a^3}{3}(\rho_p - \rho_m)g \tag{2.17}$$

When designing a microfluidic system for acoustophoresis, knowing how quickly or by how much particles will separate dictates overall channel lengths and the locations of junctions where the flow can be diverged. The position dependent velocity of a particle, v_p, can be determined by balancing the acoustic gradient force with the viscous Stokes drag force ($6\pi\eta a v_p$) to yield,

$$v_p(z) = \frac{2\phi k a^2 E_{ac}}{3\eta}\sin(2kz) \tag{2.18}$$

Alternatively, via integration, an expression for the time to move a particle from some initial position, z_0, to another position, z, can be found,

$$t = \frac{3\eta}{4\phi(ka)^2 E_{ac}}\ln\left[\frac{\tan(kz)}{\tan(kz_0)}\right] \tag{2.19}$$

where both z_0 and z must lie within a sequential node and anti-node.

Additionally it may be possible to use acoustophoretic forces to trap particles against the flow of a fluid. The direction of fluid flow may be parallel or perpendicular to the direction of ultrasound propagation [53, 29]. In either case, however, the trapping force acts in the opposite direction of the viscous drag force acting on the particle such that Stoke's law yields,

$$F_{trap} = 6\pi\eta a v_m \tag{2.20}$$

where v_m is the velocity of the medium relative to the particle.

2.4 Transducers

Commercially, the creation of ultrasonic waves involve the transduction of electrical energy into mechanical energy. Generally, ultrasound transducers operate at a defined frequency where a resonant mode is established and maximum acoustic energy is produced.

2.4.1 Piezoelectrics

Ultrasound transducers come in a few flavours but those most commonly encountered in acoustophoresis, and indeed most applications involving ultrasound, operate on the piezoelectric effect (PE). This phenomenon, first observed in crystals by the brothers Curie [54], is the generation of an electrical potential across a material that is undergoing some mechanical stress. This effect is reversible, such that if an AC voltage is applied to a piezoelectric crystal the resulting deformations can produce vibrations at an ultrasonic frequency. It wasn't until over a quarter century after its discovery, during the First World War, that PE found an application in sonar submarine detection [55].

Piezoelectric transducers can be made from single crystal materials like quartz, where the PE occurs naturally; they are far more likely today, however, to be made from polycrystalline materials such as lead zirconate titanate (PZT) where the PE is prompted by ferroelectric polarization [56]. Lead is usually a material that is regulated by the guidelines set forth in the Restriction of Hazardous Substances (RoHS). Despite this, and because there have been no comparably performing lead-free substitutes, PZT is granted an exemption from RoHS. There are bulk ceramic and film deposited PZTs; the former are cumbersome in microfabrication applications, but the latter may be deposited in micrometer layer thicknesses. Unfortunately, PZT can still be difficult to incorporate into some settings where issues of compatibility arise with materials or processes such as complementary metal-oxide-semiconductor (CMOS). Substrates used in CMOS cannot be heated beyond 600°C without incurring damage to circuitry, whereas deposition processes for PZT, such as sol-gel, routinely exceed this temperature threshold [57]. Furthermore, the thermal output of the transducer becomes a concern if operated continuously, since exceeding the Curie temperature of a polycrystalline piezo will disrupt polarization and lead to a loss of the PE.

The typical piezoelectric transducer design has a piezomaterial sandwiched between electrodes (see Figure 2.4) Here, the fundamental resonance frequency of a piezotransducer is defined by the thickness of the piezomaterial. Contact between the transducer and the

surface of the target is via a coupling material. This is done in order to increase the amount of acoustic energy delivered, an important point that will be discussed in more detail later.

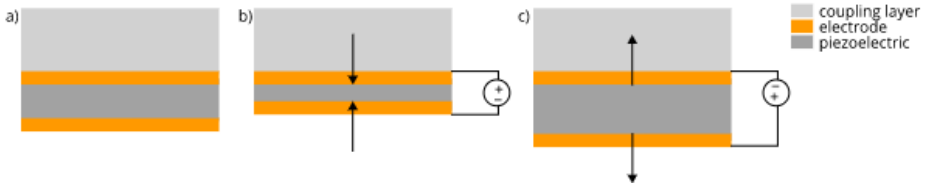

Figure 2.4: A typical piezoelectric layout showing a cross section view of a mounted element a) before activation; undergoing displacement through b) compression; and c) tension when an alternating electrical voltage is applied

2.4.2 Capacitive micromachined ultrasonic transducers (CMUTs)

Unlike piezos, CMUTs do not work on the PE. In essence, a CMUT is a biased parallel plate capacitor where one of the plates is flexible (see Figure 2.5a). There are two modes of operation in such a device, the transmit mode where a driving voltage can produce a deflection of the flexible plate (which is usually referred to as the membrane) and conversely, the receive mode in which membrane deflections generate current [8]. Due to the nature of this work, we will be concerning ourselves primarily with the transmit mode.

Capacitive transducers were difficult to implement in the ultrasonic regime because of the immense, $MV \cdot cm^{-1}$ scale, electric fields required to electrostatically move a plate. The breakdown voltage threshold in air is 30 $kV \cdot cm^{-1}$, thus conductive arcs will form between capacitor plates. However, the last two decades of micromachining techniques pioneered by the integrated circuit (IC) industry have changed this. Now, it is possible to manufacture capacitors with extremely small distances between the plates. As the distance between plates decreases, larger electric fields can be withstood [58]. The membrane on a typical CMUT unit might have a diameter as small as 10 μm with a gap height of a few hundreds of angstroms. The shape and size of the membrane determines its frequency response.

A single membrane and plate pair is called a cell. Due to their small membrane diameters, several simultaneously operating cells must be grouped into elements in order to produce any functional acoustic pressure. Within an element, the center-to-center distance from one cell to its neighbour is called the pitch. To increase the acoustic pressure output, an element's active cell area must be comparable to the total element area. The ratio of the former to the latter is known as the fill-factor, and this is clearly related to both the

shape of a membrane and pitch. Individually addressable elements can be further grouped into arrays (see Figure 2.5d). It is this collection of arrays that is typically called a CMUT. The microfabrication processes used to create a single cell are easily scalable to produce elements and arrays.

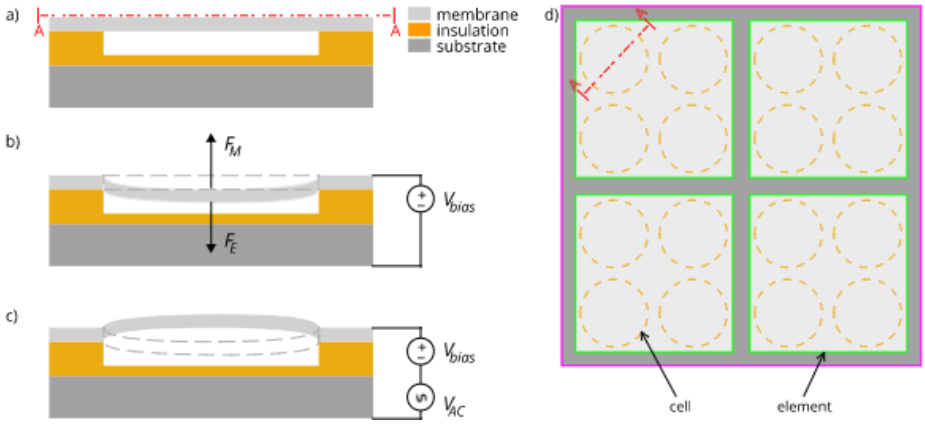

Figure 2.5: A typical layout showing a) a cross section view of the parallel plate capacitor underpinnings of a CMUT cell; b) the application of bias voltage and subsequent membrane deflection; c) the application of driving voltage and resulting membrane oscillation; and d) the top-down view of a 2D CMUT array featuring four cells per element and a 2x2 layout of elements in the array

Furthermore, because the materials and processing tools are shared between them, packaging CMUTs into larger IC devices is fairly trivial. For example, the CMUT-on-CMOS process allows parallel fabrication of both CMUTs and CMOS [59]. Or seperately fabricated CMUTs and CMOS can be integrated through flip-chip assembly [60]. Additionally, CMUTs can also be fabricated atop CMOS devices [61].

CMUT operation

During transmit operation, voltage is applied to the CMUT in two parts. First a DC bias voltage creates a static plate deflection pulling the membrane toward the substrate, as shown in Figure 2.5b. A first-order approximation of this electrostatic force, F_E, that treats the membrane like a moving piston yields [62],

$$F_E = \frac{\epsilon_0 A V_{bias}^2}{2(d_{eq} - x)^2} \tag{2.21}$$

where ϵ_0 is the permittivity of free space, A is the electrode area, V_{bias} is the DC voltage, d_{eq} is the spacing between the electrodes (such that multiple dielectric layers may be accounted for), and x is the membrane displacement. The electrostatic force is countered by the membrane's mechanical restoring force, F_M, where treating the membrane as a spring with a spring constant, k, gives

$$F_M = kx \tag{2.22}$$

Raising the bias voltage increases the sensitivity and efficiency of the CMUT when transmitting ultrasonic pulses [62]. A relationship between the bias voltage and membrane displacement is easily found by equating 2.21 and 2.22

$$V_{bias} = \sqrt{\frac{2kx}{A\epsilon_0}}(d_{eq} - x) \tag{2.23}$$

However, if the bias voltage is too large, the restoring force may be overcome and the membrane can collapse on to the substrate. By taking the derivative of 2.23 with respect to x and setting it to zero we find the collapse occurs at $x = d_{eq}/3$. Hence, in most cases, CMUTs are operated at a bias voltage that is near its collapse voltage, V_c, such that,

$$V_c = \sqrt{\frac{8kd_{eq}^3}{27A\epsilon_0}} \tag{2.24}$$

A second, AC voltage, signal is then used to excite the flexible plate (see Figure 2.5c). Since the electrostatic force generated on the plates of a capacitor is proportional to the square of the applied voltage, an AC voltage applied on its own would result in the transducer operating at double the applied frequency. Therefore, the DC bias voltage must be larger than the amplitude of the driving AC voltage in order to polarize the transducer and ensure a properly linear operation of the CMUT. The magnitude of the DC bias can play a part in the resonant frequency, f_0, of a CMUT cell. To understand how, we first recall that a resonating system is a function of its mass and spring stiffness, such that [63],

$$f_0 = \frac{1}{2\pi}\sqrt{\frac{k_{eff}}{m_{eff}}} \tag{2.25}$$

where k_{eff} is the effective spring constant of the membrane and m_{eff} is the effective mass. There are two contributors to k_{eff}, the mechanical stiffness, k_m, and the electrical stiffness, k_e, and for circular membranes [64],

$$k_m = \frac{16\pi E t^3}{(1-\nu^2)a_{mem}^2} \tag{2.26}$$

$$k_e = -\frac{\epsilon_0 V_{bias}^2 \pi a_{mem}^2}{2d_{eq}^3} \tag{2.27}$$

where E, ν, and a_{mem} are, respectively, the Young's modulus, Poisson constant, and radius of the membrane material. It is important to note that 2.27 is negative, thus the application of a bias voltage weakens k_{eff} and this phenomenon is referred to as the spring softening effect. For a circular membrane the effective mass is given by [64],

$$m_{eff} = 1.84\pi\rho t a_{mem}^2 \tag{2.28}$$

where ρ and t are the density and thickness of the membrane, respectively.

As the CMUT membrane approaches its resonant frequency, the amplitude of its oscillations increase. At f_0 the membrane reaches maximum amplitude. The magnitude of this amplitude and the oscillatory response depend on the energy lost due to damping. Generally, three damping sources exist. First, energy may be lost to the medium the membrane operates in. Second, the energy can be lost to the solid substrate that the membrane is coupled to. Finally, energy may be lost within the membrane material itself. The level of damping present in a resonant system can be represented by the quality factor (or Q-factor) of the device. Defined as the ratio of f_0, of a resonator to its bandwidth, Δf,

$$Q = \frac{f_0}{\Delta f} \tag{2.29}$$

The bandwidth is the frequency range bounded by a 3 dB drop in maximum amplitude. The higher the Q-factor the greater the amplification of resonance and narrower the band of frequencies will be at which resonance occurs. Typically, the largest of the three damping sources is the operating medium where the medium's molecules collide with the vibrating membrane. The loss due to this momentum exchange is proportional to the pressure of the medium. Thus, CMUTs operating in air will have a higher Q-factor ($\sim 10^2$) than those that are immersed in water ($\sim 10^1$) [65, 62]. Generally, CMUT devices have much wider bandwidths than their piezotransducer counterparts. This increased bandwidth can be exploited to increase the resolution of ultrasound images and enable other modalities such as harmonic imaging [66].

CMUT limitations

Of course, CMUTs are not a simple panacea for all our ultrasound needs. There exist several issues that limit CMUT operation. For example, a thin and flexible CMUT membrane cannot transfer energy into solid materials directly. This is related to the larger issue of acoustic impedance and will be covered later in this chapter. Another problem is the phenomenon of crosstalk [67]. When a CMUT element is activated, energy can be coupled to neighbouring elements and create spurious signals. The CMUT membrane undergoes stresses during deflection, and as was mentioned before, many CMUT cells are required to produce effective levels of acoustic power. Thus, fabricated CMUT arrays must be robust lest they fail during operation. Another way to increase the output power of CMUTs is by operating at higher DC bias and AC driving voltage. However, eventually a voltage threshold will be reached where the insulating layer separating the two plates of a CMUT is subject to dielectric breakdown. Closely related to this, is the dielectric charging effect, in which charges can begin to accumulate within the dielectric layer and degrade CMUT performance [68].

CMUT fabrication

Often it is one of two technologies that underpin the construction of a CMUT, they are either sacrificial release or wafer bonding. The former, illustrated in Figure 2.6, is a bottom up approach where the insulator, cavity, and membrane layers are deposited sequentially onto a silicon wafer and the membrane is released by etching the sacrificial layer that forms the cavity via etch holes [8]. The drawbacks to this fabrication technique center around the presence of the etch holes, which can negatively impact membrane uniformity, cavity sealing, and the overall output pressure of the device since the holes take up valuable transducer surface area. Alternatively, wafer bonding methods such as, high temperature fusion and, more CMOS-friendly, anodic bonding allow the cavity and membrane layers to be fabricated on separate substrates (see Figure 2.7) [69, 70]. The advantage here is that the shape and dimensions of the cavity are not encumbered by the requirements for a typical etch release process. Thus, cavities can be far shallower resulting in lower membrane actuation voltages and furthermore, potentially reducing the number of lithography steps.

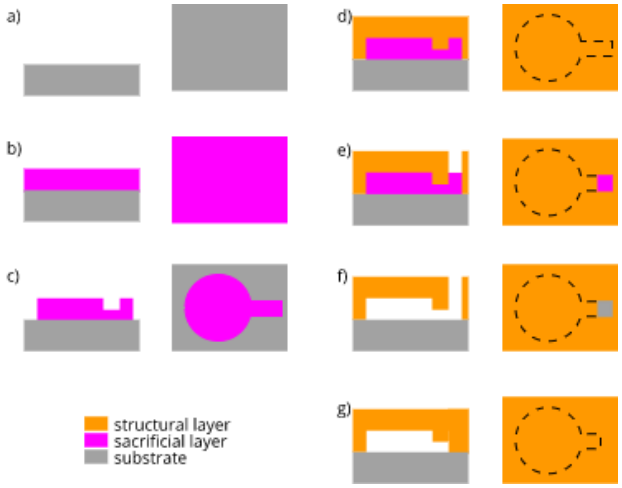

Figure 2.6: Cross section and top down views of a CMUT sacrificial layer process a) substrate; b) sacrificial layer deposition; c) patterning; and d) structural layer deposition; e) etch hole patterning; f) sacrificial layer release; g) etch hole seal

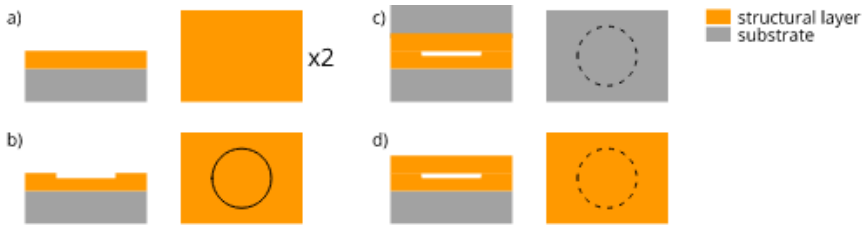

Figure 2.7: Cross section and top down views of a CMUT wafer bonding process a) two substrates with structural layers deposited; b) patterning of cavity in one of the wafers; c) both wafers are bonded; d) top substrate is etched to release membrane

Given both their dimensions and flexibility in fabrication methodology, CMUT arrays are well suited for incorporating into miniaturized probes such as catheter tips or implantable devices [71, 72]. It follows then, that CMUTs could be packaged into a microfluidic setting where acoustophoresis is popularly practiced. The element-wise control of CMUTs also allow for phased array operations which can be used to steer and focus ultrasound beams. This mode of transducer operation has been extensively used in imaging applications and we shall explore it next.

2.5 Resonators

In the seminal work of King, which provided the first quantitative analysis of particles in a sound field, it was shown that the gradient forces experienced by said particles was greater in a standing than travelling wave field [3]. We shall examine standing wave acoustic gradient forces in greater detail later, for now it is enough to note that many acoustophoretic devices pair transducers with acoustic resonators to create standing waves. There are two types of resonator systems employed in continuous flow acoustophoresis. The first was the layered resonator [6] and at its simplest is a fluidic chamber where one wall is coupled to a transducer and an opposing wall acts as a passive reflector (see Figure 2.8a). A more recent design is the transverse resonator [73] where a standing wave is created perpendicular to the direction of ultrasound activation (see Figure 2.8b). This is accomplished by creating reflections between the sidewalls of a channel. A final acoustophoretic platform worth mentioning is the standing surface acoustic wave (SSAW) (see Figure 2.8c). This technique, while still requiring a resonance condition, does not strictly speaking, rely on reflections within a resonator; rather, it generates surface standing waves via a piezoelectric substrate that acts both as a wave guide and the floor of a fluid chamber [74].

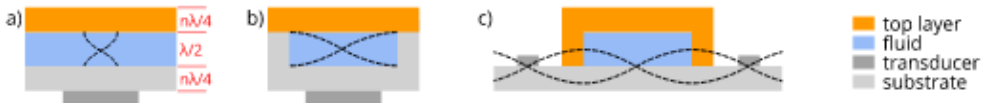

Figure 2.8: The various types of resonators a) layered; b) transversal; c) SSAW

Resonator design

The proper design of any acoustic resonator, irrespective of type, hinges on the concept of characteristic acoustic impedance, Z. Where the speed of sound in a medium (i.e. wave speed), c, is linearly related to the density, ρ, of that material such that

$$Z = \rho c \tag{2.30}$$

When sound travelling through one material meets the boundary of another material, the difference in the acoustic impedance of the two materials will determine how much sound is transmitted or reflected. This reflectance can be given by

$$R = \frac{Z_2 - Z_1}{Z_2 + Z_1} \tag{2.31}$$

Thus, to maximize the transfer of acoustic energy in a resonator system where a transducer is coupled to a fluidic chamber, the materials of each component must be considered. It would be ill-conceived, for example, to not expect losses when a piezoelectric transducer with a typical Z of 30 MRayl is joined to a chamber made of glass which has a Z of 12 MRayl. Clearly, introducing an intermediary material with a characteristic acoustic impedance between the two components would decrease the reflection of waves from transducer to chamber. This coupling material is called an impedance matching layer. Manneberg *et al.* coupled aluminum (17 MRayl) wedges to microfluidic chips as matching layers, demonstrating efficient, multi-frequency, two-dimensional particle manipulation [75]. This allowed for the offset mounting of smaller transducers, providing unobstructed views of the microchannel, ideal for microscopy applications. Larger impedance differences, such as piezotransducers directly in contact with water (1.5 MRayl) in a microchannel would result in even higher reflection-related losses.

When creating a resonator we care about its Q factor. In transversal resonators the standing wave is established by the bulk materials resonating as one, thus the resonator must be made of high Q materials such as metal, glass or silicon. In layered resonators, as the name implies, it is the thickness of the various layers that matters (see Figure 2.8a). In this case, a reflector layer with a thickness that is an odd multiple of $\lambda/4$ maximizes reflections due to the phase shift of the wave at the reflector-air interface. As long as the substrate and reflecting layer materials have thicknesses that are carefully matched with respect to their wavelengths [76], even low Q materials such as polymers may be used. Unlike the two previous layouts in which the waves move through the bulk of the material, the majority of the energy of a SSAW device is confined to within a single wavelength of the surface. Typically, opposing interdigitated transducers (IDTs) are formed on a piezoelectric wafer substrate between which a polymer channel is bonded. The polymer channel material is chosen to match the impedance of the fluid it contains, this ensures that no countering resonances are created and the standing wave is generated solely by the opposing transducers. Waves are formed on the substrate and guided into the cavity. With clever use of phase shifting IDT pairs it is possible to manipulate the standing wave such that it, and consequently the particles, can be positioned at any location across the cavity [32, 77]. However, in continuous flow environments, SSAW devices routinely operate at lower flow rates than their counterparts since more energy is dissipated into the surrounding material and thus the acoustic amplitudes maintained are lower.

Resonator fabrication

As one might expect, the techniques employed in creating an acoustic resonator depend almost entirely on the type of resonator chosen. For transversal resonators, silicon is a commonly used substrate. Given silicon's monocrystalline structure it can be wet etched to create cavities with highly vertical walls suitable for maintaining a standing wave. As previously mentioned, the adhesion between the top layer and the substrate must be robust in order to maximize resonance. Additionally, to maintain optical access to the cavity a clear top layer would be used. Thus glass is an excellent choice for the top layer given its transparency and the robustness of anodic bonding to silicon. A glass-silicon-glass sandwich construction was popularized by Manneberg *et al.* where glass forms both the top and bottom of a microchannel that is wet etched through a silicon wafer [78]. All-glass transversal resonators have also been explored, with cavities wet etched and then top layers fusion bonded. Despite the non-vertical walls that result from glass etching, good standing wave generation has provided results on par with silicon substrates [79]. Glass capillaries have also served as simple, off-the-shelf, solutions for microfluidic resonators [80, 81, 82]. While many capillary sizes are available, they are generally configured to have only a single inlet and outlet, limiting their potential acoustophoretic applications.

Layered resonators have stringent thickness requirements but more flexibility in material selection than transversal resonators. The simplest layered resonator places two transducers opposite one another and a cavity between them also acting as the spacer. Various materials have been used for the cavity ranging from quartz to polymers [6, 31]. Techniques such as soft lithography can be used with polymers in creating the cavity but a material like quartz would have to be specially machined. The more typical layered resonator design uses a single transducer to transmit ultrasound from one surface of a cavity, travels through the fluid layer and is then reflected at the opposite surface using a high impedance material such as metal or glass [83]. The thickness of this reflecting layer with respect to the fluid layer is crucial if we wish to control particle movements accurately and predictably [76]. For a $\lambda/2$ resonator, where the cavity height is equal to a half-wavelength of the frequency of sound in the cavity medium, a reflector with a thickness that is an odd multiple of $\lambda/4$ is used due to the 180° phase shift of the wave when reflecting off the less dense medium (i.e. air) on the opposite side of the reflector layer [84].

Unlike the previous resonators where off-the-shelf transducers are often incorporated into the device, a SSAW resonator requires a piezoelectric material to be the substrate, upon which interleaved metal strips can be deposited to form the IDTs. The width and pitch of the electrodes determines the frequency of operation. Since standing wave generation is decoupled from cavity material a SSAW user can exploit polymers as cavities. The

polymer is either etched or soft lithography can be utilized to create cavities before being carefully aligned with the piezoelectric substrate and then plasma bonded.

In the chapters to follow we shall explore a method to simplify resonator fabrication for piezo-equipped devices, determine how CMUT technology can be incorporated into resonators, and see if resonators really are required after all.

Chapter 3

Resonators Revisited

3.1 Cheaper, faster, better?

As we previously discussed in Chapter 2.5, three basic resonator designs have been popularized in acoustopheretic research. Unfortunately, the associated material choices and fabrication complexity of these resonators have driven costs upwards and out of the reach of labs in developing nations or consideration in novel products. The SSAW resonator for example, requires expensive piezoelectric substrates, deposition and lithographic manufacturing processes for IDT electrodes and the fluid containing polymer cavity. Although bypassing the need for patterned IDTs has been demonstrated the need for the piezoelectric substrate remains [85]. Layered resonators are hamstrung by the thickness requirements on each of the eponymous layers. Furthermore, the direction of acoustic manipulation in a layered resonator is often parallel to the optical path, confusing observation of the acoustophoretic event. One strategy to counteract the layered resonator's drawbacks has been to use a pair of opposing transducers [31]. However, similar to the SSAW resonator, this solution comes with the added cost and complexity of running multiple transducers. The transverse resonator has less stringent material thickness requirements than its layered counterpart. However, after a cavity material is etched, electrochemical bonding of the other surfaces is performed to ensure the entire assembly resonates as a single body. This demands tolerances on surface roughness and cleanliness that are typically only found on wafer substrates. Clearly, each of the masking, etching, polishing, and bonding steps involved in the fabrication of all three types of resonators requires time and expertise on different equipment. As mentioned in chapter 2.5 cylindrical and rectangular glass capillaries are a cheap and disposable resonator option. However, channel geometries more

complex than single inlet and single outlet, are unavailable. We wondered, is there a simple approach to resonators? One that uses easily accessible materials, can be fabricated *sans* cleanroom, allow for more than a single flow channel, and remain suitable for microscopy applications?[1]

3.2 Considerations and fabrication

Since we wanted to produce a device that was easily compatible with standard microscopy techniques, a transverse resonator design and optically transparent substrates were natural choices. Furthermore, while a simple, straight microchannel could be used to validate our design, realistically, we would have to incorporate flow splitting to broaden their practical use. For example, bifurcating channels could be useful in separating a single population of cells for downstream differential analysis [86]. Likewise, trifurcating channels could be used for debulking particles from solution [87]. It was also decided that operation in the low MHz region would allow activation of at least the first two resonance modes (see Equation 2.7) and still keep resonator widths in the micro regime ($\leq$750 μm).

Commercially available, $25 \times 75 \times 1$ mm microscope slides made from soda-lime glass met both the optical and acoustic requirements with the added benefit of low cost, $\approx$\$0.15 per slide. Rather than etch the microchannels in the glass, we used three layers of slides to form the top, bottom, and walls of microchannel (see Figure 3.1a). In fact, an entire microchannel can be formed from a single slide. Sections $25 \times 25 \times 1$ mm were scribed with a glass cutter and broken over a metal straight edge to form the top and bottom of the channels. For simple single channels, walls were cut into $25 \times 12.5 \times 1$ mm or, similarly, for bifurcating or trifurcating channels into $12.5 \times 12.5 \times 1$ mm sections. After cleaning with alcohol and drying with compressed air the glass layers were bonded using double-sided Kapton polyimide tape (Ted Pella Inc., 16087-25) with a total film thickness (including silicone adhesive layers) of 110 μm providing chemically-inert, watertight seals at a cost of $\approx$\$0.14 per device. The key to our device simplicity was in the spacing of the walls that formed the channels. By using combinations of #0, 1, and/or 2 cover slips removable shims were formed to use during wall placement. A single glass section forming one of the microchannel walls was attached after which the removable shim placed and opposing wall affixed. In this fashion, depending on microchannel type (straight, bifurcation, or trifurcation), channel widths of 750, 600, 300, and 200 μm were constructed. Table 3.1 shows that from six channels of all three types, we determined the repeatability and accuracy of

[1] Portions of this chapter have appeared in the publication: C. Samarasekera et al., "Facile microfluidic channels for acoustophoresis on a budget", Biomedical Microdevices, 17(5), 2015.

fabrication to be comparable to plasma etching on glass [88]. This method of construction had the added benefit of inlet and outlet holes that were automatically aligned to the microchannel, allowing for considerable location tolerance. Once the microchannel top layer was attached with Kapton tape, ports for both the inlet and outlet were fashioned from either 22 or 30 gauge needles and secured to the openings with hardware store epoxy. Three different PZT transducers operating at 1, 2.5, and 5 MHz (Steiner and Martins Inc., SMD20T21F1000R, SMD20T08F2500R, and SMD20T04F5000R) were used as ultrasound sources at a cost of ≈$7.50 per transducer. The transducers were acoustically coupled to the back of the glass assembly with a water-soluble, ultrasound gel, however, if easy salvaging of transducers was a non-issue, simple epoxy could also be used. The total cost of the microfluidic device was ≈$8. A comparison of fabrication steps and materials cost between a typical MEMS approach and our method is shown in Table 3.2. While larger production volumes would benefit from MEMS fabrication, the process we have outlined is ideally suited to the prototyping needs of research and development environments.

Table 3.1: Design width and actual width (with intra-channel standard deviations) of fabricated microchannels, all dimensions in μm

Design	200	300	600	750
Actual	200±10	301±8	588±12	750±8

3.3 Experiments

Testing of microchannels was performed with a 1.3 x 10^7 ml^{-1} solution of 10 μm diameter fluorescent polystyrene latex beads (Magsphere, PSF-010UM) in deionized water pumped through the microchannel at rates of 10 to 20μl min^{-1}. The transducers were driven via a function generator (BK Precision, 4084) routed through an amplifier (Tabor Electronics, 9400). The acoustophoretic ability of the microchannels was visually inspected under a fluorescence microscope (Nikon, E600FN). Initial experiments were performed on simple straight microchannels with widths of 350 and 750 μm, followed by experiments on bifurcation channels with 600 μm parent and daughter channels, and finally trifurcation channels with 600 μm parent and 200 μm daughter channels.

Table 3.2: A comparison of typical microchannel material costs and fabrication steps using standard MEMS techniques to our facile method

Typical MEMS method (glass-Si-glass)	**Cost(ea)**	**Our facile method (glass-Kapton-glass-Kapton-glass**	**Cost(ea)**
Microchannel materials (substrate & transducer)			
Glass wafer x2 (50.8 x 0.5 mm)	\$12.50[a]	Glass slide (25 x 75 x 1 mm)	\$0.15
Si wafer (50.8 x 0.3 mm)	\$16.90[a]	Double sided Kapton tape (25 x 50 mm)	\$0.14
Piezoceramic transducer (dia. 20mm)			\$7.50[b]
Microchannel materials (alignment)			
Mask (76.2 x 1.5 mm)	\$130[c]	Shim (coverslips)	\$1.19
Microchannel fabrication			
Wafer cleaning (RCA) Photoresist (spin & bake) Mask (align & expose) Photoresist (develop) Etch (wet or dry) Photoresist (remove) Wafer bonding (anodic) Dicing Ports		Slide cleaning (acetone & ethanol) Sizing (scribe & break) Kapton tape (adhere & trim) Side bonding (shim align) Ports	
[a]based on 10 unit pricing for double side polished wafers from University Wafer (www.universitywafer.com) [b]based on pricing for SMD20T21F1000R, SMD20T08F2500R, and SMD20T04F5000R from Steiner and Martins Inc. (www.steminc.com) [c]based on Cr deposited soda-lime glass, contact mask with 10 1 m feature size from Front Range Photomask LLC (www.frontrange-photomask.com)			

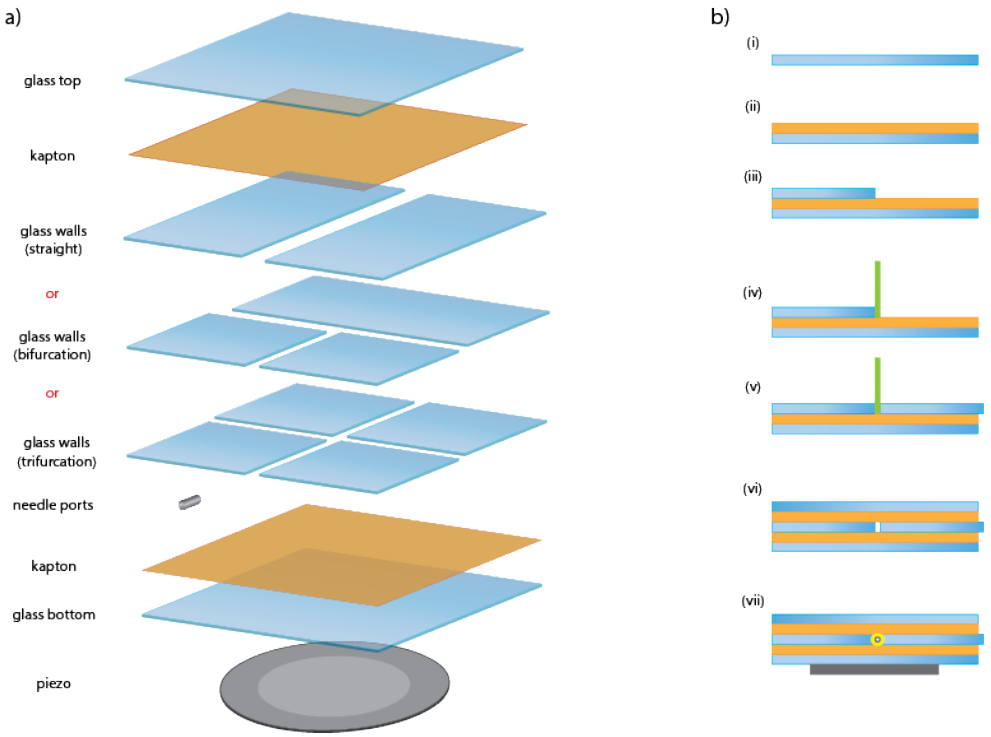

Figure 3.1: a) Exploded view of microfluidic resonator and its components; b) Sandwich fabrication steps for straight channel resonator (i) Glass surfaces cleaned with ethanol. (ii) Double sided Kapton tape applied to channel bottom glass surface. (iii) First channel wall affixed. (iv) Shim is applied. (v) Second channel wall affixed. (vi) Shim is removed and glass and Kapton forming channel top is affixed. (vii) Needle ports are epoxied and piezoceramic transducer is mounted

3.3.1 Straight channels

A 750 μm channel was paired with a 1 MHz transducer operating at 180 V_{pp} to create a standing wave with a node in the center of the channel. Similarly, a 300 μm wide channel was paired with a 5 MHz transducer operating at 20 V_{pp} to create a standing wave with two nodes situated approximately a third of the way from opposite walls. A top down view of the straight microchannel assembly and microscope imagery of the microchannel in action can be seen in Figure 3.2.

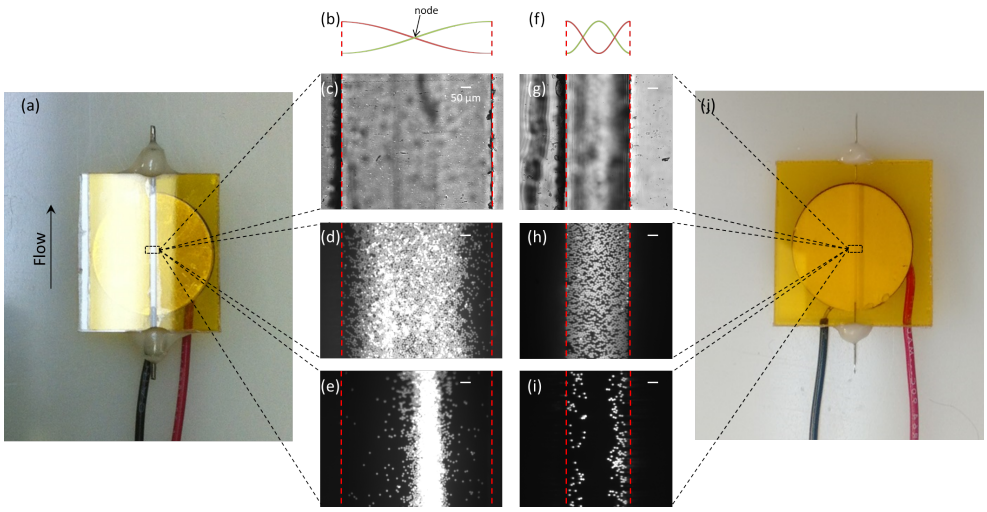

Figure 3.2: Top view of (a) 750 μm and (j) 350 μm wide microchannel. Sketch of the expected single node and dual-node waveforms generated by the (b) 1 MHz and (f) 5 MHz actuation in the cross-section of their respective microchannels. Microscope images of the same region of the device when (c,g) channels are empty, (d,h) bead solution is flowing but ultrasound is off, and (e,i) bead solution is flowing and ultrasound is activated. Red dashed lines indicate the location of the microchannel walls.

3.3.2 Bifurcation and trifurcation channels

The same concentration of bead solution was used to test bifurcation and trifurcation microchannels. A 50 V_{pp} signal was applied to a 2.5 MHz transducer attached a 600 μm resulting in a two node standing wave. With the ultrasound activated and a flow rate of 10 μL min-1 the particles in the bifurcation channel aligned to the nodes but began to swirl and collect at the t-junction walls due to disruption of the laminar flow. The vortices likely indicate the formation of a recirculation zone where the dominant flow direction of the flow field encounters an opposite velocity component. Parametric studies of laminar flow at t-junctions have shown that the size, strength and location of recirculation zones are directly influenced by the width of the daughter channels and the Reynolds number [89]. We observed that increasing the flow rate in the bifurcation channel to 20 μL min-1 provided a smoother transition of beads from the parent to the daughter channels. The increase in flow rate caused an increase in Reynolds number, which has been shown to stretch the recirculation zone downstream [89]. We posit that at the higher Reynolds number, the length of the daughter channel may have been shorter than required for the

recirculation zone to form. Although beads aligned to the nodes in the trifurcation channel, unlike the bifurcation channels, disruptions to the laminar flow in the trifurcation devices did not alleviate with increased flow rate. This resulted in some collecting of beads along the lower edge of the walls of the daughter channel. Due to the more complicated flow in the trifurcation channels the previous findings may not be valid in this instance. A more accurate model of the trifurcating junction may help in eliminating the recirculation zone in future designs, however, this work should be considered as a first step in a process development approach. Acoustic streaming was not observed, which is not unexpected given the larger particle sizes and the channel widths. The meandering behaviour of beads in the trifurcation channel indicates changes to the nodal locations along the length of the microchannel. This is a well-known occurrence in acoustophoretic microchannels and is believed to be caused by structural deviations, temperature changes, and other loss mechanisms in the channel disrupting the frequency at which resonance occurs [90]. One method developed to counteract this effect is to sweep the excitation frequency over a 100 kHz range at kHz rates [91].

3.4 Discussion

In this chapter the construction of prototype microfluidic transversal acoustic resonators from glass microscope slides and polyimide tape was outlined and demonstrated. After implementing simple straight channel geometries the construction process was then easily modified for more versatile bifurcation and trifurcation channels. The orthogonal T-type and cross-type junctions did cause disruptions to the laminar flow in the form of recirculation zones but, in the case of the bifurcation channel, this was addressed by increasing the flow rate. It should be possible to reduce disruptions to the flow by constructing shallower angle bi and trifurcations. Another option is to incorporate hydrodynamic focusing by using the construction technique described here to build multiple input microchannels that can take advantage of sheath flows. Although coverslips were used in this instance, depending on user application, anything from canulae to precision machined materials might be substituted as shims. Besides performing as a seal, the Kapton tape provides flexibility in choice of resonator layer materials. For example, metal channels could similarly be produced using this sandwich construction method, bypassing the need for screws and clamps. Furthermore, combinations of dissimilar, difficult to bond layers such as bulk metal to glass could also be realized. For inverted microscopy applications, where the transducer would block the optical path, it could be possible to use coupling wedges to offset the transducer and keep the entire microchannel transparent [75].

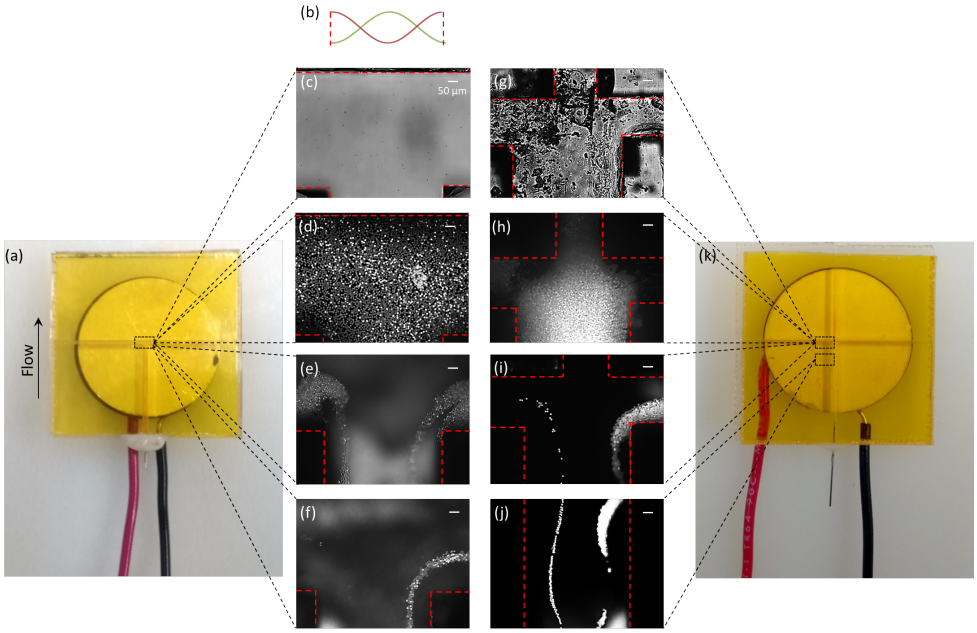

Figure 3.3: Top view of (a) bifurcation and (k) trifurcation microchannel. Sketch of (b) the standing wave generated by the 2.5 MHz actuation in the cross-section of both bi and trifurcation devices. Microscope images of the bifurcation/trifurcation junctions when (c,g) channels are empty, (d,h) bead solution is flowing but ultrasound is off, and (e,i) bead solution is flowing at 10 μL min-1 and ultrasound is activated. Increasing the flow rate to (f) 20 μL min-1 saw a smoother transition of beads from the parent to daughter channels in the bifurcation device. Beads were unevenly distributed (j) along the two nodes in the parent channel of the trifurcation device and did not improve with increasing flow rate. Red dashed lines indicate the location of microchannel walls.

The method we have employed requires no specialized microfabrication techniques or bonding processes, and can be done on any benchtop around the world. Transversal resonator layers have historically been electrochemically bonded due to concerns over the entire assembly resonating as a single body. We believe that potential users need not be restricted to such bonding processes. The method herein should be broadly applicable with other high impedance materials typically used in acoustophoresis. It is our hope that this fast, straightforward, and cheap fabrication method will help to further disseminate the use of acoustophoretic platforms.

It must be noted that although we have addressed some of the cost and fabrication disadvantages of the transverse resonator here, there remain drawbacks to the typical

piezo-equipped, (both transverse and layered) resonator that must be considered. For one, when a channel geometry is fixed, changing the location of a node is difficult. The mode of the standing wave can be changed by using other transducers operating (not concurrently) at frequencies that are multiples of the first. Furthermore, a phase shift technique can be attempted with paired transducers; this has been demonstrated with both SSAW and layered resonators [77, 92]. Yet, if the goal of acoustopheretic platforms is incorporation into larger, Lab-on-a-Chip systems, any device shackled to the piezoelectric effect is ill-suited to CMOS fabrication and will face questions regarding commercial viability.

Chapter 4

A CMUT Alternative

4.1 Co-opting CMUTs into acoustophoresis

A fundamental limitation to acoustophoretic techniques being fully realized on Lab-on-a-Chip devices is the CMOS fabrication incompatibility of piezoelectric materials. Alternatively, CMUT fabrication employs techniques similar to those already found in the integrated circuit and microfabrication industries [61, 93]. This makes CMUTs an ideal platform for incorporating with other electronics in a Lab-on-a-Chip. Furthermore, in most piezotransducer applications transferring acoustic energy into fluid mediums requires extra coupling layers to overcome the impedance mismatch; however, CMUTs can transfer their energy into fluids without the need for impedance matching. The wider bandwidth of CMUTs could also prove useful, allowing for a greater range of frequencies with a single device that might otherwise have required more than one piezotransducer. Beamforming with piezotransducers in an acoustophoretic setting has been explored previously, most notably with curved transducers or acoustic lenses such as in acoustic levitation and trapping [94, 49, 95]. Beamforming through phased array operation of piezotransducers have also been reported in acoustophoretic applications like tractor beams and 3d manipulators [96, 97]. However, these arrays incorporated large transducers operating in the kHz region, and manipulating macroparticles. More compatible with microfluidic applications, microparticles have been trapped and positioned via phase changes to rectangular and circular arrays of piezotransducers or by switching active subsets of arrays [92, 98, 82].

The first instances of CMUTs being used in microfluidic settings were for fluid actuation and in sensing some physical fluid properties [99, 100]. Although in these cases, Scholte waves were being used, which propagate along the interface of the membrane and the fluid

rather than standard pressure waves which travel into the fluid bulk. Recently, CMUT induced, Scholte waves have also been used to control rates of biochemical adsorption and interaction [101]. In this chapter we will explore the possibility of driving pressure waves with CMUTs, and how CMUTs may be incorporated into resonators. The experiments used to test these ideas will be described and their subsequent results will then be reported.[1]

4.2 Design considerations

The implications about the type of resonator that can be created when using CMUTs, hinge around their acoustic impedance. While clearly well matched for fluids, CMUTs do not couple well to solids. Thus transverse resonators, where the entire system must resonate as a single body, are out of the question. When Thränhardt *et al.* used CMUTs to create standing Scholte waves they created something analogous to a SSAW resonator. However, the very low penetration depths of interface waves may have questionable utility in acoustophoretic settings. This leaves the layered resonator design. Depending on the acoustic power required a layered resonator with either a dual, opposing-transducer, (see Figure 4.1a) or simple reflector design (see Figure 4.1b) could be constructed. The former would be a considerable challenge to implement. First, consider that each CMUT device and their respective cells would have to be carefully aligned to each other. This non-trivial task would be further complicated by virtue of the fact that most CMUT substrates are not transparent. CMUT fabrication using glass substrates have been reported, however, the poor conductivity of glass requires opaque metals be deposited to form the bottom electrodes of a CMUT [102]. Second, given that the devices would be separated by a few hundred microns, fittings for inlet and outlet ports would likely have to be incorporated through the CMUT devices themselves. By contrast the simple reflector is easier to fabricate both in terms of materials and complexity. Resonator depths would depend on CMUT frequency of operation. As discussed in the previous chapter, low MHz transducers would constrain resonator depths in the order of hundreds of microns. This matches well with the typical thickness of adhesive Kapton tape, onto which, a laser cutter can easily transfer patterns. Thus quick fabrication of variously sized layered resonators is possible. A transparent, high impedance material, such as glass, would make an ideal reflecting layer that also allows for top down observation of experiments.

This was exactly the route presented by Zeshan *et al.* in a simulation of a CMUT array integrated with a simple reflector to create a resonator [103]. The computational study

[1] Portions of this chapter have been submitted for publication in Sensors and Actuators B.

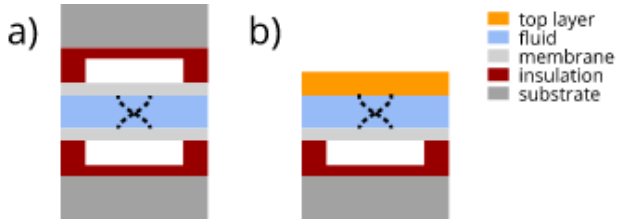

Figure 4.1: Two examples of potential CMUT layered resonators with a) paired CMUT; or b) reflector designs

concluded that a standing wave pressure node could be sustained but such a device was neither fully fabricated nor experimentally verified.

Let us also consider the option of not using a resonator design at all. In Chapter 2.3.5 we briefly described the dual and single beam trap. Might the beamforming capability of a CMUT array be utilized in these types of focused beam applications? Earlier in this section, when contemplating the layered resonator, we mentioned the increased difficulty in the opposing CMUTs design; thus for now let us disregard the dual beam trap. One consequence of operating in the ray acoustics regime are the high frequencies at which a CMUT array would have to operate to influence microparticles; typically 10× higher than the typical frequencies used in resonator-based platforms. Additionally, single beam traps have very tight axial and lateral focus requirements [49]. This in turn would demand close tolerances on the fabricated microarray and its phase-delay operation. A far simpler solution may lie in the symmetry of the CMUT cell itself. In a paper presented by Mao *et al.* a simulation of a single hexagonal CMUT cell was shown to create a potential well with the minima centered in the middle of the cell and close to the CMUT membrane [104]. From simulations, the gradient force was expected to be in the hundreds of pN. Based on these results a concentric array of hexagonal cells was fabricated and characterized. When the first ring of hexagonal cells was activated during immersion operation the center cell operated as expected but significant suppression of the surrounding CMUT cells was reported. The authors leveraged this unforeseen behaviour to observe the capability of a single hexagonal CMUT cell. During experiments a single 10 μm polymer particle was photographed near the surrounding ring before CMUT activation and then over the central cell after activation. This method of acoustophoresis could be very useful if a device could be optimized for array operation, demonstrated with higher bead populations, and shown to work under flow conditions. A microchannel is necessary to enable flow, however, the formation of standing waves would have to be suppressed. Assuming the same orientation of components as seen in Figure 4.1b, we can simply do the opposite of what was recommended in Chapter 2.5. First make the distance between membrane and top layer shorter than $\lambda/2$,

the likely shortest distance at which a standing wave will form. Although the top layer must still be transparent for observation, rather than glass, we can choose a material that is a poor acoustic reflector, with a thickness that is not an odd multiple of $\lambda/4$. The reflection at the fluid-wall interface will depend on the acoustic impedance mismatch between the two materials. Thus, choosing a wall material that is of similar acoustic impedance to the fluid, such as PDMS, will be useful in minimizing reflections. This was demonstrated to great effect by Leibacher *et al* when they used impedance matched layers to create resonators with decoupled acoustic and fluidic boundaries [105].

Ideally, harnessing the capabilities of an N×N CMUT array would mean independent control of each CMUT element. However, the number of electrical connections required quickly turns this into a complicated proposition. One solution to this, first suggested for imaging applications, is the row-column (RC) addressing scheme that reduces the number of required connections to N+N from N×N [106]. In such a scheme, the top electrodes of an RC-CMUT array might be connected in rows, and bottom electrodes wired in columns. Thus operating an element requires activating its corresponding row and column electrode. This simplification comes at the expense of flexibility, however, as it rules out the operation of some element combinations (see Figure 4.2).

Figure 4.2: The operation of a a) row-column addressed 2×2 array; illustrating the element activation combinations (in green) that are b) allowed; and c) forbidden

4.2.1 Phased array

An interesting application of focused ultrasound used a curved piezoelectric transducer to trap microparticles in a quasi-standing wave formed between the transducer and a reflector [51]. A planar CMUT device in phased array operation could emulate the focused beam of a curved transducer. The advantages in using a CMUT microarray is that the beam could also be electronically steered or, given a sufficiently large array, translated. Thus moving the trapped objects may not require physically manipulating the transducer.

4.3 Simulations

4.3.1 CMUT cell

In order to understand the behaviour of the CMUT a finite element model (FEM) was created in COMSOL Multiphysics software. A simplified 3D model, was used to represent a circular CMUT cell (see Figure 4.3a) with radii, r, and thicknesses, t, of each component. The model couples an *electromechanics* subdomain to the cavity and solid materials, and a *pressure acoustics* subdomain to the fluid and perfectly matched absorbing radiation layer. The matching layer removes reflected sound waves from the fluid layer. The membrane layer is fixed at the edges to prevent translational motion but allow for deflection. The dimensions, mechanical (density, ρ, speed of sound, c, Young's modulus, E, and Poisson's ratio, ν), and electrical (relative permittivity, ϵ_r) properties of the materials used can be seen in Table 4.1. As a first step a static model was studied showing a collapse voltage of 105 V. At a bias voltage set to 60% of V_c the model reported a static deflection of 61 nm. The following step was to use the previous deflection information in a harmonic study to determine the frequency response of the membrane when a V_{bias} of 60 V was already applied. This suggested a CMUT resonance frequency of 3.09 MHz and a membrane deflection of 27 nm (see Figure 4.3b).

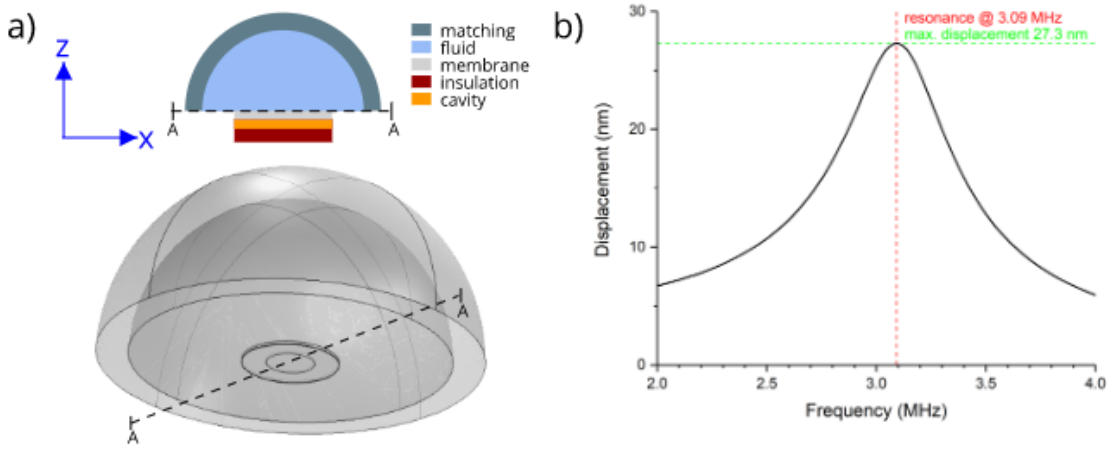

Figure 4.3: a) Simplified 3D COMSOL model with dimensions and materials provided in Table 4.1; and resulting b) frequency response of the membrane

Table 4.1: Dimensions and properties of materials used in travelling wave COMSOL model

Part	**Dimensions**		**Material**	**Properties**				
	r (μm)	t (μm)		ρ (kg·m^{-3})	c (m·s^{-1})	E (GPa)	ν	ϵ_r
Membrane	30	1.7	Si	2320	8490	169	0.22	4.5
Insulation	30	0.5	SiO2	2650	5900	73	0.17	3.9
Cavity	30	0.24	vacuum					1
Fluid	49.5		water	1000	1500			
Matching	60							

The pressure and velocity amplitudes of the acoustic wave in the fluid was also determined as a function of depth along the center of the CMUT cell using the frequency domain solver (see Figure 4.4a). By incorporating this data with equations 2.3 to 2.6 the numerical solutions to the acoustic potential and gradient force of the travelling wave can be found. In the example shown in Figure 4.4b a particle with a diameter of 4 μm, made out of silica ($\rho = 1800$ kg·m^{-3}, $c = 5900$ m·s^{-1}) is placed in the fluid. As might be expected of a single cell, the pressure drops significantly within the first 100 μm. The vertically acting gradient force is strongest at the CMUT membrane and suffers a hundredfold reduction 70 μm above the CMUT membrane. The negative values for F_{grad} indicate that the force is always acting toward the CMUT cell.

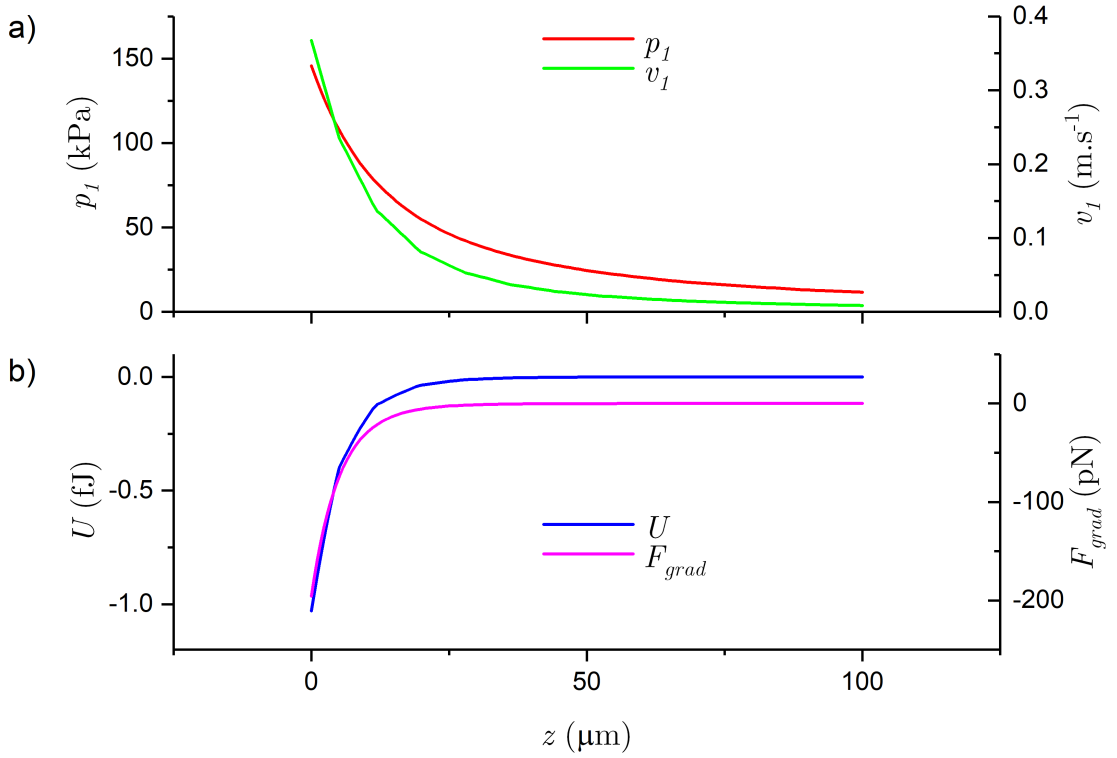

Figure 4.4: COMSOL simulation of a travelling wave's a) pressure and velocity amplitudes in the fluid for a single CMUT cell as a function of depth at x = y = 0; and numerical solutions to b) acoustic potential and gradient force on a 4 μm diameter silica bead

When we look at F_{grad} radially, starting from the center and travelling out past the edge of the cell an interesting story emerges (see Figure 4.5). The CMUT cell can compel silica microparticles almost 20 μm from the cell edge toward the central point of the cell. The lateral gradient force has an inflection point 15 μm from the center of the cell. At this location a particle will experience a peak force in the lateral direction of 63 pN. The implications of this are regions at the center of a circular CMUT cell, and very close to the surface, should act as a particle trap, comparable to a hexagonal CMUT cell [104]. Furthermore, the lateral force of a circular cell may be strong enough to trap particles against a flow.

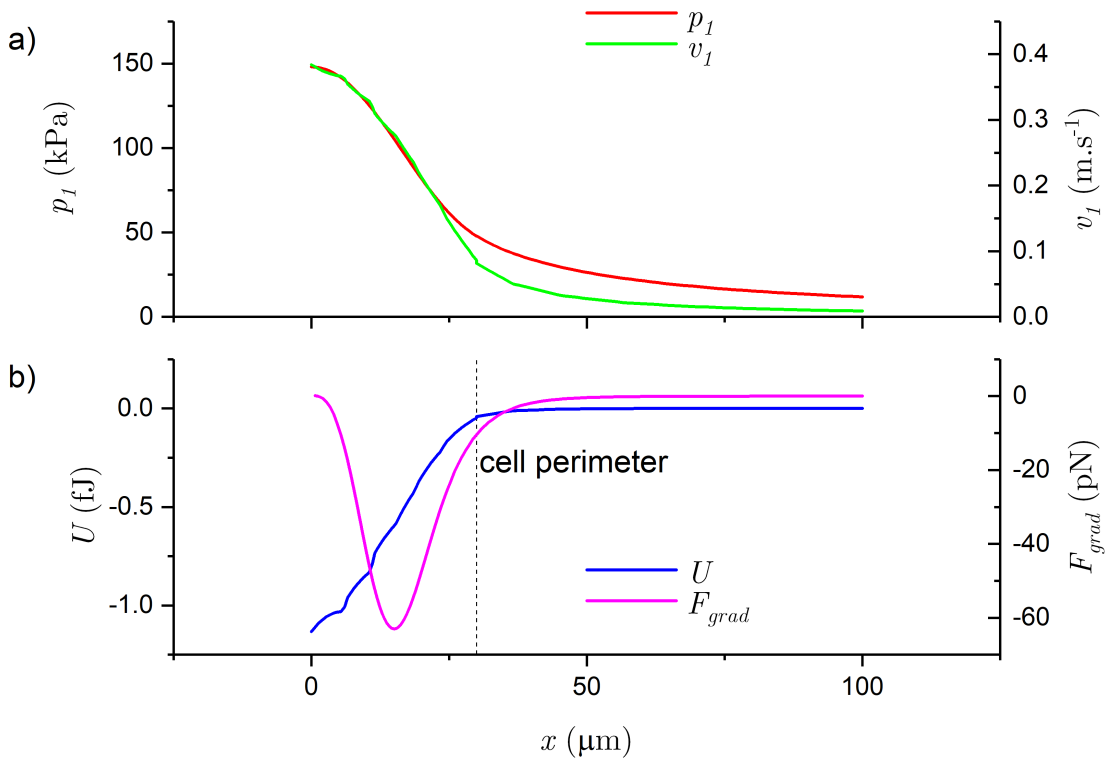

Figure 4.5: COMSOL simulation of a wave propagating in free-field a) pressure and velocity amplitudes in the fluid for a single CMUT cell as a function of radial distance at z = 0; and numerical solutions to b) acoustic potential and gradient force on a 4 μm diameter silica bead, the dashed line indicates the edge of a CMUT cell

Passive reflector

Next, a COMSOL model of a standing wave acoustic trap was established by creating a glass reflector layer of $\lambda/4$ thickness at a distance $\lambda/2$ above the membrane. In this model the hemispherical fluid and absorbing layers were replaced with a fluid cylinder, extruded to $\lambda/2$ with the same radius as the membrane (see Figure 4.6a). The top of the cylinder had the reflector layer followed by an air layer. A larger cylinder (1.3x the radius of the membrane) ensconcing the fluid formed the perfectly matched absorbing layer. Dimensions and layer properties are shown in Table 4.2 of any changed or new materials, those not listed are the same as in Table 4.1. Interestingly, as Figure 4.6b shows, the frequency response

of the membrane shifted slightly, with a sharper response at 2.98 MHz and slightly higher amplitude, followed by a series of decaying peaky responses. These changes may be directly due to interactions between the reflected wave and the CMUT membrane and have been reported in simulations where the distance to a reflector approaches a certain critical value, around $\lambda/2$ [107].

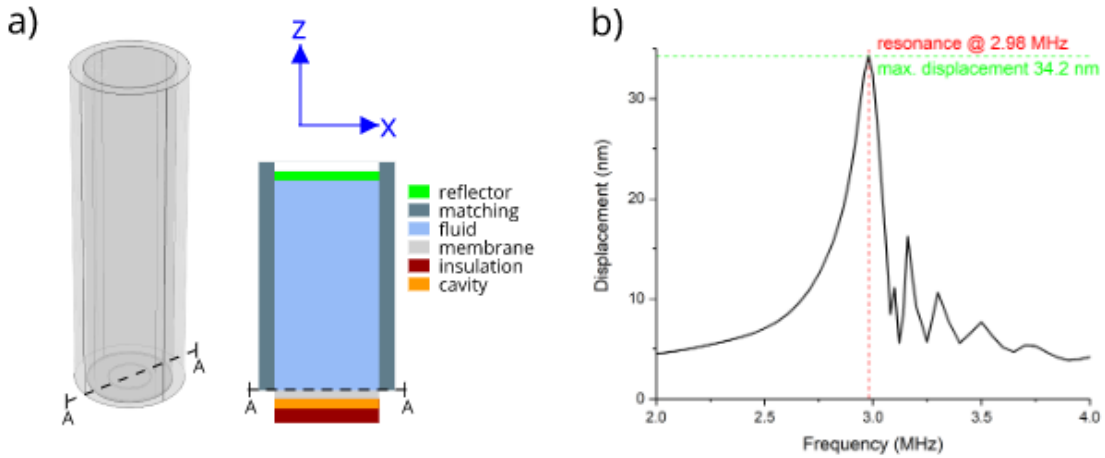

Figure 4.6: a) Simplified 3D COMSOL model of the reflector setup; and resulting b) frequency response of the membrane

Table 4.2: Dimensions and properties of materials used in standing wave COMSOL model

Part	**Dimensions**		**Material**	**Properties**	
	r (μm)	t (μm)		ρ (kg·m^{-3})	c (m·s^{-1})
Reflector	39	500	glass	2230	5647
Fluid	30	250	water	1000	1500
Matching	30-39	250			

As before, the pressure and velocity amplitudes as a function of depth along the centerline of the CMUT cell (see Figure 4.7a) was used to find the acoustic potential and gradient force acting on a silica sphere (see Figure 4.7b) using equations 2.8 to 2.12. Note the increasing pressure at the membrane and reflector with minimum near the center of the channel, indicating the location of a pressure node. The potential well is now near the pressure amplitude minimum unlike in the travelling wave case where the potential well was at the pressure maximum. The corresponding vertical gradient force is just over 2× smaller than the travelling wave case and, given the positive acoustic contrast factor

calculated from equation 2.12, we can expect that the particle will be levitated toward the channel center.

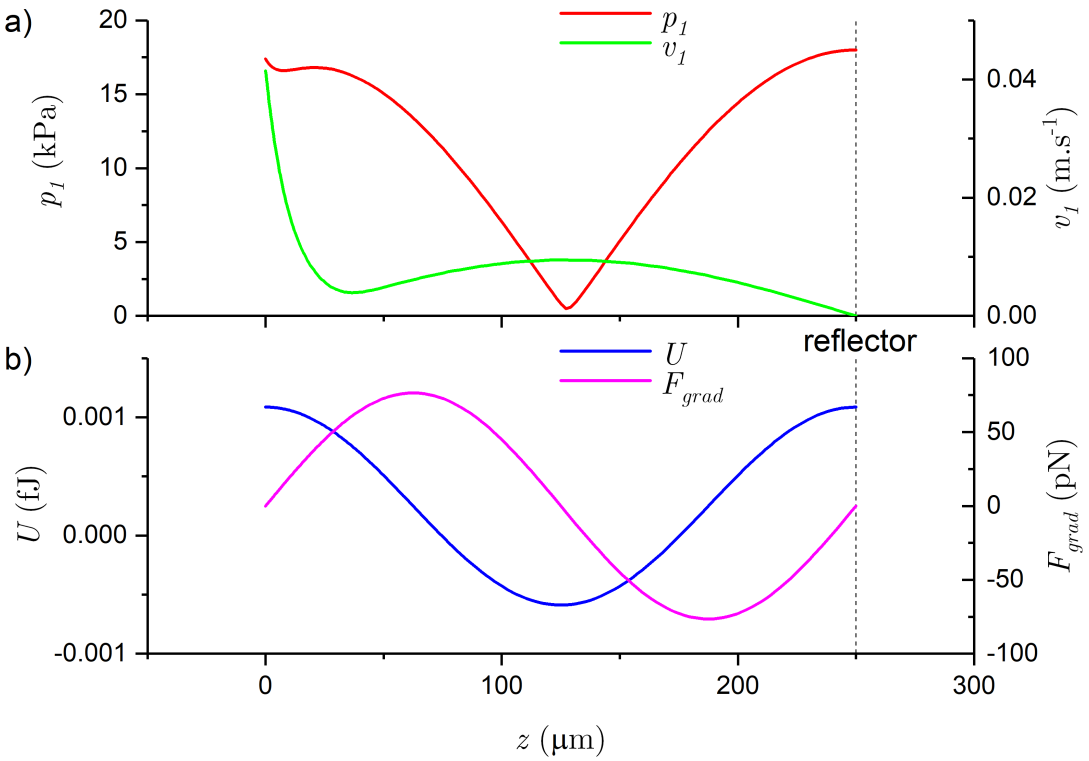

Figure 4.7: COMSOL simulation of a 3 MHz standing wave's a) pressure and velocity amplitudes in the fluid for a single CMUT cell as a function of depth at x = y = 0; and numerical solutions to b) acoustic potential and gradient force on a 4 μm diameter silica bead, with dashed lines showing the location of the glass reflecting layer

The pressure and velocity amplitudes along the radial direction at the center of the channel are shown in Figure 4.8a, from which we can then calculate the lateral force of the standing wave (see Figure 4.8b). This data indicates that the lateral trapping force of a single cell operating in the standing wave is much weaker than in the travelling wave case. There are two workarounds to this. First, the use of multiple CMUT cells and elements will have an additive effect on F_{grad}. Second, given that F_{grad} goes as the cubed radius of the particle we can simply use larger beads.

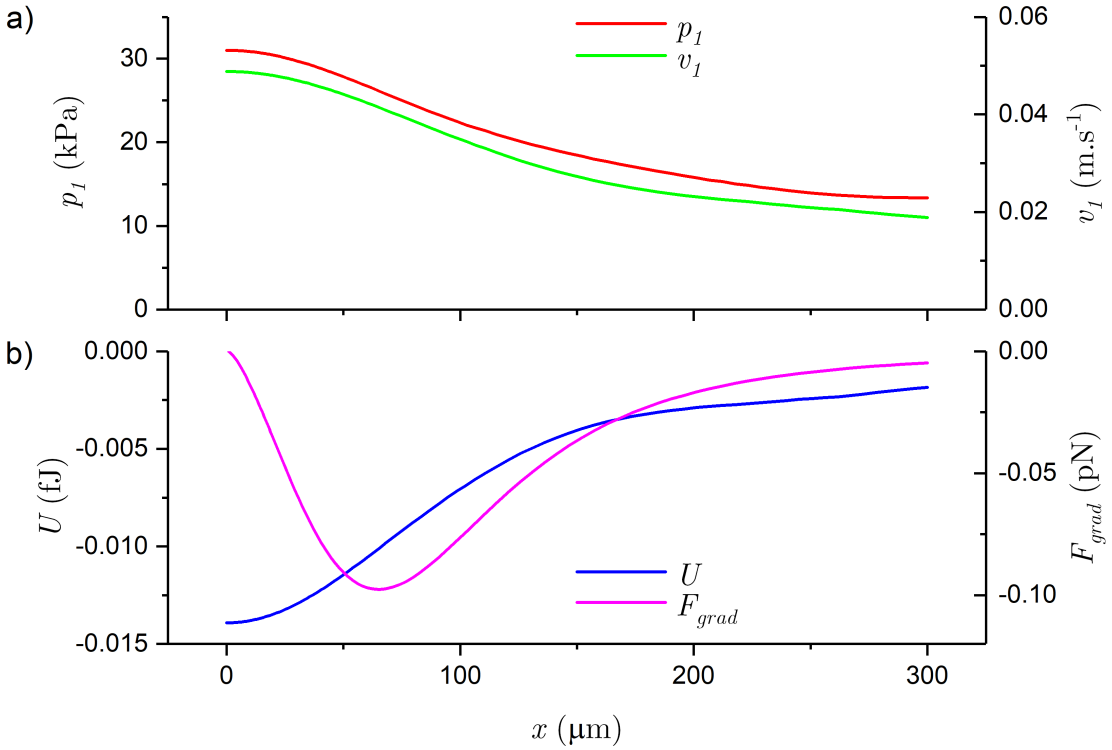

Figure 4.8: COMSOL simulation of a 3 MHz standing wave's a) pressure and velocity amplitudes in the fluid for a single CMUT cell as a function of radial distance at the expected pressure node in the vertical direction or z = 110 μm; and numerical solutions to b) acoustic potential and gradient force on a 4 μm diameter silica bead

The sensitivity of the standing wave to changes in CMUT operating frequency and channel height are also important considerations. The former because of the CMUT's bandwidth of operation and the latter due to tolerances during fabrication. Thus, we looked at the performance of a CMUT cell at 2.9, and 3.1 MHz in their respective 259, and 242 μm $\lambda/2$ resonators and compared it to the results of the 250 μm channel operating at 3 MHz (see Figure 4.9).

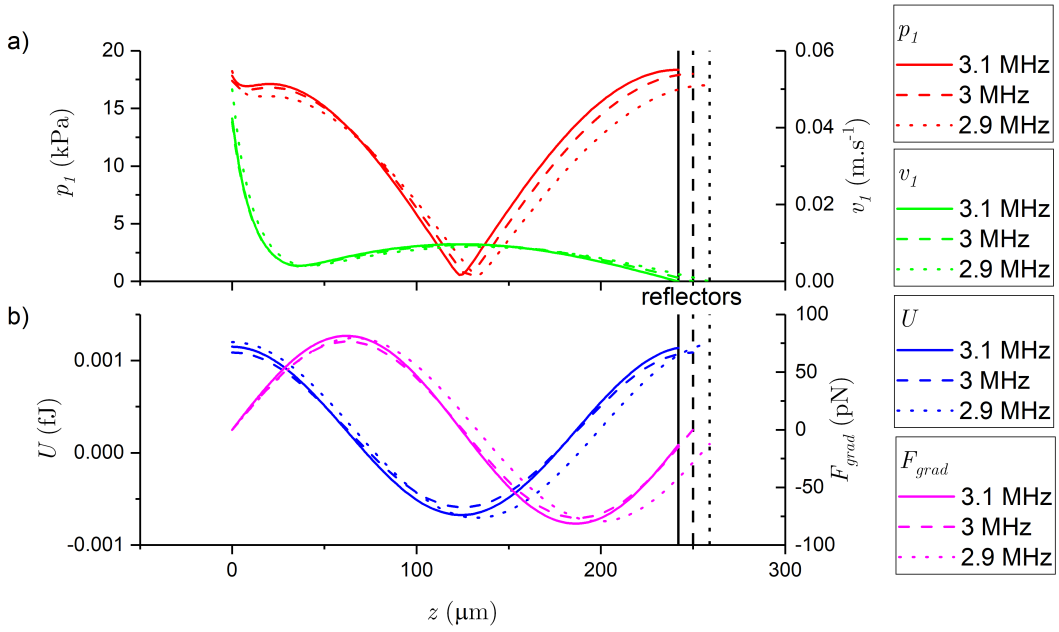

Figure 4.9: Comparison of COMSOL simulations of 3.1 (solid), 3 (dashed), and 2.9 (dotted) MHz standing waves' a) pressure and velocity amplitudes in the fluid for a single CMUT cell as a function of depth at x = y = 0; and numerical solutions to b) acoustic potential and gradient force on a 4 μm diameter silica bead, with vertical lines showing the location of the corresponding glass reflecting layer at each working frequency

Unsurprisingly, the location of the pressure node increases with decreasing frequency and its paired, increasing, channel width. The pressure at the reflecting wall increased by almost 8% as the frequency increased from 2.9 to 3.1 MHz. While the locations of maximum acoustic potential and gradient force shifted in a manner akin to the pressure node, their amplitudes changed by 20% and 2% respectively.

We then looked at how p_1, generated by a cell operating at 3.0 MHz, would change when paired with a reflector placed at varying positions along z. The results are presented in Figure 4.10.

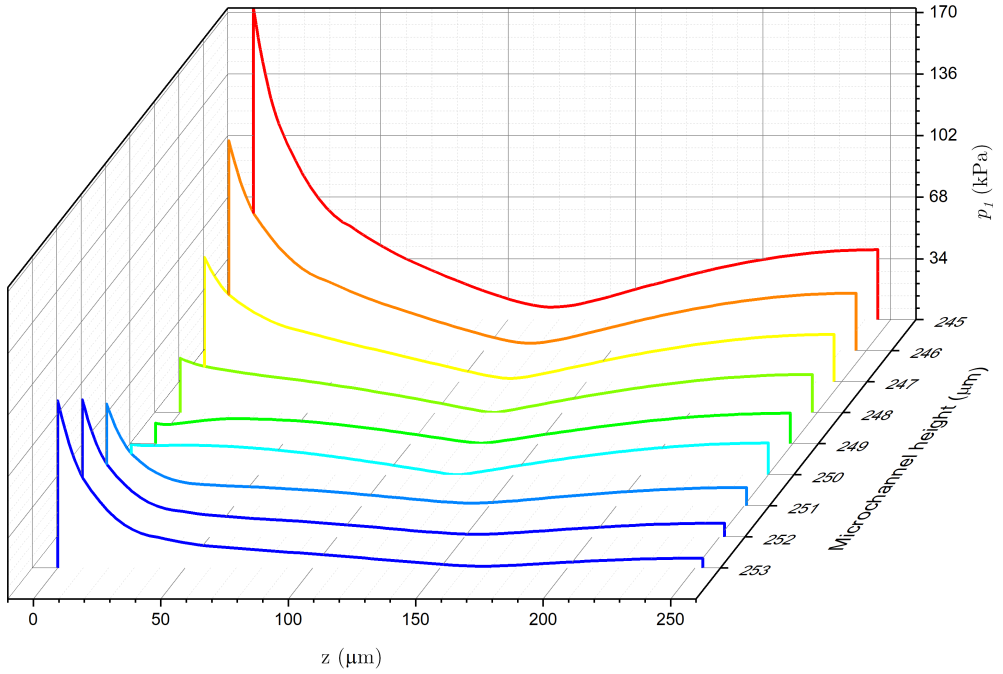

Figure 4.10: COMSOL simulation of a 3 MHz standing wave pressure amplitudes in the fluid for a single CMUT cell as a function of depth at x = y = 0, for microchannels of varying height

The model predicts that the shape of the standing wave devolves as the microchannel depth changes from the original $\lambda/2$ position of 250 μm. The superposition of transmitted and reflected waves in the microchannel become asymmetric with higher pressure amplitudes at the transducer surface than the reflector. The result is a parabolic behaviour to the pressure amplitude at the CMUT surface, with the lowest simulated pressure near the expected $\lambda/2$ microchannel dimension (see Figure 4.11a). Conversely, the pressure amplitude at the reflector surface drops exponentially with increasing microchannel length (see Figure 4.11b). The 1D pressure resonance in a $\lambda/2$ resonator is typically approximated by a cosine wave [30]. Therefore, the generalized equations for F_{grad}, and U introduced in section 2.3.2 may no longer be appropriate for these pseudo-standing waves.

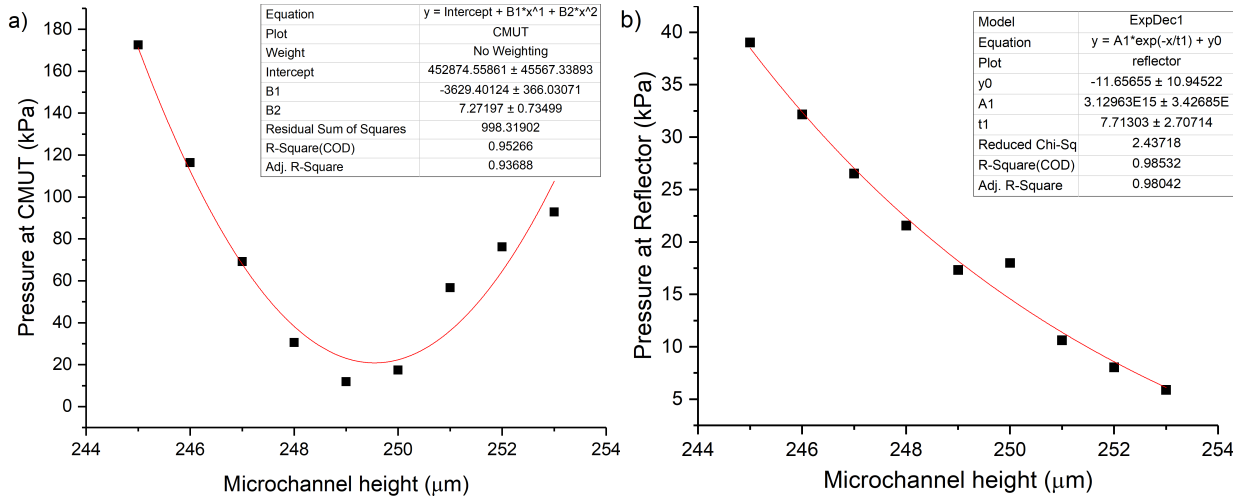

Figure 4.11: Behaviour of pressure amplitudes as a function of microchannel height at a) the CMUT surface; and b) the reflector surface

Opposing CMUT reflectors

Despite the considerable fabrication issues that would have to be overcome in order to build it, we also wanted to examine the performance of paired, opposing CMUT reflectors. A model similar to that of the passive reflector in Figure 4.6a where the reflector layer was replaced with another CMUT operating in unison to the first. As evidenced by Figure 4.12, the pressure amplitude, resulting acoustic potential, and gradient force were increased by 14%, 26%, and 40% respectively when compared to the single transducer and reflector setup of the same dimensions and operating frequency. It should be noted, that although the profile of the velocity amplitude of the two cases are quite different, the magnitude of their velocity amplitudes at the middle of the channel (i.e. the location of the pressure node) is within 9%. Thus, a well-designed single transducer system operates within the same order of magnitude as a two transducer setup.

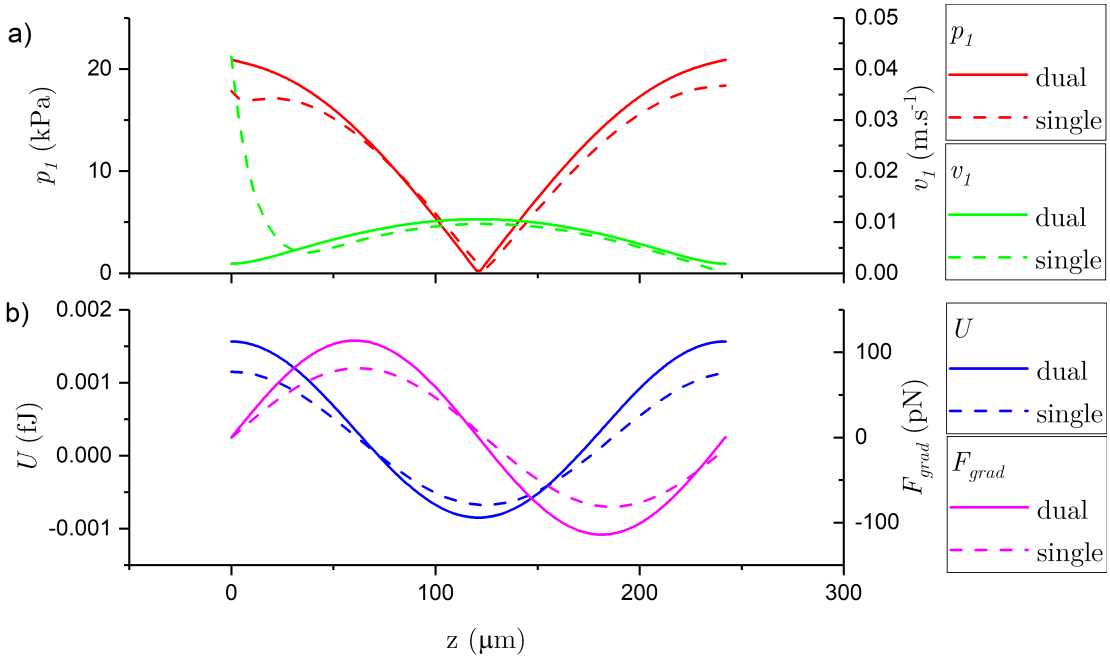

Figure 4.12: Comparison of COMSOL simulations of a 3.1 MHz standing wave's a) pressure and velocity amplitudes in the fluid for a pair of opposing CMUT cells (solid) and a single CMUT reflector (dashed) as a function of depth at x = y = 0; and numerical solutions to b) acoustic potential and gradient force on a 4 μm diameter silica bead

Poor reflector

The travelling wave model showed that the lateral gradient force could be as high as 60 pN near the surface of the CMUT cell. This could be useful in cases where particles could be trapped against a flowing medium. In order to contain the fluid, a channel must be incorporated onto the device much like the standing wave case. However, to maintain bead traps at or near the surface of the CMUT cell, the microchannel must undermine the formation of strong standing waves. To do this, the surface opposite the CMUT cell should be a poorly reflecting material with an acoustic impedance similar to the medium. We can further reduce the chance of standing wave formation by choosing a channel depth that is not a value λ/n, where n is any integer.

A model using a polydimethylsiloxane (PDMS) reflector at a distance $< \lambda/2$ was simulated in COMSOL (see Table 4.3). The thickness of the PDMS was chosen so as to provide enough support for inserted inlet and outlet ports and still not be an odd multiple of $\lambda/4$.

Table 4.3: Dimensions and properties of materials used in the poor reflector COMSOL model

Part	**Dimensions**		**Material**	**Properties**	
	r (μm)	t (μm)		ρ (kg·m^{-3})	c (m·s^{-1})
Reflector	39	2000	PDMS	965	1076
Fluid	30	200	water	1000	1500
Matching	30-39	200			

The resulting pressure amplitude (see Figure 4.13) decays exponentially in the fluid; the similar acoustic properties of the PDMS layer suppress reflections. As a result, there is no pressure node formation within the fluid channel.

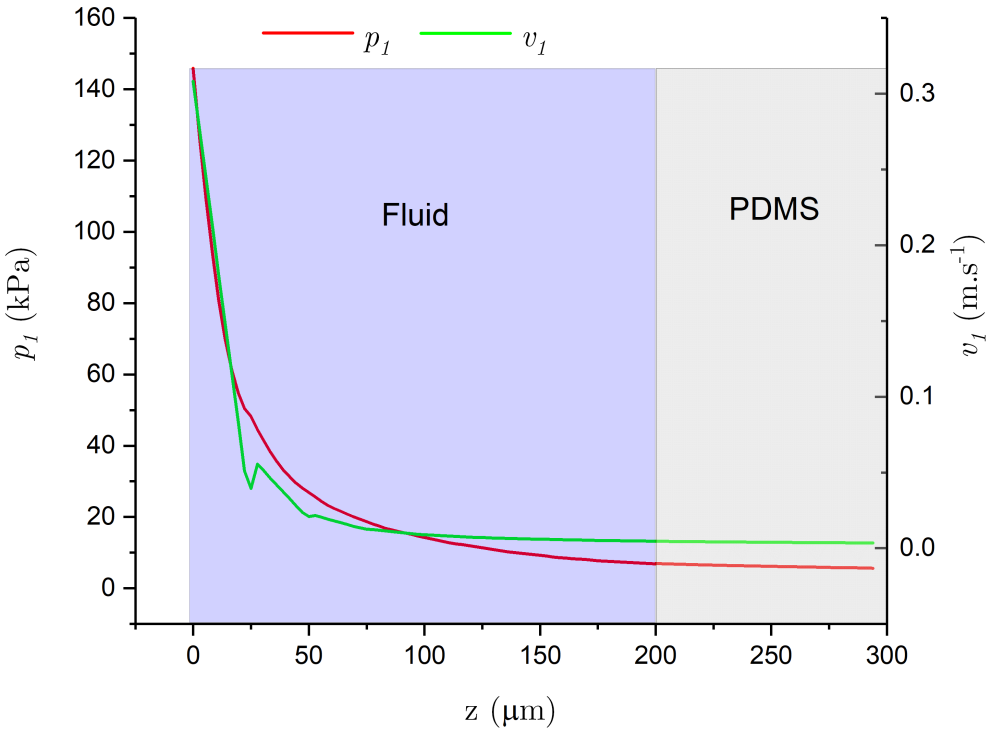

Figure 4.13: COMSOL simulations of a 3 MHz wave's pressure and velocity amplitudes in the fluid (blue) and PDMS (grey) layers as a function of depth at x = y = 0

While all of the simulations discussed thus far are valid for a single cell, we cannot extrapolate much information from this data about the behaviour of multiple cells, an element, or the entire array.

4.3.2 CMUT array

Simulating a large array of CMUTs in COMSOL is computationally expensive. Thus to better understand the pressure fields generated by the RC-CMUT array, numerical simulations were conducted using the Fast Object-Oriented C++ Ultrasound Simulator (FOCUS) program. FOCUS is a free, MATLAB-based, ultrasound simulation tool available at http://www.egr.msu.edu/~fultras-web/. FOCUS uses the fast nearfield method in

combination with an angular spectrum approach to give the emitted ultrasound field of an array [108]. It should be noted that FOCUS is optimized for piezotransducers not for MEMS-based transducers such as CMUTs. When a piezotransducer activates, the entire surface will deflect equally in a piston-like motion. However, when a CMUT oscillates, the clamped edges result in a higher deflection at the middle of the membrane than at the outer perimeter. Thus, the volume displacements between the two types of transducers is quite different. To better simulate the pressure amplitudes of a CMUT device, and maintain a piston-like motion model, a correction factor is required for the equivalent piston radius of a CMUT. It has been shown that the effective radius of a CMUT in a piston model, where the deflection is small compared to the thickness of the membrane, is about 68% of its total radius [64]. The simulated pressure amplitudes are still higher than expected and is a result of the simple FOCUS model that does not take into account factors like the membrane mass, and spring softening effect. As Figure 4.14a shows, even when using a corrected membrane radius in FOCUS, the result is a threefold increase in maximum pressure amplitude when compared to the equivalent COMSOL model discussed earlier. However, as the normalized pressure amplitudes are comparable (Figure 4.14b) the beam profile and pressure fields provided by FOCUS can be considered an adequate first-order approximation.

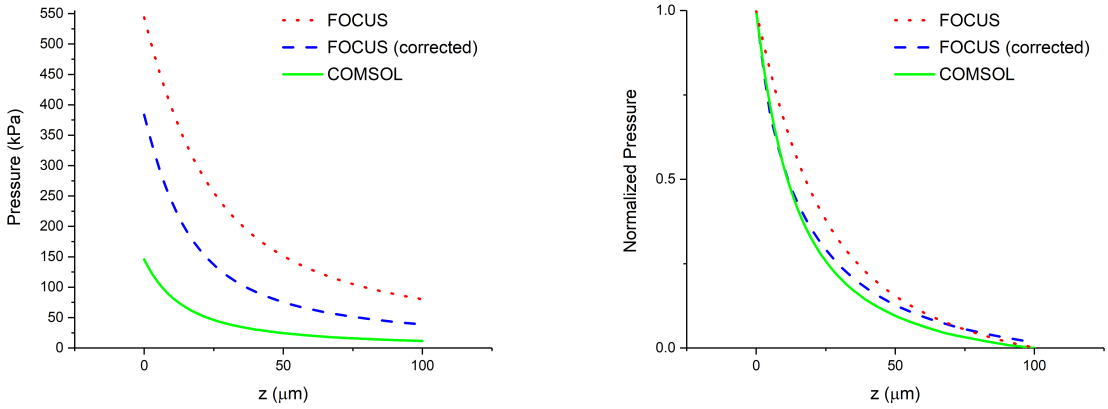

Figure 4.14: Comparison of the COMSOL and two FOCUS simulations (original and corrected membrane radius) of travelling wave a) pressure amplitudes in the fluid for a single CMUT cell as a function of depth at x = y = 0; and b) normalized pressure amplitudes

A facile method was used to approximate the standing wave pressure profile of a CMUT element, and by extension, the array. First, a single 380 μm square element of 25 cells was simulated as shown in Figure 4.15a. To maximize fill factor, the 60 μm diameter cells were arranged with a diagonal pitch of 70 μm. The normalized pressure profiles were calculated as a function of depth (distance normal to the transducer surface), as seen in Figure 4.15b, and also in the plane of the transducer surface (see 4.15d) which showed a strong spatial pressure variation due to the pattern of the CMUT cells. Although the pressure profile is calculated within a finite volume, FOCUS defaults to assume that the medium extends infinitely in all directions. For an example of the FOCUS code used please see Appendix H. The pressure matrix obtained through FOCUS was truncated to a depth equivalent to the expected $\lambda/2$ resonator and then the data was summed with its reflected self. The corresponding standing wave pressure profile of a single element in a $\lambda/2$ resonator is shown in Figure 4.15c.

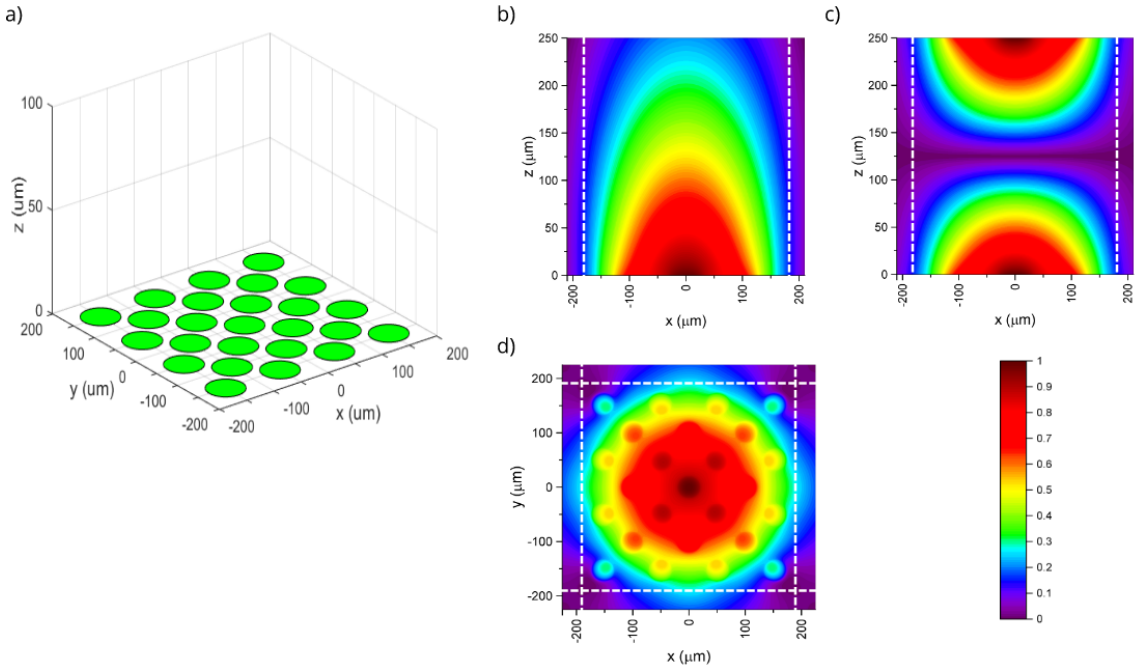

Figure 4.15: FOCUS simulation of a) an immersed CMUT element operating in water at 3 MHz; and the corresponding normalized pressure amplitude profile at y = 0 in the x-z plane of b) a travelling wave; c) standing wave with a glass reflector at z = 250 μm; and d) the travelling wave pressure amplitude profile at z = 0 in the x-y plane. Dashed white lines indicate the projection of the element's edges (element width)

Next, several simple arrays of CMUT elements shown in Figure 4.16a were chosen and their pressure profiles calculated. The corresponding standing wave pressure profiles, normalized to the highest value in water, are shown in Figure 4.16b. Each of the arrays' standing waves have pressure nodes located in the center of the channel. Of particular interest is the 2×2 element array which the model predicts will generate the highest pressure regions along the length of the subset.

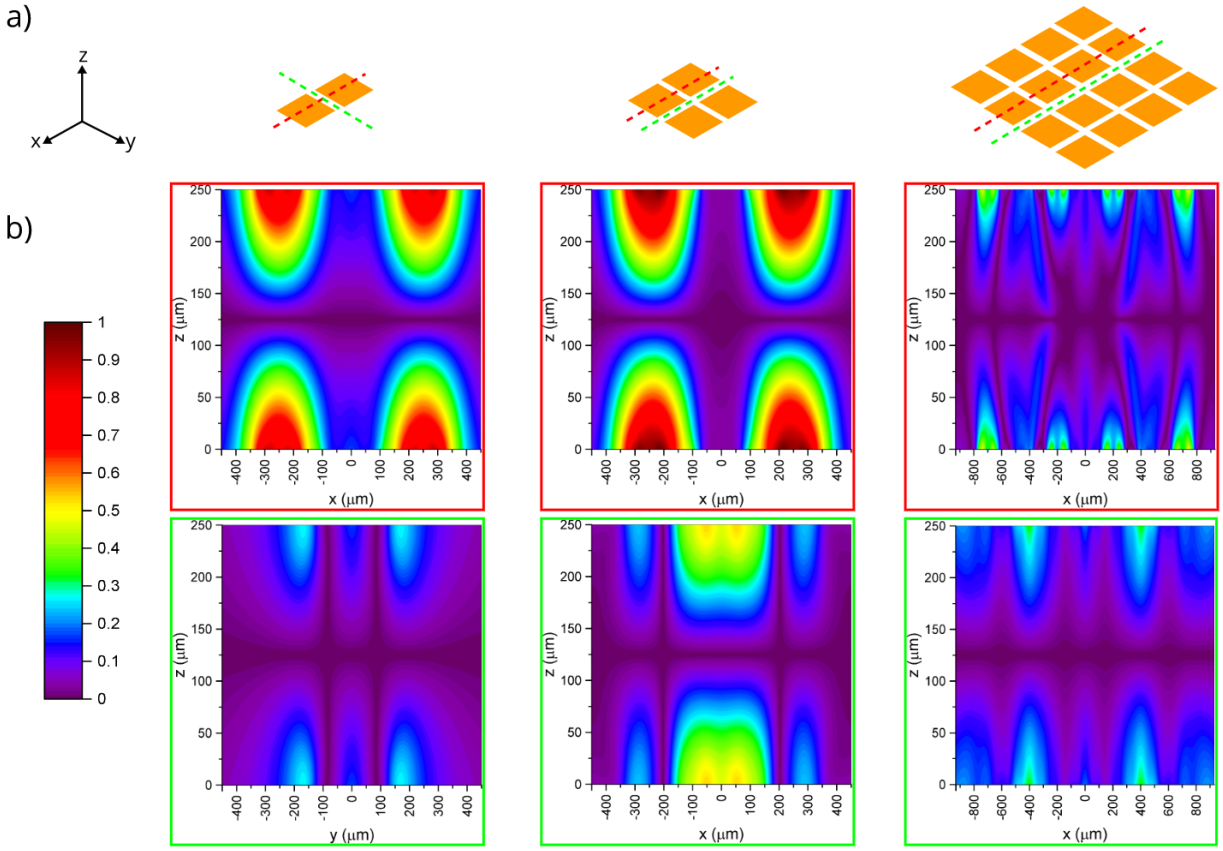

Figure 4.16: a) 1×2, 2×2, and 4×4 CMUT arrays operating in water at 3 MHz, with selected planes of interest indicated with red or green dashed lines; and FOCUS simulations of their b) normalized standing wave pressure profiles (red or green border corresponding to planes of interest) for a glass reflector at z = 250 μm

This seems counter-intuitive, since it could be expected that the more elements are activated the higher the output pressure should be. The pressure fields in these cases are complex and, absent speculation, requires further exploration through finite element analysis and experiment.

Next, a slightly more elaborate combination of arrays was examined. First, the activation of 2×2 corners in a 6×6 array was simulated (see Figure 4.17a). Clearly, the space between active transducers have lower pressure amplitudes (Figure 4.17b); therefore, we might expect particles to trap and form agglomerates above each of the four corner regions. The larger the separation between active and inactive subsets the greater the likelihood of creating such discrete trapping regions.

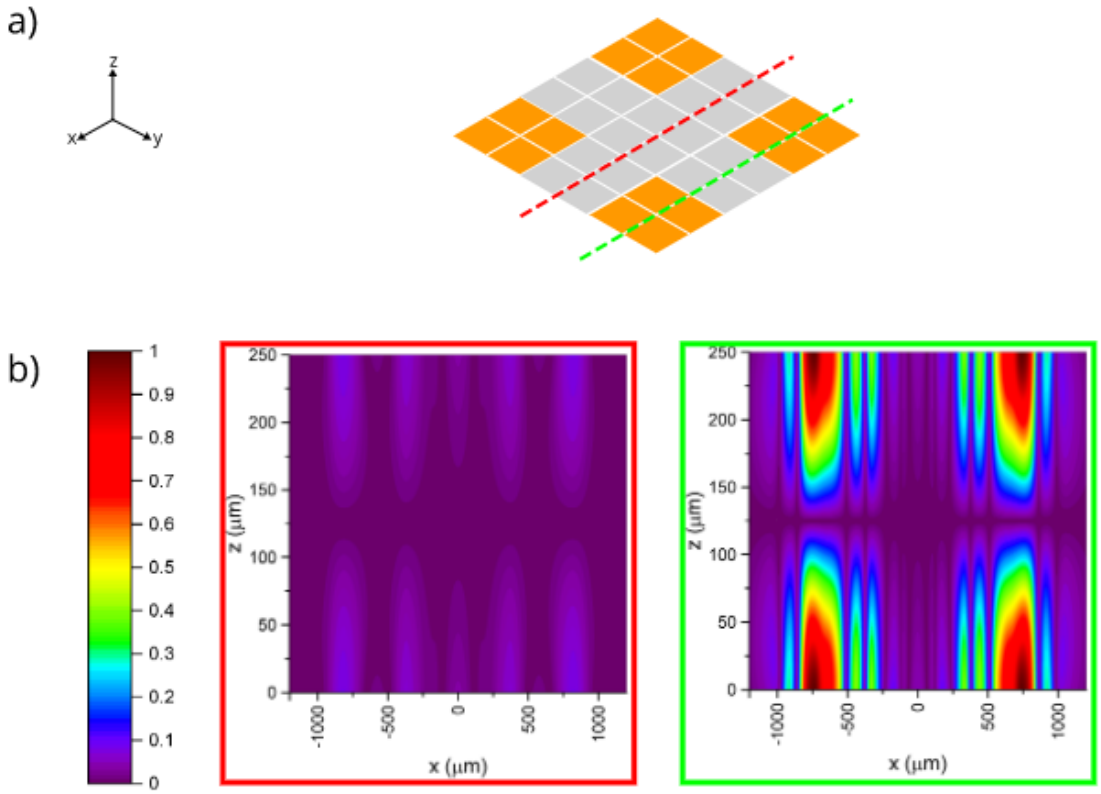

Figure 4.17: a) Four 2×2 elements activated in a 6×6 array, operating in water at 3 MHz, activated subsets are indicated in orange and selected planes of interest indicated with red or green dashed lines; and FOCUS simulations of their b) normalized standing wave pressure profiles (red or green border corresponding to planes of interest) for a glass reflector at z = 250 μm

Due to the finite dimensions of the transducer elements, just as in the single CMUT cell, there is also an F_{grad} component acting perpendicular to the wave propagation. This lateral trapping region can be moved by activating and deactivating subset patterns of the array as shown in Figure 4.18a. As the pressure gradient is translated (Figure 4.18b), so too will particles that were captured within the trapping region. In this manner, precise particle manipulation may be achieved along a CMUT microarray.

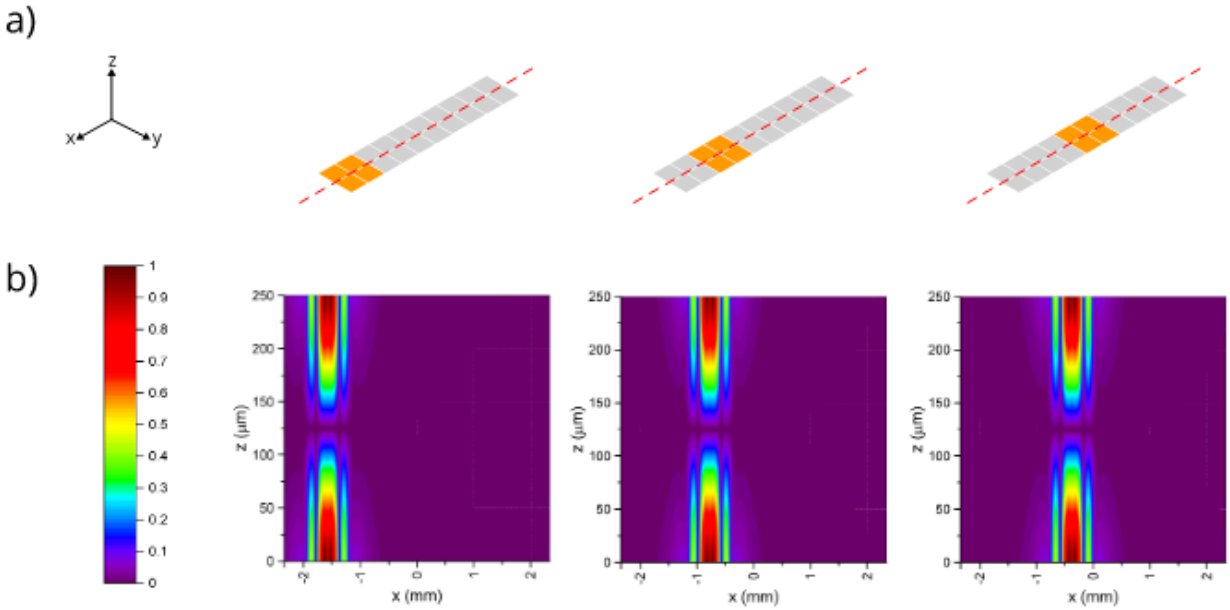

Figure 4.18: a) 10×2 CMUT array, operating in water at 3 MHz, with sequentially activated 2×2 subsets, activated subsets are indicated in orange and the selected plane of interest indicated with red dashed lines; and FOCUS simulations of their b) normalized standing wave pressure profiles for a glass reflector at z = 250 μm

4.4 Fabrication

A 32×32 RC-CMUT array was fabricated using a wafer bonding process (please see Appendix I). Each square element had side lengths of 380 μm within which 25 circular cells of 60 μm diameter are arranged. For collapse voltage characterization a CMUT membrane was first immersed in oil and observed under a microscope as increasing bias voltage was applied. When the semi-transparent membrane contacted the bottom of the cavity a visible change in contrast to the membrane region was seen. In this manner, the observed V_c was about 110 V. When membrane deflection was measured using a vibrometer (Polytec OFV-5000) the V_{bias} was kept to 60 VDC and driven with a 20 V_{p-p} AC signal. Vibrometer measurements show a resonance frequency of 3 MHz ± 100 kHz from cell to cell and displacements of 19 ± 4 nm (see Figure 4.19). It is likely that there were three sources causing these variations. One may have been inconsistency in the thickness of the CMUT membrane. The manufacturer of the SOI wafers (Ultrasil, Hayward, CA, USA) claims an expected variation in the device layer (i.e. the CMUT membrane of our device) of around 0.5 μm. Another reason may be contamination within CMUT cavities further reducing their depth from original design parameters. Finally, it may be mutual acoustic impedance effects from multiple neighbouring CMUT cells when operating in a fluid, which can manifest as frequency response variations amongst cells in an element [109].

The microchannel for travelling wave, flow operation was fabricated by sandwiching two layers of patterned, 100 μm thick, double-sided, Kapton tape (Ted Pella, Inc., Redding, CA, USA) between the CMUT device and a silicone elastomer top (Sylgard 184, Dow Corning, Midland, MI, USA) of thickness 500 μm. A Y-shaped microchannel having widths of 2 mm was patterned on to the Kapton tape by laser engraver (VLS2.30, Universal Laser Systems, Scottsdale, AZ, USA). The engraver employs a 10.6 μm wavelength, CO_2 laser, capable of outputting a maximum power of 30 W. To prevent uncontrolled thermal damage to the Kapton material, yet successfully transfer the microchannel pattern through the entire Kapton thickness, a low-power, high-repetition scheme was used. With laser power reduced to 0.75 W a hundred passes with the laser were needed to create the microchannel. The silicone forming the top of the microchannel was cut to cover the entire working area of the CMUT using a scalpel. The inlet and outlet ports were fashioned from sections of 32 gauge needle and punched through the top of the microchannel. Beads were introduced through the left port and washing fluid through the right with a common outlet downstream. For a diagram of the CMUT microchannel device please refer to Figure 4.20.

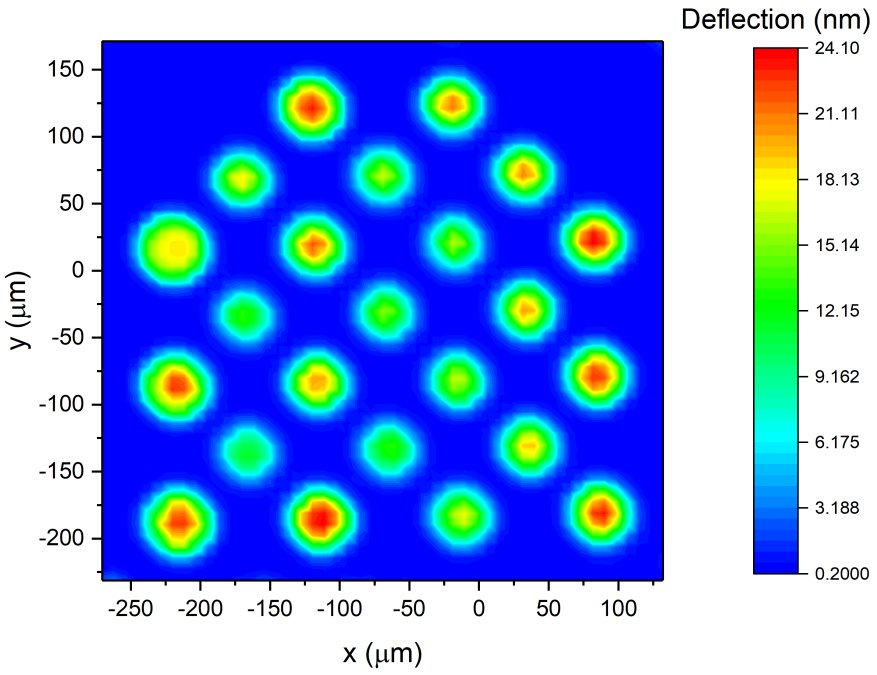

Figure 4.19: Vibrometer measurements of an oil immersed element of the CMUT array

For standing wave experiments a microchannel with a height of 259 μm was required. This was accomplished by using two layers of the Kapton double sided tape (as used in the travelling wave microchannel) sandwiching two more layers of DuPont 120FN616 Kapton film. The Kapton film has a 25.4 μm thick polyimide core that is coated on both sides with a 2.5 μm thick, heat sealable, Teflon FEP fluoropolymer layer. The Kapton layers were wrapped in aluminum foil and baked on a hot plate, under compression, for 20 minutes at 280 °C. With the Kapton layers now heat sealed, a single 3.5 mm wide microchannel pattern was transferred via laser. Borofloat glass with a thickness of 500 μm was used to fashion an optically transparent and acoustically reflective layer. The laser cutter was used a final time to size the glass and create the inlet and outlet holes. Much like the Kapton layers, to prevent thermal damage and cracking, multiple laser passes (150) at low power (3 W) were used. However, given the thickness of the glass, the laser passes were performed at three different focal depths (0, 250, and 500 μm).

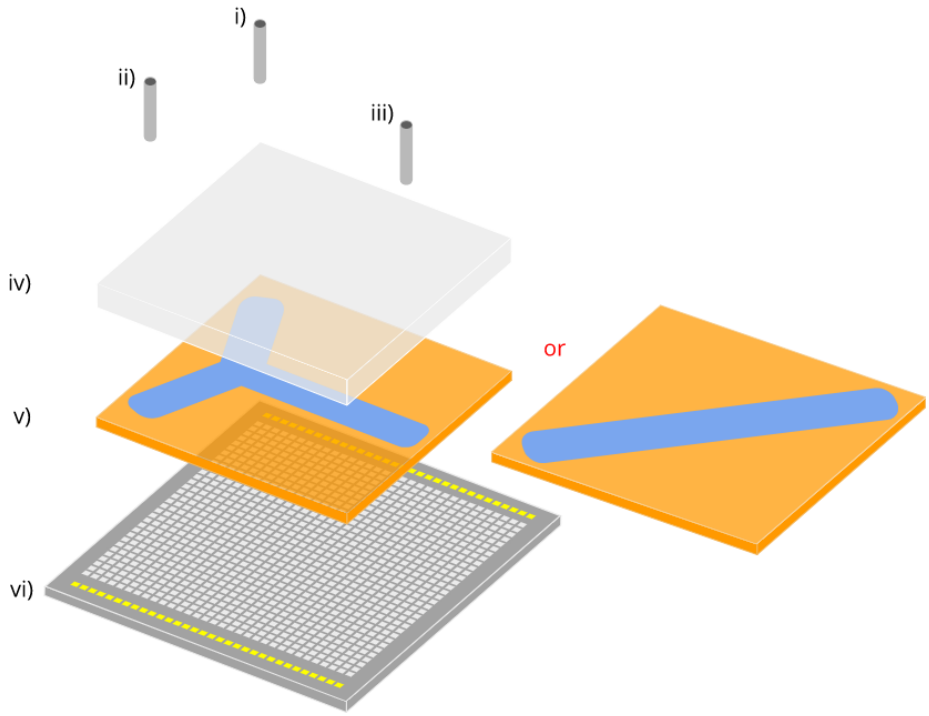

Figure 4.20: An exploded view diagram of the CMUT microchannel assembly with i), ii) inlet ports for wash fluid and bead solution respectively; and iii) a single outlet port; iv) 2 mm thick silicone elastomer (PDMS) top layer (for travelling wave experiments); or 500 μm thick glass (for standing wave experiments); v) Y-shaped microchannel (for travelling wave experiments) patterned into a 200 μm thick, double-sided, Kapton tape; or a wider single microchannel (for standing wave experiments) patterned into a 259 μm thick combination of double-sided Kapton tape and Kapton film; vi) 32×32 array CMUT

4.5 Experiments

The CMUT device was wirebonded to a homemade circuit board fabricated on a copper plate, interconnects were laser cut on an adhesive tape (3M Canada, London, ON, Canada) mask, and then etched in a standard ferric chloride solution (MG Chemicals, Burlington, ON, Canada). To protect the wirebonds, a thin layer of silicone elastomer was deposited where interconnects were located, along the two edges of the CMUT. An aqueous solution of 4 μm silica beads (Polysciences, Inc., Warrington, PA, USA) was diluted from stock to 4.97×10^6 ml^{-1}. For droplet testing, 10 μl of the bead solution was placed on top of the CMUT array, and a bias voltage of 60 V DC was applied to the CMUT elements of interest

using a power supply (GW Instek, New Taipei City, Taiwan) before applying a sinusoidal driving voltage of 20 V_{p-p} AC (BK Precision, Yorba Linda, CA, USA). For experiments under flow, bead solutions were pumped at flow rates of 20 μl min^{-1} unless otherwise noted. All experiments were observed via a CoolSNAP EZ camera (Photometrics, Tuscon, AZ, USA) mounted to an optical microscope (Nikon, Tokyo, Japan). A picture of the device without fluid ports installed is provided in Figure 4.21.

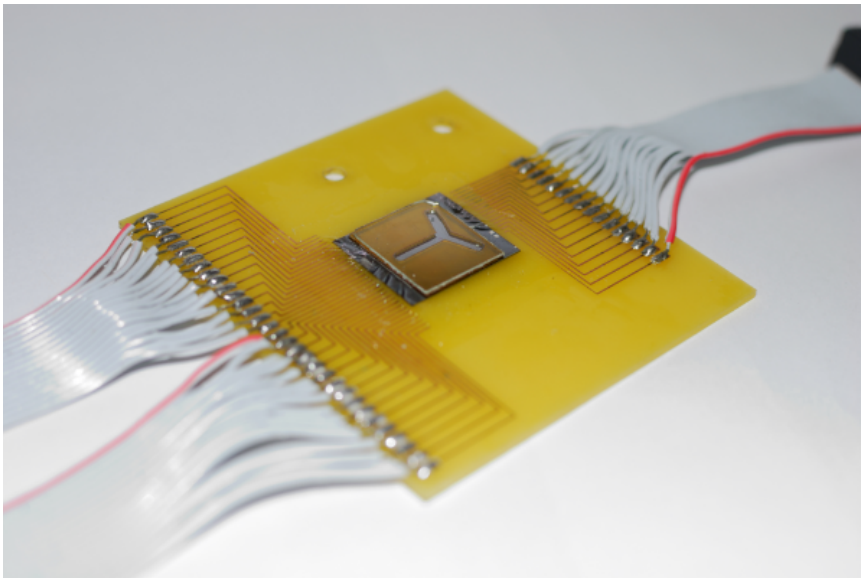

Figure 4.21: A photograph of the CMUT assembly, used in standing wave experiments, after wirebonding, silicone elastomer protection, Kapton microchannel and glass reflector installed

4.5.1 Travelling wave

Droplet operations

To observe the gradient forces of the travelling wave, 5 μL droplets of 4 μm silica beads were placed on the CMUT surface and examined under a microscope. Droplets were dispensed by manual pipette thus some variation in droplet volume and shape was expected; however, typical droplets were approximately 3 mm wide and 0.5 mm tall. The beads appeared evenly dispersed before ultrasound activation (see Figure 4.22a). After activation at 3 MHz the beads began to agglomerate into clusters at the center of the CMUT cells (see Figure 4.22b). At this single frequency operation some clusters exhibited tighter packing of particles than others. We can attribute this to the variations in resonance frequency between cells as revealed by the vibrometer. By executing a linear frequency sweep from 2.9 to 3.1 MHz over a 10 ms period we can remedy this performance difference (see Figure 4.22c). When switching the CMUT cells off we can observe a broadening of the agglomerated particles (see Figure 4.22d). The short ($\leq$10 μm) lateral distances that the particles travel after the acoustic field is turned off indicates that the agglomerated beads were very close to or on the CMUT membrane surface and not suspended higher in the fluid. These results are in good agreement with the expected behaviour of the beads in the COMSOL model. Video of the device in operation is available in Appendix A.

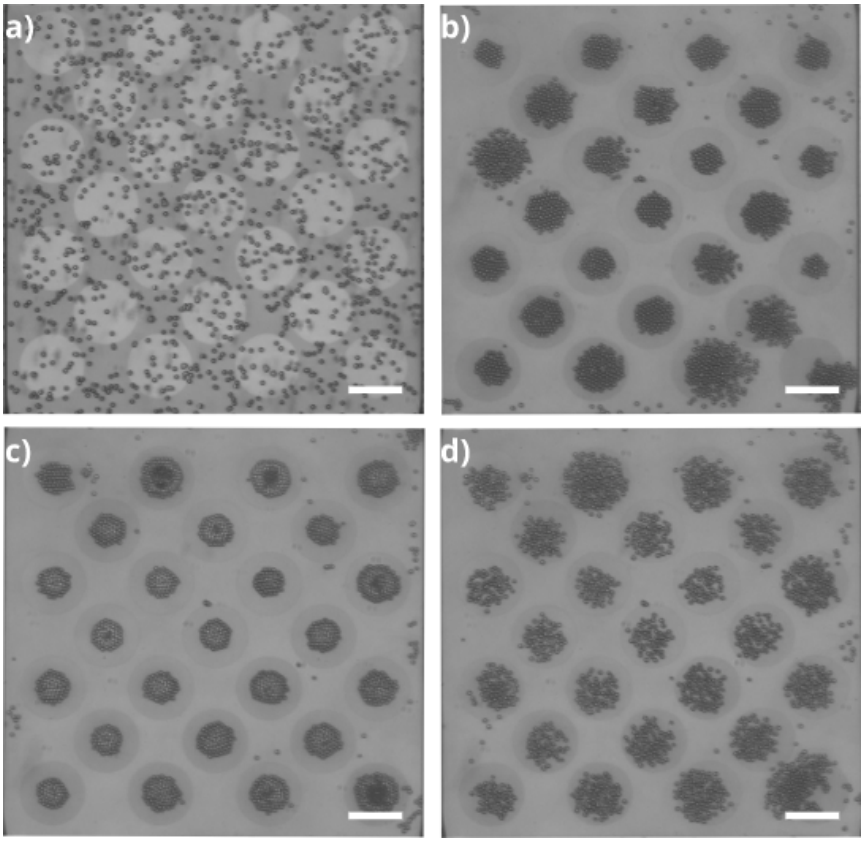

Figure 4.22: Micrographs of the surface of a single CMUT element consisting of 25 cells with a droplet of 4 μm silica bead solution, a) before; and one minute after b) single frequency ultrasound activation; c) frequency sweep activation; d) ultrasound deactivation. Scale bars represent 50 μm

We then investigated wider and slower frequency sweeps, with 1 to 3.1 MHz linear sweeps at a period of 15 s. The slower sweeps were equivalent to driving the CMUTs at a series of discrete frequencies. In Figure 4.23a we show a sequence of images of a bead cluster on a single CMUT cell as the frequency sweep is applied. The trapped bead aggregates could be palpated by expanding and contracting the discrete clusters. This palpating motion of the bead clusters can be explained by the behaviour of the pressure amplitude of the CMUT cell as it undergoes a frequency sweep. Figure 4.23b shows a FEM analysis of p_1 in the y-z plane as the membrane drifts off resonance and back on again. Intuitively, the drop in pressure amplitude must be accompanied by a drop in F_{grad} (Figure 4.23c) and this can be thought of as the CMUT's "grip" on the particle cluster relaxing

and the particle cluster being squeezed less. Video of bead cluster palpation is available in Appendix B.

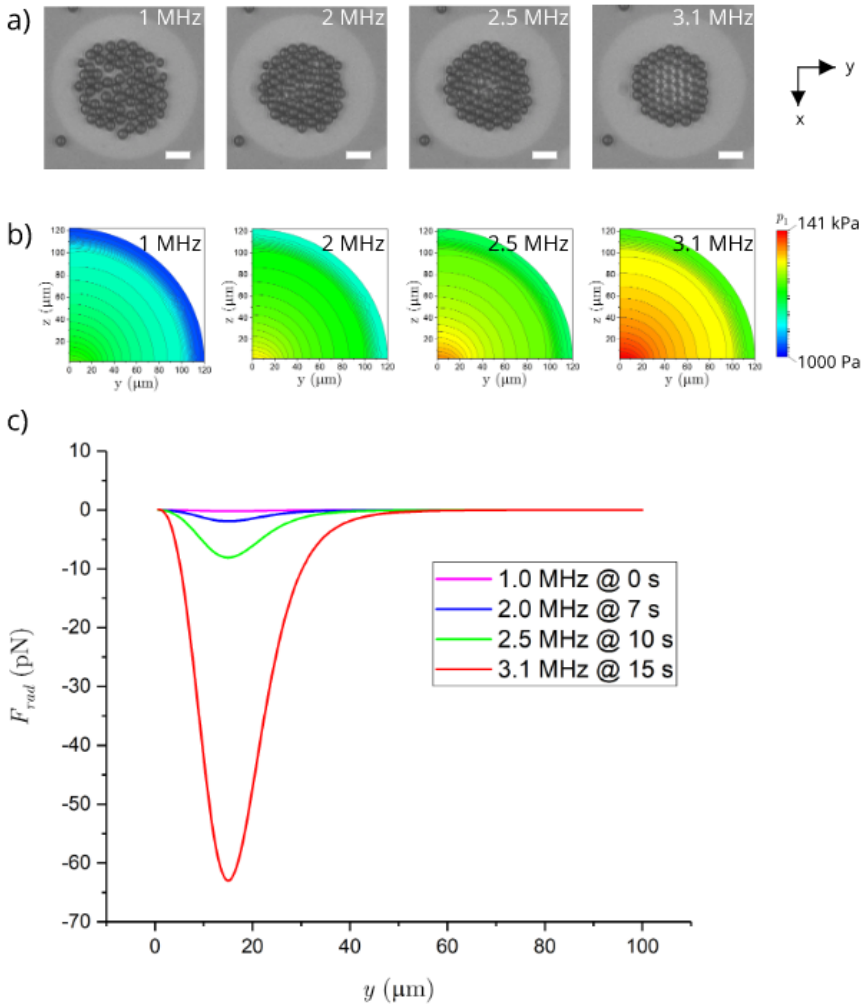

Figure 4.23: Micrographs a) of a typical bead cluster over a single CMUT cell undergoing a linear frequency sweep from 1 to 3.1 MHz over a 15 s interval. Scale bar represents 10 μm; and COMSOL simulations b) of their corresponding pressure amplitudes in the y-z plane; and c) the lateral gradient force at the surface of a CMUT cell as frequency is swept. Pressure scale is logarithmic

Flow operations

When the 2 mm wide and 200 μm thick microchannel was incorporated onto the CMUT device, trapped particles were tested against flow. The width of the microchannel enclosed four elements. Using a short and fast frequency sweep regime (2.9 to 3.1 MHz in 10 ms) particles were introduced through one port and trapped at a volumetric flow rate of 2 μl·min^{-1}. Particle flow was stopped and DI water was introduced through the wash port at 2 μl·min^{-1} and then steadily increased. To determine the trapping force of the device a single particle was trapped to a CMUT cell and the flow rate of the syringe pump increased at 1 μl·min^{-1} increments until the bead no longer appeared over the CMUT cell. The trapping experiment was repeated ten times and the velocity reported by the syringe pump immediately prior to the loss of the bead was recorded. These volumetric flow rates were converted into linear fluid velocities by taking into account the cross sectional area and parabolic flow profile of the microchannel, for an explanation of this conversion please see Appendix G. Inputting the linear fluid velocities into equation 2.20 we determined the trapping force acting on the beads to be 64 $\pm$ 1 pN, corresponding to a maximum linear fluid velocity of 1.9 $\pm$ 0.2 mm·s^{-1}). This matches very well with the our model in Figure 4.5b that predicted a lateral gradient force of 63 pN. The trapping force also compares comfortably to other microparticle trapping techniques such as optical tweezing, and dielectrophoresis, but higher than most magnetophoretic devices [110, 111]. It should be noted that a small number of beads often stuck to the surface of the CMUT, either on the cells or in the space between them; these stuck beads were distinguishable from acoustically trapped beads, as the telltale oscillations that occur with increased sweep period were not present.

After trapping bead agglomerates at one CMUT cell it was also possible to transport them to another cell directly downstream. This was facilitated by briefly turning off the AC voltage signal, thereby allowing the beads to re-enter the laminar flow, and then reactivating the AC voltage to trap the beads when they had reached the new target cell. This sequential trapping process is shown in Figure 4.24 and available as a video in Appendix C.

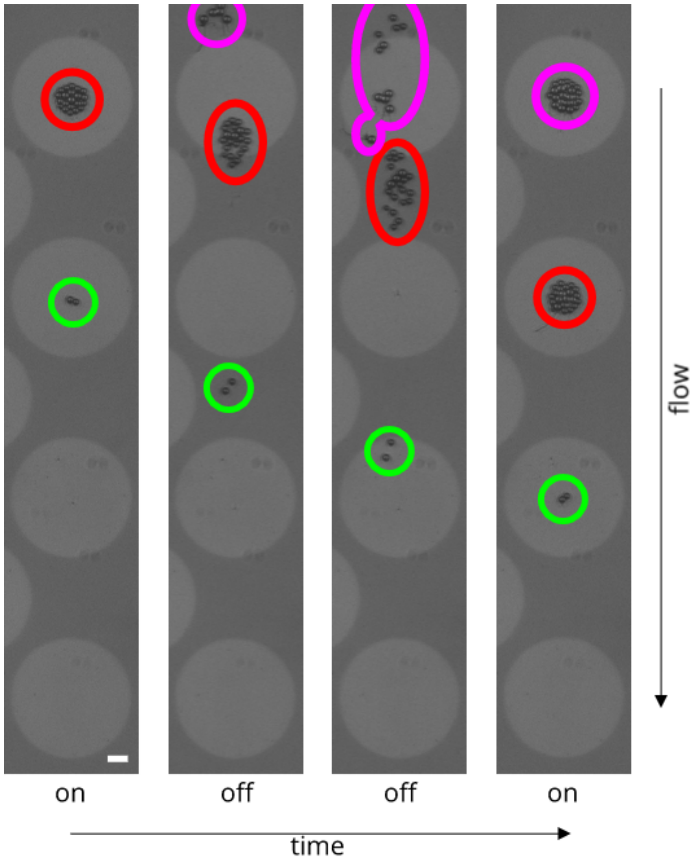

Figure 4.24: Micrographs of bead transport by initially trapping bead clusters (highlighted in ellipses), then deactivating the AC voltage allowing clusters to join the 20 μl·min^{-1} flow, and finally activating the CMUTs again after beads moved to the next consecutive cell. Scale bar represents 10 μm

The bead cluster palpating witnessed in droplet mode operation could also be replicated under flow. Using a wide and moderate frequency sweep regime (2.9 to 3.1 MHz in 100 ms) and at lower flow rates ($\leq$ 5 μl·min^{-1}) the trapped bead clusters could be made to breathe as in the droplet case (Video available in Appendix D). However, under fast flow conditions ($\geq$ 20 μl·min^{-1}) and at the same sweep periods the beads could be pushed off their trapped positions in the direction of the flow before being pulled back toward the center of the CMUT cell. The oscillations may again be explained by the drop in F_{grad} as the CMUT cells are driven off-resonance; at long sweep periods the drag force acting on the particles can temporarily overcome the lateral acoustic gradient force.

Finally, we attempted to leverage the laminar flow of the microchannel alongside threshold AC voltage operation of the CMUTs (i.e. where the gradient force would be too low to trap beads but high enough to alter the bead trajectory) to see if beads could be gradually separated into discrete flows. This separation operation was achieved at a flow rate of 20 μl·min^{-1} by configuring the CMUT array to first capture a large population of beads with an upstream section of the CMUT array operating at 20 V_{p-p} AC (Figure 4.25) and then switching the driving signal to a downstream section of the array at, a much lower, 1 to 5 V_{p-p} AC, where beads would form lines over consecutive CMUT cells.

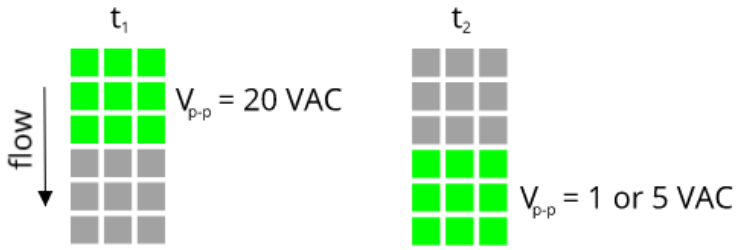

Figure 4.25: Configuration of the CMUT array at time t_1 where the upstream section of the array is activated at 20 V_{p-p} AC for bead capture, and at a later time, t_2, where the downstream section of the –array is activated at a lower 1 or 5 V_{p-p} AC for bead separation. Green squares are active elements and grey squares are inactive

The somewhat arbitrary distribution of the captured beads at the upstream location (Figure 4.26a) results in different widths of discrete flows downstream (Figure 4.26b). In general, the discrete bead lines appear to taper in the direction of flow. This indicates that, with a long enough CMUT array, the separation between bead lines is only limited by the pitch (cell-to-cell distance) of the CMUT device in the direction perpendicular to the flow. The small variation in threshold voltage required for separation was attributed to

differences in performance from cell to cell of the CMUT microarray. Video demonstrating this discrete bead line formation is available in Appendix E.

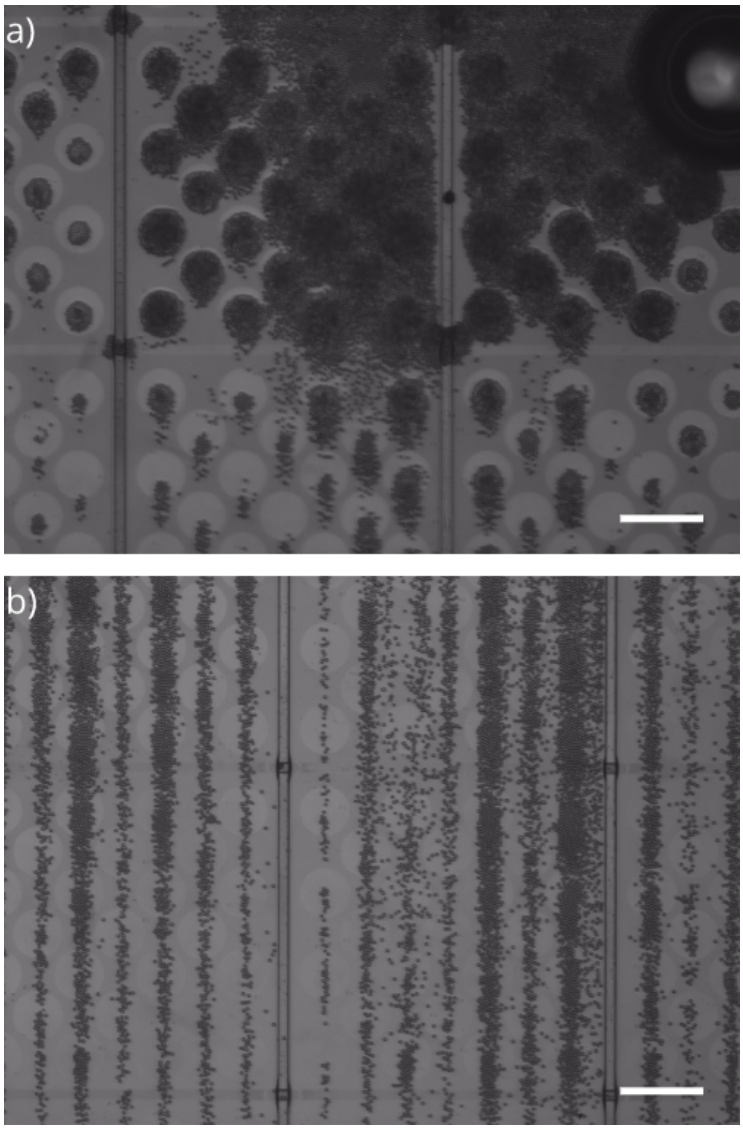

Figure 4.26: Micrographs of the areas of interest a) upstream region where the CMUT array was trapping a large population of beads; b) bead separation into discrete lines at low voltage operation of the downstream CMUT array. Flow is 20 μl min^{-1} and from top to bottom. Scale bars represents 100 μm

4.5.2 Standing wave

Operations involving standing waves were conducted with solutions of 10 μm fluorescent polystyrene beads. The larger beads were chosen to increase the F_{grad}, as discussed previously. Furthermore, the use of fluorescent beads would make it easier to distinguish from background as the expected plane of bead aggregation is the center of the microchannel rather than at the device surface. Beads were pumped into the standing wave microchannel at a volumetric flow rate of 20 μl·min^{-1} and stopped after a sufficient portion of the microchannel was filled (see Figure 4.27a). Selected CMUT elements were then activated at 2.9MHz. First, each of the simpler array patterns that had been simulated were observed. The 1×2, 2×2, and 4×4 arrays were alternately tested at different locations on the microchannel. The results were puzzling. Bead agglomeration was most successful with the smaller 1×2 and 2×2 arrays. Beads would leave the field of view (FOV), form small clusters off screen, and then re-enter the FOV to create larger aggregates. However, this agglomeration process occurred very slowly, 30 to 40 minutes (see Figure 4.27b-d), as opposed to the 30 to 100 seconds typically reported in literature [44, 112]. The effectiveness of the arrays also varied greatly with location on the CMUT device, with some areas showing little to no evidence of agglomeration when array patterns were activated.

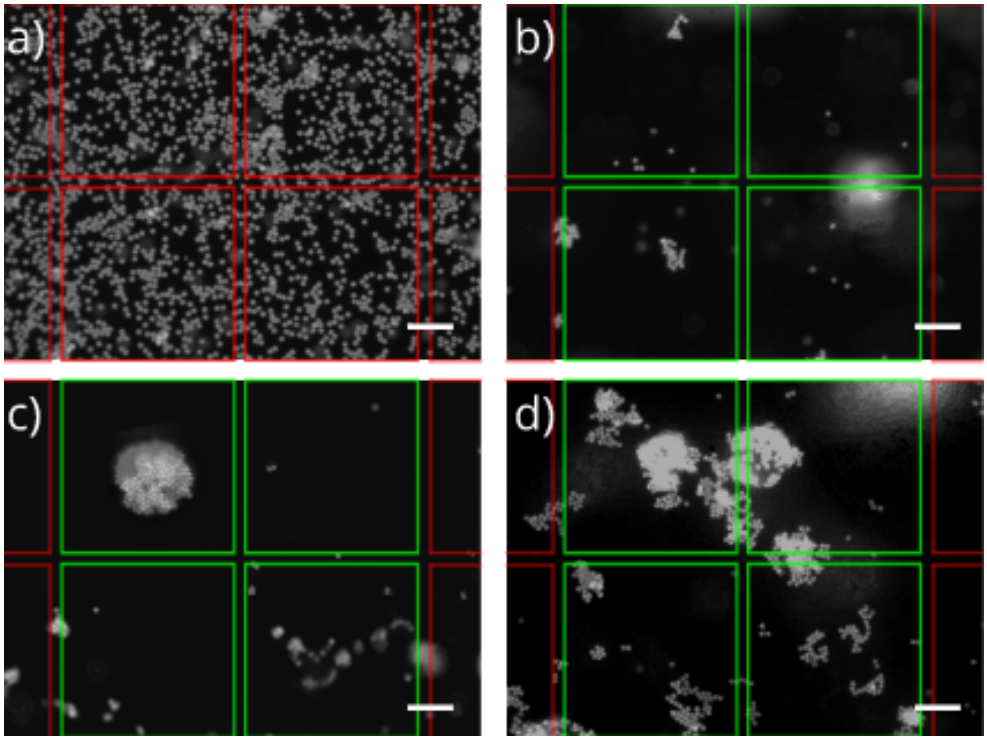

Figure 4.27: Micrographs of 10 μm fluorescent polystyrene beads in the middle of the standing wave microchannel, a) before activation; and after activation of a 2×2 array for b) 10 min; c) 20 min; and d) 40 min. Inactive elements are in res and active elements in green. Scale bars represent 100 μm

Activation of the more complex 2×2 corners in a 6×6 array was also attempted. Aggregation at the four corners was not observed. Instead, a semi-stable microflow briefly trapped and rotated bead aggregates near the center of the activated array (see Figure 4.28). The center of rotation and number of aggregates in the FOV changed over time before aggregates fell out of the plane of focus or exited the FOV altogether. Video of the aggregate rotation is available in Appendix F.

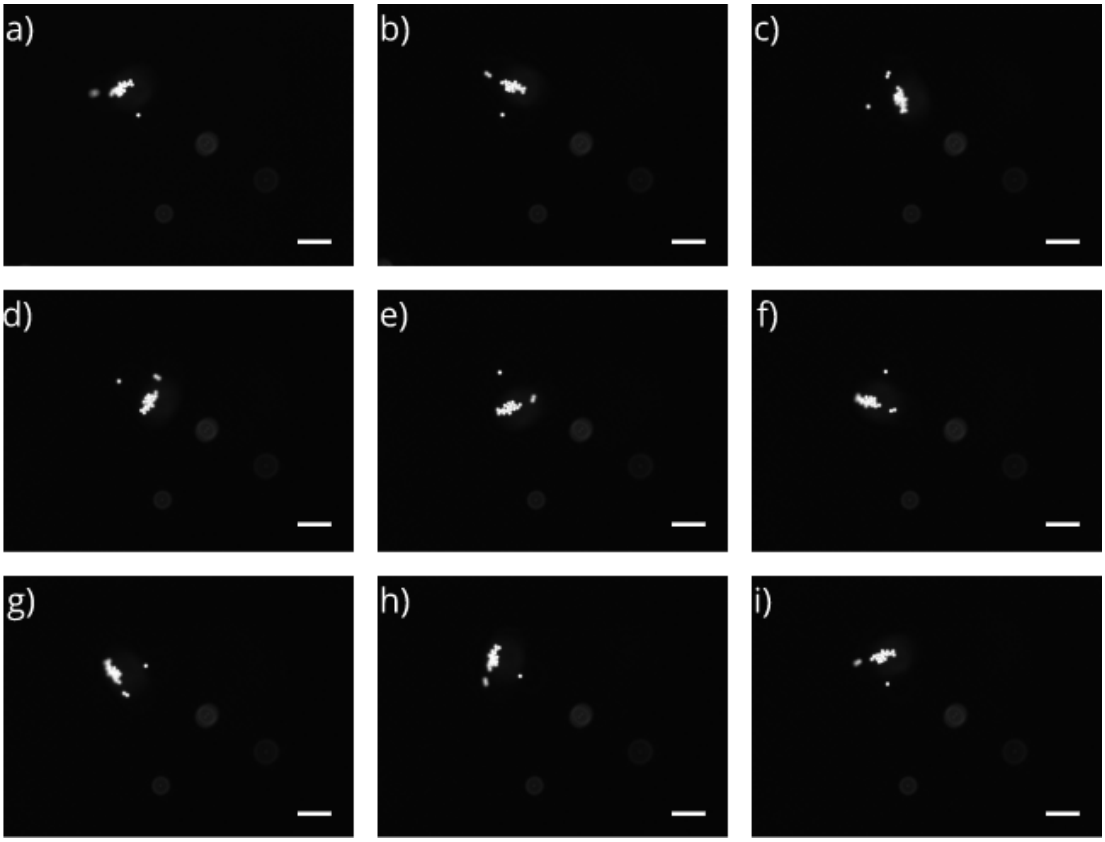

Figure 4.28: Micrographs of 10 μm fluorescent polystyrene bead aggregate rotating in the middle of the standing wave microchannel, after activation of a 2×2 corners in a 6×6 array, consecutive frames are separated by 1.5 sec. Scale bars represent 100 μm

The translation of beads along the microchannel by sequential 2×2 array activation was another casualty of the variation in CMUT standing wave performance with location. Aggregates that were formed above one array would then very slowly "smear" after its closest neighbour array was activated. Even after 30 to 40 minutes of operation the beads would not re-aggregate over the next array (see Figure 4.29). There were no observed streaming effects counteracting the gradient force traps. It may be that there was poorer overlap of pressure fields from the neighbouring arrays than expected through simulation.

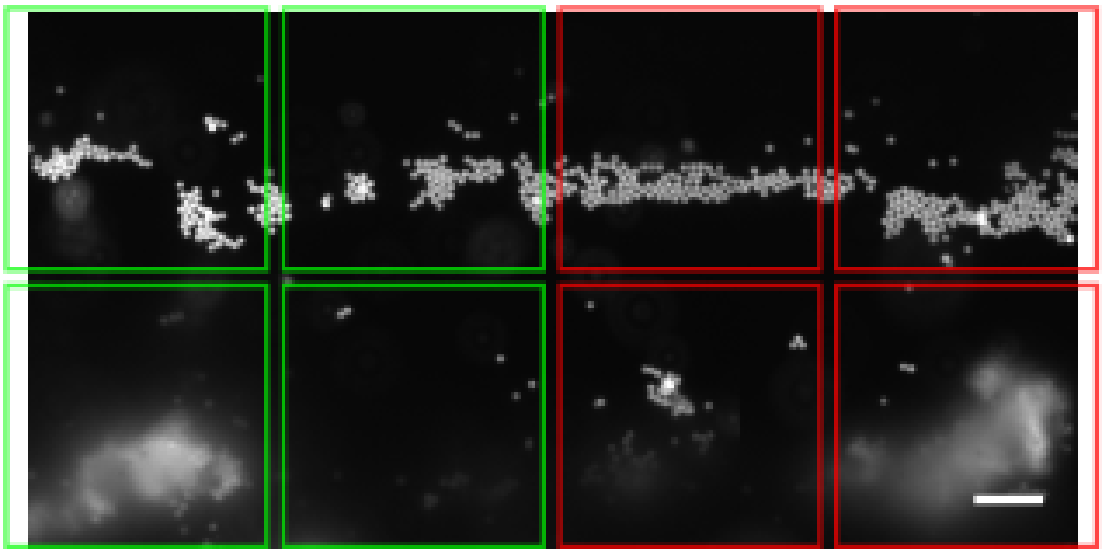

Figure 4.29: Micrograph of 10 μm fluorescent polystyrene bead aggregates in the middle of the standing wave microchannel, 40 minutes after deactivation of one 2×2 array (location outlined in red) and activation of a neighbouring 2×2 array (location outlined in green), this is a composite image stitched from two frames taken at different microscope stage locations. Scale bars represent 100 μm

4.6 Discussion

This chapter demonstrated that CMUT platforms can manipulate microbeads within droplets, and under flow conditions. How might such particle manipulations be useful?

The large surface area to volume ratio of microbeads have made them enticing targets for treatment with functional groups. This has resulted in a plethora of functionalization options, making microbeads a preeminent platform for multiplexed assay applications [113, 114]. Subsequent developments in microfabrication have also seen bead-based assays moving from the popular static microwell plate to the dynamic setting of a microfluidic chip [115]. While this shift to a microfluidic environment has resulted in the typical efficiencies of scale (*e.g.*, sample volume reduction, increased sensitivity), flow conditions have necessitated techniques for immobilizing beads. Bead trapping allows for real-time observation during assay operations such as measurement and washing steps.

The CMUT device we have described and shown meets these requirements. First, the

microarray layout of the device provides multiple, highly localized sites for particle capture. The CMUT cells that act as particle traps can be fabricated to much smaller dimensions than typical piezotransducers. Thus, the high precision in acoustic manipulation we have demonstrated with our CMUT device is not possible with a system based on conventional piezotransducer technologies. Our device also allows for easy transport of particles and particle clusters from cell to cell; this may be useful in multiplex assays. The unique palpating action possible through CMUTs could also be used to provide thorough access to beads during washing steps while still remaining trapped for observation.

Biosensing applications may be another avenue worth exploring for travelling wave CMUT devices. The limiting factor in many biosensor applications, especially at the nanoscale, is analyte mass transport times [116]. Acoustically delivering bead-conjugated analytes to a localized area, such as the surface of a CMUT, could decrease biosensor response times. Furthermore, the tight packing of CMUT cells could enable a single device to test for multiple analytes at the CMUT element or array level, fulfilling the true potential of Lab-on-a-Chip.

The poor performance of the CMUT device in standing wave mode may be largely due to the variation in resonance frequency between CMUT cells as revealed during vibrometer characterization (see section 4.4). When driving the CMUT cells at a single frequency of 2.9 MHz, the variation in each cell's membrane deflection may result in a weakly formed standing wave pressure field. Here, driving the elements with a frequency sweep (as was done in the travelling wave experiments) was not a potential solution, as the higher frequencies would not enable us to form coherent standing waves in a 259 μm deep microchannel. The locational difference in array performance might be similarly explained as selected elements having a majority of cells with resonance frequencies outside 2.9 MHz. This is likely to indicate a need for better process controls during CMUT fabrication. For example, variations in the cavity depth of a CMUT can reduce their transmission efficiency. This is quite possible if leftover photoresist or contaminants remain after etching.

Another potential source of error may be variations in the thicknesses of the different layers of the device. Namely, the SOI wafer membrane and Kapton tape and film microchannel. The manufacturer provides nominal thickness information on Kapton products with no deviation range. Profilometer measurements taken of a single layer of Kapton tape show a $\pm$ 1 μm on the manufacturer reported 100 μm thickness. The SOI wafer, likewise, varied by as much as 0.5 μm according to the manufacturer.

The very slow agglomeration of beads in our device is indicative of weak lateral gradient trapping forces. As a consequence, the CMUTs had to operate continuously for very long periods of time. This increases the likelihood of dielectric charging and would further reduce

the performance of the CMUT. An examination of the CMUT devices after operation also showed membrane failures on some cells. These manifested as entire cell membranes debonding from the insulating layer, or shedding portions of a membrane in micrometer-sized flakes.

The presence of a microflow with a circulation plane that was parallel to the transducer surface was unexpected. The more commonly encountered Eckart and Rayleigh types of streaming operate, in most cases, on a plane perpendicular to the transducer surface. An explanation may be offered by Lei *et al*, whose work has described similar streaming flows as an interplay between standing and travelling waves at the edges of a device [117].

Although the issues presented here were not insurmountable, properly addressing them would require the production of new CMUT microarrays. The aforementioned results, in combination with time constraints, curtailed the exploration of these CMUT devices in phased array operation.

Chapter 5

Summary and outlook

Although particle manipulation using sound has been studied for the past 150 years, it is through a more recent integration with microfabrication that the repertoire of applications in acoustophoresis has exponentially grown. A recurring modality in acoustophoresis is the use of standing waves, the formation of which, has required the construction of acoustic resonator chambers. Transverse resonators in particular have typically been fabricated using wet etched and electrochemically bonded layers. These processes are impossible without caustic chemicals, expensive equipment, and cleanroom facilities.

Throughout this period of research, an aspect that has remained fundamentally unchanged is the use of piezoelectric transducers as a sound source. There is much to appreciate about the venerable piezoelectric transducer; it is relatively easy to produce, ubiquitous, and its principles of operation well understood. Conversely, capacitive micromachined ultrasound transducers (CMUTs) are the industry upstarts; touting advantages of wider bandwidth, microfabrication process compatibility, better impedance matching to fluids, and higher temperature stability. CMUTs have begun to be seen as a viable, even preferential, option for certain ultrasound imaging applications; however, their use in acoustophoresis has barely been investigated.

5.1 Simplified resonators

This thesis first looked to develop a simple and equipment-free method for fabricating transverse acoustic resonators for use with off-the-shelf piezoelectric transducers. The proposed method was a layered design that sandwiched glass microscope slides between polyimide

tape. The critical dimension of spacing between transducer walls was accomplished, with acceptable repeatability, using simple removable shims. Utilizing this method we have demonstrated bifurcating and trifurcating microchannel resonators that are suitable for microscopy applications.

5.2 CMUTs and travelling wave acoustophoresis

A second avenue to be explored in this thesis was the use of CMUTs as a platform for acoustophoresis. Acoustic simulations were performed using COMSOL to understand the travelling wave pressure profile of a circular CMUT transducer cell. The simulations indicated that a point centered on the membrane surface of such a cell would act as a potential well. The strength of the well and corresponding acoustic gradient force suggested a CMUT cell was capable of trapping particles both vertically and laterally.

Experimental results confirmed the simulation findings. Using a solution of silica microparticles dispersed onto the CMUT surface as a droplet, individual CMUT cells were shown to act as local trapping sites creating clusters of beads. Utilizing the wide bandwidth of CMUTs we then demonstrated a heretofore unreported mode of acoustic manipulation, bead cluster expansion and contraction through a cycling frequency sweep operation. This palpating phenomenon was attributed to the gradient force intensifying as the membrane approached resonance and the subsequent relaxation of gradient forces as the resonance condition ended. The trapping force of the CMUT cell was found experimentally by introducing a laminar flow and equating the trapping force of the bead with the Stokes drag force due to fluid flow. The measured trapping force matched very well with the value obtained through the CMUT COMSOL model. The laminar flow was also used to sequentially trap beads from one CMUT cell to the next by timed activation and deactivation of the CMUT cell. It was additionally shown, by operating the CMUT microarray at threshold voltages, discrete streams of beads were formed in a laminar flow.

5.3 CMUTs and standing wave acoustophoresis

This investigation concluded by coupling the CMUT microarray to a microfluidic resonator in order to evaluate the platform for standing wave acoustophoresis. It was shown that the lateral acoustic gradient forces generated by array subsets were very weak, requiring many tens of minutes of operation to create particle agglomerates. These timescales are not ideal for microfluidic applications. Additionally, the effectiveness of activated array subsets was

variable across the device. This may be indicative of fabrication issues with the CMUT or perhaps the microchannel. Our FEM models show a strong asymmetric response to the standing wave when the microchannel depth deviates from the expected $\lambda/2$ depth. The thicknesses of Kapton tapes and films reported by the manufacturer are typical values. Choosing a more stringently controlled material could mitigate this issue. However, such materials would likely require the use of microfabrication tools and have to be performed during CMUT device fabrication rather than after.

5.4 Future work

The preliminary work of this thesis has shown that CMUT devices are promising candidates for the development of new acoustophoretic devices. While there are many possible research questions to pose, they fall broadly into one of two categories: fabrication or operation.

The CMUT devices described in this work were originally designed for imaging ultrasound research. While they were shoehorned into an acoustophoretic device, there are clear benefits to fabricating a CMUT for a specific application. For one thing, the CMUT device could be designed for eventual use with a microchannel. An issue that we encountered was finding the space to place the structures that would form the microchannel. For robust bonding and water tightness, the Kapton tape must be applied to a significant portion of the device surface. Consequently, many otherwise usable CMUT elements had to be sacrificed. A more ambitious plan would be to build part or all of the microchannel structure concurrent with the CMUT device fabrication. The benefits, especially considering a layered resonator design, is the precision of the same MEMS fabrication processes underpinning CMUT construction.

One advantage to the MEMS-based fabrication of CMUTs is that CMUT cells with multiple membrane sizes, and thus operating frequencies, can be constructed on a single device. With sufficient spatial and bandwidth separation between CMUTs, we can construct a resonator with various standing wave profiles at different points along a microchannel (see Figure 5.1a). Or, where travelling waves are used, CMUTs of different frequencies may interspersed, thus allowing the user to translate particles to regions of interest on the CMUT surface without using fluid flow (see Figure 5.1b).

Minimizing dielectric charging of the device is something else that can be addressed through fabrication. By choosing CMUT structural dimensions that minimize operational voltage the risk of dielectric charging is reduced. Another issue that can be addressed through fabrication is membrane layer uniformity. The thickness variation of SOI wafers,

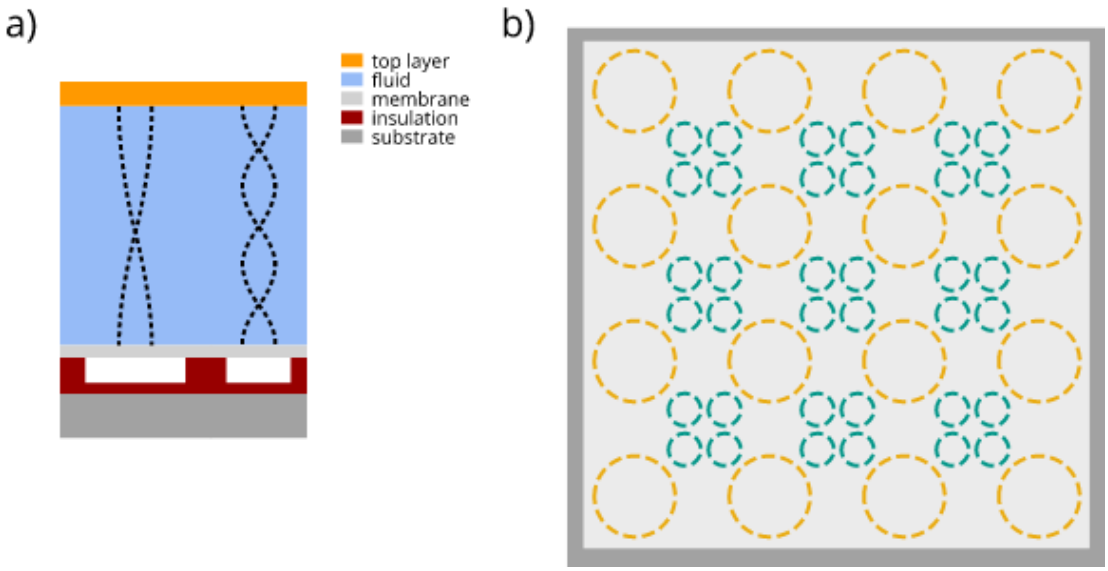

Figure 5.1: Possible future work displaying a) a cross section view of a microchannel that incorporates two sizes of CMUT membrane to generate standing waves of different modes and; b) the top-down view of a CMUT element featuring two sizes of interspersed cells that operate at two different frequencies

as used in our device, are generally considered to be high. This can manifest as membrane failures where the thickness is too low, or changes to the expected resonance frequency of the cell. By using higher quality wafers a membrane layer with higher thickness tolerances can be achieved. Variation in cavity depth between CMUT cells is another potential culprit for different cell-to-cell performance. For example, residual photoresist or contaminants that may not have been properly removed prior to bonding of the two wafers would result in reductions to effective cavity depth. Therefore, device performance would benefit from a more rigorous process control approach to fabricating the CMUT device.

An area that we did not explore in this thesis is the effect of transducer phase changes on particle manipulation. Were an opposing CMUT reflector device to be built, the nodal position of the standing wave formed between them could be moved by simply changing the relative phase of transducer excitation. Alternatively, a similar setup with opposing 2D-arrays could employ beam-forming to position the pressure focus at nearly any chosen location within the microchannel. A comparatively easier proposition is to use a single 2D array, like the one used in this work, to emulate a curved transducer and create focused ultrasound for acoustophoresis experiments. In previous years, designing the hardware to

enable phased-array operation of transducers was an onerous task. However, the recent purchase by this lab of a prototyping platform for driving transducer arrays should ease things considerably.

References

[1] I. -H. Chen. *Row-Column Capacitive Micromachined Ultrasonic Transducers for Medical Imaging*. PhD thesis, University of Waterloo, 2016.

[2] A. Kundt and O. Lehmann. Ueber longitudinale schwingungen und klangfiguren in cylindrischen flüssigkeitssäulen. *Annalen der Physik*, 229(9):1–12, 1874.

[3] L. V. King. On the acoustic radiation pressure on spheres. *Proc.R.Soc.London, Ser.A*, 147:212–240, 1934.

[4] K. Söllner and C. Bondy. The mechanism of coagulation by ultrasonic waves. *Transactions of the Faraday Society*, 32:616–623, 1936.

[5] Z. I. Mandralis and D. L. Feke. Fractionation of suspensions using synchronized ultrasonic and flow fields. *AIChE Journal*, 39(2):197–206, 1993.

[6] K. Yasuda, S. I Umemura, and K. Takeda. Concentration and fractionation of small particles in liquid by ultrasound. *Japanese Journal of Applied Physics*, 34(5S):2715–2720, 1995.

[7] D. W. Schindel, L. Zou, M. Sayer, and D. A. Hutchins. The design and characterization of micromachined air-coupled capacitance transducers. *IEEE Transactions on Ultrasonics, Ferroelectrics, and Frequency Control*, 42(1):42–50, 1995.

[8] Matthew I. Haller and Butrus T. Khuri-Yakub. Surface micromachined electrostatic ultrasonic air transducer. In *Proceedings of the IEEE Ultrasonics Symposium*, volume 2, pages 1241–1244, 1994.

[9] R. S. Molday, S. P. S. Yen, and A. Rembaum. Application of magnetic microspheres in labelling and separation of cells. *Nature*, 268(5619):437–438, 1977.

[10] S. A. Peyman, E. Y. Kwan, O. Margarson, A. Iles, and N. Pamme. Diamagnetic repulsiona versatile tool for label-free particle handling in microfluidic devices. *Journal of Chromatography A*, 1216(52):9055–9062, 2009.

[11] F. Shen, H. Hwang, Y. K. Hahn, and J. K Park. Label-free cell separation using a tunable magnetophoretic repulsion force. *Analytical Chemistry*, 84(7):3075–3081, 2012.

[12] H. A. Pohl. The motion and precipitation of suspensoids in divergent electric fields. *Journal of Applied Physics*, 22(7):869–871, 1951.

[13] H. Li and R. Bashir. Dielectrophoretic separation and manipulation of live and heat-treated cells of listeria on microfabricated devices with interdigitated electrodes. *Sensors and Actuators, B: Chemical*, 86(2):215–221, 2002.

[14] R. Pethig, Y. Huang, X. B. Wang, and J. P. H Burt. Positive and negative dielectrophoretic collection of colloidal particles using interdigitated castellated microelectrodes. *Journal of Physics D: Applied Physics*, 25(5):881–888, 1992.

[15] Y. Huang, R. Holzel, R. Pethig, and X. B. Wang. Differences in the ac electrodynamics of viable and non-viable yeast cells determined through combined dielectrophoresis and electrorotation studies. *Physics in Medicine and Biology*, 37(7):1499–1517, 1992.

[16] S. Sridharan, J. Zhu, G. Hu, and X. Xuan. Joule heating effects on electroosmotic flow in insulator-based dielectrophoresis. *Electrophoresis*, 32(17):2274–2281, 2011.

[17] Y. Kang, D. Li, S. A. Kalams, and J. E. Eid. Dc-dielectrophoretic separation of biological cells by size. *Biomedical Microdevices*, 10(2), 2008.

[18] A. Ashkin. Acceleration and trapping of particles by radiation pressure. *Physical Review Letters*, 24(4):156–159, 1970.

[19] A. Ashkin, J. M. Dziedzic, J. E. Bjorkholm, and S. Chu. Observation of a single-beam gradient force optical trap for dielectric particles. *Optics Letters*, 11(5):288–290, 1986.

[20] M. P. MacDonald, G. C. Spalding, and K. Dholakia. Microfluidic sorting in an optical lattice. *Nature*, 426(6965):421–424, 2003.

[21] H. Liang, K. T. Vu, P. Krishnan, T. C. Trang, D. Shin, S. Kimel, and M. W. Berns. Wavelength dependence of cell cloning efficiency after optical trapping. *Biophysical Journal*, 70(3):1529–1533, 1996.

[22] Y. Seol, A. E. Carpenter, and T. T. Perkins. Gold nanoparticles: Enhanced optical trapping and sensitivity coupled with significant heating. *Optics Letters*, 31(16):2429–2431, 2006.

[23] W. Soo Hoo, M. Wang, J. R. Kohrumel, and J. Hall. A novel method for detection of virus-infected cells through moving optical gradient fields using adenovirus as a model system. *Cytometry A*, 58(2):140–146, 2004.

[24] OPTOPHORESIS Trademark Information. https://www.trademarkia.com/optophoresis-76251726.html. Accessed: 2017-12-31.

[25] P. Debye. A method for the determination of the mass of electrolytic ions. *The Journal of chemical physics*, 1(1):13–16, 1933.

[26] J. F. Kelso and T. A. Ferrazzoli. Effect of powder surface chemistry on the stability of concentrated aqueous dispersions of alumina. *Journal of the American Ceramic Society*, 72(4):625–627, 1989.

[27] T. Allen. *Powder Sampling and Particle Size Determination*, chapter 10, pages 524–622. 2003.

[28] F. Petersson, A. Nilsson, C. Holm, H. Jönsson, and T. Laurell. Continuous separation of lipid particles from erythrocytes by means of laminar flow and acoustic standing wave forces. *Lab on a Chip - Miniaturisation for Chemistry and Biology*, 5(1):20–22, 2005.

[29] M. Evander, L. Johansson, T. Lilliehorn, J. Piskur, M. Lindvall, S. Johansson, M. Almqvist, T. Laurell, and J. Nilsson. Noninvasive acoustic cell trapping in a microfluidic perfusion system for online bioassays. *Analytical Chemistry*, 79(7):2984–2991, 2007.

[30] H. Bruus. Acoustofluidics 7: The acoustic radiation force on small particles. *Lab on a Chip - Miniaturisation for Chemistry and Biology*, 12(6):1014–1021, 2012.

[31] S. Kapishnikov, V. Kantsler, and V. Steinberg. Continuous particle size separation and size sorting using ultrasound in a microchannel. *Journal of Statistical Mechanics: Theory and Experiment*, (1), 2006.

[32] M. C. Jo and R. Guldiken. Active density-based separation using standing surface acoustic waves. *Sensors and Actuators, A: Physical*, 187:22–28, 2012.

[33] D. Ensminger. *Ultrasonics: Fundamentals, Technology, Application*. Marcel Dekker, Inc., 2nd edition, 1988.

[34] F. Chemat, Zill-E-Huma, and M. K. Khan. Applications of ultrasound in food technology: Processing, preservation and extraction. *Ultrasonics Sonochemistry*, 18(4):813–835, 2011.

[35] R. A. Nishimura, M. D. Abel, L.K. Hatle, and A. J. Tajik. Assessment of diastolic function of the heart: Background and current applications of doppler echocardiography. part ii. clinical studies. *Mayo Clinic Proceedings*, 64(2):181–204, 1989.

[36] C. M. C. Tempany, N. J. McDannold, K. Hynynen, and F. A. Jolesz. Focused ultrasound surgery in oncology: Overview and principles. *Radiology*, 259(1):39–56, 2011.

[37] B. Krumme. Renal doppler sonography- update in clinical nephrology. *Nephron-Clinical Practice*, 103(2):c24–c28, 2006.

[38] L. J. Salomon, Z. Alfirevic, V. Berghella, C. Bilardo, E. Hernandez-Andrade, S. L. Johnsen, K. Kalache, K. Y. Leung, G. Malinger, H. Munoz, F. Prefumo, A. Toi, and W. Lee. Practice guidelines for performance of the routine mid-trimester fetal ultrasound scan. *Ultrasound in Obstetrics and Gynecology*, 37(1):116–126, 2010.

[39] D. S. Bradshaw and D. L. Andrews. Manipulating particles with light: radiation and gradient forces. *European Journal of Physics*, 38(3):1–17, 2017. article no: 034008.

[40] L. P. Gor'kov. On the forces acting on a small particle in an acoustical field in an ideal fluid. *Sov.Phys.Dokl.*, 6(9):773–775, 1962.

[41] M. A. H. Weiser and R. E. Apfel. Interparticle forces on red cells in a standing wave field. *Acustica*, 56(2):114–119, 1984.

[42] P. Dayton, A. Klibanov, G. Brandenburger, and K. Ferrara. Acoustic radiation force in vivo: A mechanism to assist targeting of microbubbles. *Ultrasound in Medicine and Biology*, 25(8):1195–1201, 1999.

[43] M. Bengtsson and T. Laurell. Ultrasonic agitation in microchannels. *Analytical and Bioanalytical Chemistry*, 378(7):1716–1721, 2004.

[44] J. F. Spengler and W. T. Coakley. Microstreaming effects on particle concentration in an ultrasonic standing wave. *AIChE Journal*, 49(11):2773–2782, 2003.

[45] S. S. Sadhal. Acoustofluidics 13: Analysis of acoustic streaming by perturbation methods. *Lab on a Chip - Miniaturisation for Chemistry and Biology*, 12(13):2292–2300, 2012.

[46] M. Wiklund, R. Green, and M. Ohlin. Acoustofluidics 14: Applications of acoustic streaming in microfluidic devices. *Lab on a Chip - Miniaturisation for Chemistry and Biology*, 12(14):2438–2451, 2012.

[47] J. Wu and G. Du. Acoustic radiation force on a small compressible sphere in a focused beam. *Journal of the Acoustical Society of America*, 87(3):997–1003, 1990.

[48] J. Wu. Acoustical tweezers. *Journal of the Acoustical Society of America*, 89(5):2140–2143, 1991.

[49] J. Lee, S. Y. Teh, A. Lee, H. H. Kim, C. Lee, and K. K. Shung. Single beam acoustic trapping. *Applied Physics Letters*, 95:1–3, 2009. article no: 073701.

[50] J. Lee, C. Lee, H. H. Kim, A. Jakob, R. Lemor, S. Y. Teh, A. Lee, and K. K. Shung. Targeted cell immobilization by ultrasound microbeam. *Biotechnology and Bioengineering*, 108(7):1643–1650, 2011.

[51] Y. Qiu, H. Wang, C. E. M. Demore, D. A. Hughes, P. Glynne-Jones, S. Gebhardt, A. Bolhovitins, R. Poltarjonoks, K. Weijer, A. Schönecker, M. Hill, and S. Cochran. Acoustic devices for particle and cell manipulation and sensing. *Sensors*, 14:14806–14838, 2014.

[52] H. Bruus. Acoustofluidics 10: Scaling laws in acoustophoresis. *Lab on a Chip - Miniaturisation for Chemistry and Biology*, 12(9):1578–1586, 2012.

[53] M. Wiklund, S. Nilsson, and H. M. Hertz. Ultrasonic trapping in capillaries for trace-amount biomedical analysis. *Journal of Applied Physics*, 90(1):421–426, 2001.

[54] J. Curie and P. Curie. Développement par compression de l'électricité polaire dans les cristaux hémièdres à faces inclinées. *Bulletin de la Société minérologique de France*, 3:90–93, 1880.

[55] C. Chilowsky and P. Langevin. Production of submarine signals and the location of submarine objects. Patent, Oct 1923. US 1471547.

[56] D. R. Raichel. *The Science and Applications of Acoustics*, chapter 15, pages 409–441. 2006.

[57] I. M. Reaney, D. V. Taylor, and K. G. Brooks. Ferroelectric pzt thin films by sol-gel deposition. *Journal of Sol-Gel Science and Technology*, 13:813–820, 1998.

[58] A. Peschot, N. Bonifaci, O. Lesaint, C. Valadares, and C. Poulain. Deviations from Paschen's law at short gap distances from 100 nm to 10 μm in air and nitrogen. *Applied Physics Letters*, 105(12):1–4, 2014. article no: 123109.

[59] G. Gurun, P. Hasler, and F. L. Degertekin. Front-end receiver electronics for high-frequency monolithic cmut-on-cmos imaging arrays. *IEEE Transactions on Ultrasonics, Ferroelectrics, and Frequency Control*, 58(8):1658–1668, 2011.

[60] I. O. Wygant, N. S. Jamal, H. J. Lee, A. Nikoozadeh, Ö. Oralkan, M. Karaman, and B. T. Khuri-Yakub. An integrated circuit with transmit beamforming flip-chip bonded to a 2-d cmut array for 3-d ultrasound imaging. *IEEE Transactions on Ultrasonics, Ferroelectrics, and Frequency Control*, 56(10):2145–2156, 2009.

[61] J. Zahorian, M. Hochman, T. Xu, S. Satir, G. Gurun, M. Karaman, and F. L. Degertekin. Monolithic cmut-on-cmos integration for intravascular ultrasound applications. *IEEE transactions on ultrasonics, ferroelectrics, and frequency control*, 58(12):2659–2667, 2011.

[62] A. S. Ergun, G. G. Yaralioglu, and B. T. Khuri-Yakub. Capacitive micromachined ultrasonic transducers: Theory and technology. *Journal of Aerospace Engineering*, 16:76–84, 2003.

[63] J. J. Allen. *Micro Electro Mechanical System Design*, chapter 3, pages 101–102. 2005.

[64] I. O. Wygant, M. Kupnik, and B. T. Khuri-Yakub. Analytically calculating membrane displacement and the equivalent circuit model of a circular cmut cell. In *Proceedings of the IEEE Ultrasonics Symposium*, pages 2111–2114, 2008.

[65] B. T. Khuri-Yakub, K. K. Park, H.J. Lee, G. G. Yaralioglu, S. Ergun, Ö. Oralkan, M. Kupnik, C. F. Quate, T. Braun, H.P. Lang, M. Hegner, J. P. Ramseyer, C. Gerber, and J. Gimzewski. The capacitive micromachined ultrasonic transducer (cmut) as a chem/bio sensor. In *Proceedings of the IEEE Ultrasonics Symposium*, pages 472–475, 2007.

[66] Ö. Oralkan, A. S. Ergun, J. A. Johnson, M. Karaman, U. Demirci, K. Kaviani, T. H. Lee, and B. T. Khuri-Yakub. Capacitive micromachined ultrasonic transducers: Next-generation arrays for acoustic imaging? *IEEE Transactions on Ultrasonics, Ferroelectrics, and Frequency Control*, 49(11):1596–1610, 2002.

[67] A. Caronti, C. Longo, A. Savoia, P. Gatta, G. Caliano, and M. Pappalardo. Analysis of acoustic interaction effects and crosstalk in cmut linear arrays for medical imaging. In *Proceedings of the IEEE Ultrasonics Symposium*, volume 1, pages 582–585, 2006.

[68] S. Machida, S. Migitaka, H. Tanaka, K. Hashiba, H. Enomoto, Y. Tadaki, and T. Kobayashi. Analysis of the charging problem in capacitive micromachined ultrasonic transducers. In *Proceedings of the IEEE Ultrasonics Symposium*, pages 383–385, 2008.

[69] Y. Huang, A. S. Ergun, E. Hæggström, M. H. Badi, and B. T. Khuri-Yakub. Fabricating capacitive micromachined ultrasonic transducers with wafer-bonding technology. *Journal of Microelectromechanical Systems*, 12(2):128–137, 2003.

[70] J. K. Knight, J. McLean, and F. L. Degertekin. Low temperature fabrication of immersion capacitive micromachined ultrasonic transducers on silicon and dielectric substrates. *IEEE Transactions on Ultrasonics, Ferroelectrics, and Frequency Control*, 51(10):1324–1333, 2004.

[71] A. Nikoozadeh, Ö. Oralkan, M. Gencel, J. W. Choe, D. N. Stephens, A. de la Rama, P. Chen, K. Thomenius, A. Dentinger, D. Wildes, K. Shivkumar, A. Mahajan, M. O'Donnel, D. Sahn, and P. T. Khuri-Yakub. Forward-looking volumetric intracardiac imaging using a fully integrated cmut ring array. In *Proceedings of the IEEE International Ultrasonics Symposium*, 2009.

[72] J. Chen, X. Cheng, C. -C. Chen, P. -C. Li, J. -H. Liu, and Y. -T. Cheng. A capacitive micromachined ultrasonic transducer array for minimally invasive medical diagnosis. *Journal of Microelectromechanical Systems*, 17(3):599–610, 2008.

[73] A. Nilsson, F. Petersson, H. Jönsson, and T. Laurell. Acoustic control of suspended particles in micro fluidic chips. *Lab on a Chip - Miniaturisation for Chemistry and Biology*, 4(2):131–135, 2004.

[74] J. Shi, X. Mao, D. Ahmed, A. Colletti, and T. J. Huang. Focusing microparticles in a microfluidic channel via standing surface acoustic waves (ssaw). *Lab on a Chip - Miniaturisation for Chemistry and Biology*, 8(2):221–223, 2008.

[75] O. Manneberg, J. Svennebring, H. M. Hertz, and M. Wiklund. Wedge transducer design for two-dimensional ultrasonic manipulation in a microfluidic chip. *Journal of Micromechanics and Microengineering*, 18(9), 2008. Cited By :27.

[76] J. J. Hawkes, M. Gröschl, E. Benes, H. Nowotny, and W. T. Coakley. *Positioning Particles Within Liquids Using Ultrasound Force Fields*, 2002.

[77] F. Guo, Z. Mao., Y. Chen, Z. Xie, J. P. Lata, P. Li, L. Ren, J. Liu, J. Yang, M. Dao, S. Suresh, and T. J. Huang. Three-dimensional manipulation of single cells using surface acoustic waves. *PNAS*, 113(6):1522–1527, 2016.

[78] O. Manneberg, S. Melker Hagsäter, J. Svennebring, H. M. Hertz, J. P. Kutter, H. Bruus, and M. Wiklund. Spatial confinement of ultrasonic force fields in microfluidic channels. *Ultrasonics*, 49(1):112–119, 2009.

[79] M. Evander, A. Lenshof, T. Laurell, and J. Nilsson. Acoustophoresis in wet-etched glass chips. *Analytical Chemistry*, 80(13):5178–5185, 2008.

[80] G. Goddard and G. Kaduchak. Ultrasonic particle concentration in a line-driven cylindrical tube. *Journal of the Acoustical Society of America*, 117(6):3440–3447, 2005.

[81] B. Hammarström, M. Evander, H. Barbeau, M. Bruzelius, J. Larsson, T. Laurell, and J. Nilsson. Non-contact acoustic cell trapping in disposable glass capillaries. *Lab on a Chip - Miniaturisation for Chemistry and Biology*, 10(17):2251–2257, 2010.

[82] P. Glynne-Jones, C. E. M. Démoré, C. Ye, Y. Qiu, S. Cochran, and M. Hill. Array-controlled ultrasonic manipulation of particles in planar acoustic resonator. *IEEE Transactions on Ultrasonics, Ferroelectrics, and Frequency Control*, 59(6):1258–1266, 2012.

[83] J. J. Hawkes and W. Terence Coakley. Force field particle filter, combining ultrasound standing waves and laminar flow. *Sensors and Actuators, B: Chemical*, 75(3):213–222, 2001.

[84] M. Hill. The selection of layer thicknesses to control acoustic radiation force profiles in layered resonators. *Journal of the Acoustical Society of America*, 114(5):2654–2661, 2003.

[85] A. R. Rezk, J. R. Friend, and L. Y. Yeo. Simple, low cost mhz-order acoustomicrofluidics using aluminium foil electrodes. *Lab on a Chip - Miniaturisation for Chemistry and Biology*, 14(11):1802–1805, 2014.

[86] T. Laurell, F. Petersson, and A. Nilsson. Chip integrated strategies for acoustic separation and manipulation of cells and particles. *Chemical Society Reviews*, 36(3):492–506, 2007.

[87] F. Petersson, L. Åberg, A. M Swärd-Nilsson, and T. Laurell. Free flow acoustophoresis: Microfluidic-based mode of particle and cell separation. *Analytical Chemistry*, 79(14):5117–5123, 2007.

[88] S. Queste, R. Salut, S. Clatot, J. Y Rauch, and C. G. Khan Malek. Manufacture of microfluidic glass chips by deep plasma etching, femtosecond laser ablation, and anodic bonding. *Microsystem Technologies*, 16(8-9):1485–1493, 2010.

[89] R. E. Hayes, K. Nandakumar, and H. Nasr-El-Din. Steady laminar flow in a 90 degree planar branch. *Computers and Fluids*, 17(4):537–553, 1989.

[90] S. M. Hagsäter, A. Lenshof, P. Skafte-Pedersen, J. P. Kutter, T. Laurell, and H. Bruus. Acoustic resonances in straight micro channels: Beyond the 1d-approximation. *Lab on a Chip - Miniaturisation for Chemistry and Biology*, 8(7):1178–1184, 2008.

[91] O. Manneberg, B. Vanherberghen, B. Önfelt, and M. Wiklund. Flow-free transport of cells in microchannels by frequency-modulated ultrasound. *Lab on a Chip - Miniaturisation for Chemistry and Biology*, 9(6):833–837, 2009.

[92] C. R. P. Courtney, C. K. Ong, B. W. Drinkwater, P. D. Wilcox, C. Demore, S. Cochran, P. Glynne-Jones, and M. Hill. Manipulation of microparticles using phase-controllable ultrasonic standing waves. *Journal of the Acoustical Society of America*, 128(4):EL195–EL199, 2010.

[93] Z. Li, L. L. P. Wong, S. Na, J. Sun, and J. T. W. Yeow. Fabrication of capacitive micromachined ultrasonic transducers based on adhesive wafer bonding technique. *Journal of Micromechanics and Microengineering*, 26(11), 2016. article no: 115019.

[94] H. M. Hertz. Standing-wave acoustic trap for nonintrusive positioning of microparticles. *Journal of Applied Physics*, 78(8):4845–4849, 1995.

[95] D. Baresch, J. L. Thomas, and R. Marchiano. Observation of a single-beam gradient force acoustical trap for elastic particles: Acoustical tweezers. *Physical Review Letters*, 116(2):024301–1–024301–6, 2016.

[96] C. E. M. Démoré, P. M. Dahl, Z. Yang, P. Glynne-Jones, A. Melzer, S. Cochran, M. P. MacDonald, and G. C. Spalding. Acoustic tractor beam. *Physical Review Letters*, 112(17):174302–1–174302–5, 2014.

[97] Y. Ochiai, T. Hoshi, and J. Rekimoto. Three-dimensional mid-air acoustic manipulation by ultrasonic phased arrays. *PLoS ONE*, 9(5), 2014. article e97590.

[98] C. R. P. Courtney, B. W. Drinkwater, C.E.M. Demore, S. Cochran, A. Grinenko, , and P. D. Wilcox. Dexterous manipulation of microparticles using bessel-function acoustic pressure fields. *Applied Physics Letters*, 102(12):1–5, 2013. article no: 123508.

[99] J. McLean and F. L. Degertekin. Directional scholte wave generation and detection using interdigital capacitive micromachined ultrasonic transducers. *IEEE Transactions on Ultrasonics, Ferroelectrics, and Frequency Control*, 51(6):756–764, 2004.

[100] M. Thränhardt, P. C. Eccardt, H. Mooshofer, P. Hauptmann, and L. Degertekin. Sensing physical fluid properties with cmut arrays. In *Proceedings of the IEEE Ultrasonics Symposium*, pages 763–766, 2009.

[101] D. Pelenis, D. Barauskas, E. Sapeliauskas, G. Vanagas, M. Mikolajunas, and D. Virzonis. Acoustical streaming in microfluidic cmut integrated chip controls the biochemical interaction rate. *Journal of Microelectromechanical Systems*, 26(5):1012–1017, 2017.

[102] F. Y. Yamaner, X. Zhang, and Ö. Oralkan. A three-mask process for fabricating vacuum-sealed capacitive micromachined ultrasonic transducers using anodic bonding. *IEEE Transactions on Ultrasonics, Ferroelectrics, and Frequency Control*, 62(5):972–982, 2015.

[103] A. Zeshan, X. Zhang, Ö. Oralkan, and F. Y. Yamaner. 2d cmut array based ultrasonic micromanipulation platform. In *Proceedings of the IEEE Ultrasonics Symposium*, 2016.

[104] S. P. Mao, K. Zhong, V. Rochus, S. Severi, B. Nauwelaers, H. A. C. Tilmans, and X. Rottenberg. Capacitive micromachined ultrasonic transducers for acoustic manipulation. In *International Conference on Solid-State Sensors, Actuators, and Microsystems*, pages 662–665, 2015.

[105] I. Leibacher, S. Schatzer, and J. Dual. Impedance matched channel walls in acoustofluidic systems. *Lab on a Chip - Miniaturisation for Chemistry and Biology*, 14(3):463–470, 2014.

[106] C. E. Morton and G. R. Lockwood. Theoretical assessment of a crossed electrode 2-d array for 3-d imaging. In *Proceedings of the IEEE Ultrasonics Symposium*, volume 1, pages 968–971, 2004.

[107] G. Vanagas, D. Barauskas, and D. Virzonis. Study of cmut operation in microchannel application. In *Proceedings of the IEEE Ultrasonics Symposium*, pages 1814–1817, 2012.

[108] R. J. McGough, T. V. Samulski, and J. F. Kelly. An efficient grid sectoring method for calculations of the near-field pressure generated by a circular piston. *Journal of the Acoustical Society of America*, 115(5):1942–1954, 2004.

[109] K. K. Park, M. Kupnik, H.J. Lee, B. T. Khuri-Yakub, and I. O. Wygant. Modeling and measuring the effects of mutual impedance on multi-cell cmut configurations. In *Proceedings of the IEEE Ultrasonics Symposium*, pages 431–434, 2010.

[110] K. C. Neuman and A. Nagy. Single-molecule force spectroscopy: optical tweezers, magnetic tweezers and atomic force microscopy. *Nature Methods*, 5(6):491–505, 2008.

[111] J. Nilsson, M. Evander, B. Hammarström, and T. Laurell. Review of cell and particle trapping in microfluidic systems. *Analytica Chimica Acta*, 649(2):141–157, 2009.

[112] Y. Qiu, H. Wang, S. Gebhardt, A. Bolhovitins, C. E. M. Démoré, A. Schönecker, and S. Cochran. Screen-printed ultrasonic 2-d matrix array transducers for microparticle manipulation. *Ultrasonics*, 62:136–146, 2015.

[113] D. A. A. Vignali. Multiplexed particle-based flow cytometric assays. *Journal of Immunological Methods*, 243(1-2):243–255, 2000.

[114] D. M. Rissin, D. R. Fournier, T. Piech, C. W. Kan, T. G. Campbell, L. Song, L. Chang, A. J. Rivnak, P. P. Patel, G. K. Provuncher, E. P. Ferrell, S. C. Howes, B. A. Pink, K. A. Minnehan, D. H. Wilson, and D. C. Duffy. Simultaneous detection of single molecules and singulated ensembles of molecules enables immunoassays with broad dynamic range. *Analytical Chemistry*, 83(6):2279–2285, 2011.

[115] C. T. Lim and Y. Zhang. Bead-based microfluidic immunoassays: The next generation. *Biosensors and Bioelectronics*, 22(7):1197–1204, 2007.

[116] P. E. Sheehan and L. J. Whitman. Detection limits for nanoscale biosensors. *Nano Letters*, 5(4):803–807, 2005.

[117] J. Lei, P. Glynne-Jones, and M. Hill. Acoustic streaming in the transducer plane in ultrasonic particle manipulation devices. *Lab on a Chip - Miniaturisation for Chemistry and Biology*, 13(11):2133–2143, 2013.

APPENDICES

Appendix A

Video of CMUT device operating in travelling wave on a droplet of bead solution

This appendix is a video file wherein a droplet of initially dispersed 4 μm silica beads in solution agglomerate into discrete clusters over the cells of a CMUT element after the element is activated. The CMUT device is operating at a single frequency of 2.9 MHz. The video is presented at 2$\times$ actual speed.

The file name of this video file is "SV1.mp4"

If you accessed this thesis from a source other than the University of Waterloo, you may not have access to this file. You may access it by searching for this thesis on https://uwspace.uwaterloo.ca/UWSpace.

Appendix B

Video of palpating bead cluster in travelling wave, droplet mode, operation of CMUT

This appendix is a video file wherein agglomerated clusters of 4 μm silica beads undergo expansion and contraction when a CMUT element is operated at a linear frequency sweep from 1 to 3.1 MHz at a period of 15 s. The video is presented at 2$\times$ actual speed.

The file name of this video file is "SV2.mp4"

If you accessed this thesis from a source other than the University of Waterloo, you may not have access to this file. You may access it by searching for this thesis on https://uwspace.uwaterloo.ca/UWSpace.

Appendix C

Video of sequential bead trapping in travelling wave, flow mode operation of CMUT

This appendix is a video file wherein clusters of 4 μm silica beads are trapped against flow at CMUT cells and then allowed to re-enter the flow before being trapped by downstream CMUT cells. When operating, the CMUT element is running at a linear frequency sweep from 2.9 to 3.1 MHz at a period of 10 ms. The video is presented at actual speed.

The file name of this video file is "SV4.mp4"

Appendix D

Video of palpating bead cluster in travelling wave, flow mode, operation of CMUT

This appendix is a video file wherein clusters of 4 μm silica beads are trapped against a flow of 5 μl·min^{-1} and undergo expansion and contraction when a CMUT element is operated at a linear frequency sweep from 1 to 3.1 MHz at a period of 100 ms. The video is presented at actual speed.

The file name of this video file is "SV3.mp4"

If you accessed this thesis from a source other than the University of Waterloo, you may not have access to this file. You may access it by searching for this thesis on https://uwspace.uwaterloo.ca/UWSpace.

Appendix E

Video of bead separation into discrete lines in travelling wave, flow mode, operation of CMUT

This appendix is a video file wherein clusters of 4 μm silica beads are separated into discrete streams of beads by operating the array at low (1 to 5 V_{p-p}) threshold AC voltages. The video is presented at actual speed.

The file name of this video file is "SV5.mp4"

If you accessed this thesis from a source other than the University of Waterloo, you may not have access to this file. You may access it by searching for this thesis on https://uwspace.uwaterloo.ca/UWSpace.

Appendix F

Video of bead aggregate rotation in standing wave operation of 2×2 corners in a 6×6 CMUT array

This appendix is a video file wherein clusters of 10 μm fluorescent beads are briefly trapped and rotate, evidence of an unstable microflow occurring in the channel. The video is presented at actual speed.

The file name of this video file is "SV6.mp4"

If you accessed this thesis from a source other than the University of Waterloo, you may not have access to this file. You may access it by searching for this thesis on https://uwspace.uwaterloo.ca/UWSpace.

Appendix G

Volumetric to linear flow rate conversion

To convert from a volumetric to linear flow rate we first convert μl·min^{-1} to units of mm^3·sec^{-1}. Then we calculate the cross-sectional area through which the fluid is flowing. The microchannels created for travelling wave experiments are 2 mm wide and 0.2 mm deep, yielding an area of 0.4 mm^2. Dividing the mm^3·sec^{-1} by the cross-sectional area will provide the linear flow rate.

In a microchannel the flow of a fluid will be slowest at the microchannel surfaces and fastest in the center. This results in a parabolic flow profile and must also be considered in the conversion. Using the equation for parabolic flow,

$$v(r) = 2V_{avg}(1 - \frac{r^2}{R^2}) \tag{G.1}$$

where V_{avg} is the average linear velocity of the flow (the flow rate reported by the pump), r is the distance from the center of the channel to the point of interest, and R is the distance from the center of the channel to the channel surface. Here we must make an assumption as to the value of r. We know that when the CMUT is activated beads are trapped close to the surface and when deactivated the previously trapped beads move laterally $\leq 10\mu$m. Therefore, an r value of 180 μm was chosen.

Appendix H

FOCUS code for acoustic pressure model of CMUT array

To calculate the pressure fields created by our CMUT array the FOCUS program running in a MATLAB environment was used. Included below is the code used to generate the graphs in Figure 4.15b. The FOCUS code was modified from versions provided to the author by Zhou Zheng and Ibrahim Bendaya.

```
% MAIN PROGRAM

close all
clear all
clc
fprintf('[Circular_CMUT.m]\n');
fprintf('Circular membrane')

tic

% Define a planar array with circular CMUT cells
el_x = 7;            % number of elements in x-direction of the array
el_y = 7;            % number of elements in y-direction of the array
radius = 30e-6;      % membrane radius [m]
kerf_x = -10e-6;     % x-distance from edge of one cell to next [m]
kerf_y = -10e-6;     % y-distance from edge of one cell to next [m]
f0 = 3.0e6;          % Operating frequency [Hz]
```

```
xdcr = create_circ_planar_array(el_x, el_y, radius, kerf_x, kerf_y);

% Specify which cells in the planar array are active (0 = off, 1 = on)
enabled = [1 0 1 0 1 0 1
           0 1 0 1 0 1 0
           1 0 1 0 1 0 1
           0 1 0 1 0 1 0
           1 0 1 0 1 0 1
           0 1 0 1 0 1 0
           1 0 1 0 1 0 1];
xdcr = enable_ele(xdcr,enabled);

% Create the data structure that specifies the attenuation value, etc.
medium = set_medium('water');

% Define the computational AOI
xmin = -el_x*(radius);
xmax = el_x*(radius);
ymin = 0;
ymax = 0;
zmin = 0;
zmax = 250e-6;

nx = 200;
ny = 200;
nz = 500;

dx = (xmax - xmin) / nx;
dz = (zmax - zmin) / nz;
x = xmin:dx:xmax;
z = zmin:dz:zmax;

ndiv = 50;

cg = set_coordinate_grid([dx 0 dz], xmin, xmax, ymin, ymax, zmin, zmax);

% Generate the pressure field
```

```
pressure = cw_pressure(xdcr, cg, medium, ndiv, f0);
abs_pressure = squeeze(abs(pressure));
Max_pressure = max(max(abs_pressure));
[mx mz] =find(squeeze(abs(pressure))==Max_pressure);
disp(['The maximum pressure is ', num2str(Max_pressure/1e6),' MPa']);
MaxPressure_location = [x(mx) z(mz)]*1e3     % mm

toc

% show -6dB profile
pref1 = abs(squeeze(pressure));
pref_dB=20*log10(pref1);
pref_dB=pref_dB-max(max(pref_dB));
pref_dB(pref_dB<-6)=0;
contour(x*1000, z*1000, pref_dB');
title('-6dB beam profile');
xlabel('x (mm)');
ylabel('z (mm)');


% Show transducer (verification purposes only)
figure();
draw_array(xdcr);
xlabel('x (m)');
ylabel('y (m)');
zlabel('z (m)');

% Show beam profile (verification purposes only)
figure();
pcolor(x*1000, z*1000, abs_pressure');
shading flat;
title('Pressure at y = 0');
xlabel('x (mm)');
ylabel('z (mm)');

% Write (absolute) pressure data to an Excel file
xlswrite('C:\Users\Champika\Documents\FOCUSscripts\single_element_3MHz.xlsx',
abs_pressure',3);
```

```
% KEY CALLED FUNCTIONS:

function xdcr_array=create_circ_planar_array(nelex,neley,radius,kerf_x,kerf_y,center,
override)
% Description
%     This function creates a planar array of circular transducers.
% Usage
%     transducer = create_circ_planar_array();
%     transducer = create_circ_planar_array(nx, ny, radius, kerf_x, kerf_y);
%     transducer = create_circ_planar_array(nx, ny, radius, kerf_x, kerf_y, center);
%     transducer = create_circ_planar_array(nx, ny, radius, kerf_x, kerf_y, center,
%     textbackslashoverride);
% Arguments
%     nx: Number of elements in the x direction.
%     ny: Number of elements in the y direction.
%     radius: Radius each element in m. All elements in the array will be the same
%     size.
%     kerf_x: Kerf (edge-to-edge spacing) in the x direction.
%     kerf_y: Kerf (edge-to-edge spacing) in the y direction.
%     center: Three element array that is the coordinate of the center of the array.
%     This argument is optional.
%     override: Omit to allow error checking, any value to bypass error checking.
% Output Parameters
%     transducer: An array of transducer structs.
% Notes
%     The center of the array is defined to be the geometric center of the rectangle
%     that bounds the array. All coordinates are expressed in meters.
if nargin==0
disp('Please enter the following arguments:')
disp('nelex, neley, radius, x kerf, y kerf, center(a 3x1 array)')
nelex=input('nelex:');
neley=input('neley:');
radius=input('radius:');
if nelex~=1
        kerf_x=input('x kerf:');
    else
        kerf_x=radius*0.1;
```

```
    end
    if neley~=1
        kerf_y=input('y kerf:');
    else
        kerf_y = radius*0.1;
    end
    center=[0 0 0 ];
end
% The following if statement is commented out to allow cell overlap, we have
% a tightly packed cell layout and the unphysical, overlapping cells are
% manually disengaged in the "enabled" matrix of the main program.
%
% if (kerf_x < 0 || kerf_y < 0)&& nargin()~=7 && (nelex~=1 &&neley ~=1)
%     xdcr_array=[];
%  disp('Elements are going to overlap')
%  disp('array not created, if you really')
%  disp('want to make the array, please set')
%  error('the override flag using arguments')
%  return
% end

if nargin()==5
    center=[0 0 0];
end
if length(center)~=3
    center=[ 0 0 0];
end

if mod(nelex,2)==1
    xf=0;
else
    xf=.5;
end
if mod(neley,2)==1
    yf=0;
else
    yf=.5;
end
```

```
spacing_x = kerf_x + (2*radius);
spacing_y = kerf_y + (2*radius);

x_coords = floor(-(nelex-1)/2):floor((nelex-1)/2);
y_coords = floor(-(neley-1)/2):floor((neley-1)/2);

for i=1:nelex
    for j=1:neley
        x = x_coords(i)*spacing_x+xf*spacing_x+center(1);
        y = y_coords(j)*spacing_y+yf*spacing_y+center(2);
        z = center(3);

        xdcr_array(i,j)=get_circ(radius,[x y z],[0 0 0]);
    end
end
%draw_array(xdcr_array,'r');

function xdcr_array_enable = enable_ele(xdcr_array,enabled)
% Description
%   Assigns which elements in an array are active or inactive
count = 1;
% new_struct=[];
for i = 1:size(xdcr_array,1)
    for j = 1:size(xdcr_array,2)
        if enabled(i,j)
            new_stru(count) = xdcr_array(i,j);
            count = count+1;
        end
    end
end

xdcr_array_enable = new_stru;

end

function medium=set_medium(varargin)
% Description
```

```
%   Create a medium struct for use with other FOCUS functions.
% Usage
%   medium = set_medium();
%   medium = set_medium(cb, wb, rho, c_sound, b, atten_coeff, ct, kappa, beta);
% Arguments
%   cb: Specific heat of blood in J/kg/K
%   wb: Blood perfusion in kg/meter3/s
%   rho: The density of the medium in kg/meter3
%   c_sound: The speed of sound in m/s
%   b: Power law exponent; unitless.
%   atten_coeff: Attenuation coefficient in dB/cm/MHz
%   ct: Specific heat of the medium in J/kg/K
%   kappa: Thermal conductivity in W/m/K
%   beta: Nonlinear parameter; unitless.
% Output Parameters
%   medium: A MATLAB struct with the following properties:
% Notes
%   If no arguments are specified, the function will prompt the user to enter the
%   correct values.
if nargin()==0
disp('Please enter the medium variables:')
    disp('If you don''t know what these parameters mean, please use one of the media
    defined by define_media.')
wb=input('Blood perfusion (kg/m^3/s): ');
rho=input('Density (kg/m^3): ');
c_sound=input('Speed of sound (m/s): ');
b=input('Power Law exponent (unitless): ');
    atten_coeff=input('Attenuation (dB/cm/MHz): ');
    ct=input('Specific heat (J/kg/K): ');
    kappa=input('Thermal conductivity (W/m/K): ');
    beta=input('Nonlinearity parameter (unitless): ');
medium=set_medium(3480,wb,rho,c_sound,b,atten_coeff,ct,kappa,beta);
return
% 1 argument: string representing medium type, e.g. 'lossless'
elseif nargin()==1
    if strcmp(varargin{1}, 'lossless')
        medium = set_medium(3.48e3, 0, 1.000e3, 1.500e3, 1, 0, 4.180e3, 6.150e-1, 0);
    elseif strcmp(varargin{1}, 'attenuated')
```

```
        medium = set_medium(3.48e3, 0, 1.000e3, 1.500e3, 1, 1, 4.180e3, 6.150e-1, 0);
    elseif strcmp(varargin{1}, 'water')
        medium = set_medium(3.48e3, 0, 1.000e3, 1.500e3, 1, 2.5e-4, 4.180e3,
        6.150e-1, 0);
    elseif strcmp(varargin{1}, 'skin')
        medium = set_medium(3.48e3, 5, 1.200e3, 1.498e3, 1, 1.4e-1, 3.430e3,
        2.660e-1, 0);
    elseif strcmp(varargin{1}, 'fat')
        medium = set_medium(3.48e3, 5, 9.210e2, 1.445e3, 1, 7.0e-2, 2.325e3,
        2.230e-1, 0);
    elseif strcmp(varargin{1}, 'muscle')
        medium = set_medium(3.48e3, 5, 1.138e3, 1.569e3, 1, 8.0e-2, 3.720e3,
        4.975e-1, 0);
    elseif strcmp(varargin{1}, 'liver')
        medium = set_medium(3.48e3, 5, 1.060e3, 1.540e3, 1, 3.2e-2, 3.600e3,
        5.120e-1, 0);
    elseif strcmp(varargin{1},'nonlinearlossless')
        medium = set_medium(3.48e3, 0, 1.000e3, 1.500e3, 1, 0, 4.180e3, 6.150e-1, 1);
    elseif strcmp(varargin{1},'nonlinearlossy')
        medium = set_medium(3.48e3, 0, 1.000e3, 1.500e3, 1, 1e-2, 4.180e3, 6.150e-1,
        1);
    else
        error('FOCUS:InvalidMediumType','Invalid medium type. See the documentation
        for a list of accepted types.');
    end
    return
% 9 arguments: all properties defined
elseif nargin()==9
    medium.specificheatofblood=varargin{1};
    medium.bloodperfusion=varargin{2};
    medium.density=varargin{3};
    medium.soundspeed=varargin{4};
    medium.powerlawexponent=varargin{5};
    % Decide which attenuation to set based on the power law exponent
    if medium.powerlawexponent == 1
        medium.attenuationdBcmMHz=varargin{6};
    else
        medium.attenuationdBcmMHzy=varargin{6};
```

```
    end
    medium.specificheat=varargin{7};
    medium.thermalconductivity=varargin{8};
    medium.nonlinearityparameter=varargin{9};
    return
% Number of arguments not a multiple of 2; arguments are not preceded by their names
elseif ~mod(nargin(),2)
    arg_count = nargin();
    % Assign default values for all properties
    medium.specificheatofblood = 3.48e3;
    medium.bloodperfusion = 0;
    medium.density = 1000;
    medium.soundspeed = 1500;
    medium.powerlawexponent = 1;
    medium.specificheat = 4.18e3;
    medium.thermalconductivity = 6.15e-1;
    medium.nonlinearityparameter = 0;
    % Assign any arguments that are present
    for i=1:2:arg_count
        arg_label = varargin{i};
        arg_value = varargin{i+1};
        if ~(isa(arg_label, 'char') && isa(arg_value, 'numeric'))
            error('FOCUS:InvalidArguments','Invalid arguments provided. Please see
            the documentation for information on how to use this function.');
            return
        end
        if strcmp(arg_label, 'specificheatofblood')
            medium.specificheatofblood = arg_value;
        elseif strcmp(arg_label, 'bloodperfusion')
            medium.bloodperfusion = arg_value;
        elseif strcmp(arg_label, 'density')
            medium.density = arg_value;
        elseif strcmp(arg_label, 'soundspeed')
            medium.soundspeed = arg_value;
        elseif strcmp(arg_label, 'powerlawexponent')
            medium.powerlawexponent = arg_value;
        elseif strcmp(arg_label, 'attenuationdBcmMHz')
            medium.attenuationdBcmMHz = arg_value;
```

```
        elseif strcmp(arg_label, 'attenuationdBcmMHzy')
            medium.attenuationdBcmMHzy = arg_value;
        elseif strcmp(arg_label, 'specificheat')
            medium.specificheat = arg_value;
        elseif strcmp(arg_label, 'thermalconductivity')
            medium.thermalconductivity = arg_value;
        elseif strcmp(arg_label, 'nonlinearityparameter')
            medium.nonlinearityparameter = arg_value;
        end
    end
    % Check that the medium is sane
    % Power law attenuation but y = 1 -- won't cause wrong results so just a warning
    if isfield(medium, 'attenuationdBcmMHzy') && medium.powerlawexponent == 1
        warning('Power law attenuation has been specified but the power law exponent
        is 1. ''attenuationdBcmMHz'' can be used for non-power law media.');
    % Non-power law attenuation but y != 1 -- error
    elseif isfield(medium, 'attenuationdBcmMHz') && medium.powerlawexponent ~= 1
        error('Power law exponent is not 1 but a non-power law attenuation has been
        specified. You must use ''attenuationdBcmMHzy'' to set attenuation for power
        law media.');
    end
    % Both attenuations set -- error
    if isfield(medium, 'attenuationdBcmMHz') && isfield(medium,
    'attenuationdBcmMHzy')
        error('Both power law and non-power law attenuation values are set. Only one
        of these variables may be set for the simulation to work correctly.');
    end
    % Set default attenuation based on power law exponent
    if ~isfield(medium, 'attenuationdBcmMHz') && ~isfield(medium,
    'attenuationdBcmMHzy')
        if medium.powerlawexponent == 1
            medium.attenuationdBcmMHz = 0;
        else
            medium.attenuationdBcmMHzy = 0;
        end
    end
    return
else
```

```
    error('FOCUS:InvalidArguments','Invalid number of arguments provided. See the
    documentation for information about the arguments.');
end

function pressure = cw_pressure(varargin)
%Description
%   Calculate continuous-wave pressures with the Fast Nearfield Method in FOCUS
% Usage
%   pressure = cw_pressure(transducer, cg, medium, ndiv, f0);
%   pressure = cw_pressure(transducer, cg, medium, ndiv, f0, method);
% Arguments
%   transducer: A FOCUS transducer array.
%   cg: A FOCUS coordinate grid.
%   medium: A FOCUS medium.
%   ndiv: The number of integral points to use.
%   f0: Frequency of the array in Hz.
%   method: The method to use when calculating the pressure. If the string 'sse' is
%   present, SSE instructions will be used to speed up the calculation where
%   possible.
%   Valid pressure calculation methods are:
%       'fnm': Use the Fast Nearfield Method (fnm_cw), this is the default.
%       'farfield': Use the farfield approximation (farfield_cw).
%       'rayleigh': Use the Rayleigh-Sommerfeld Integral (rayleigh_cw).
% Output Parameters
%   pressure: A 3-d array representing the complex pressure at each point in space.
if nargin < 5 || nargin > 6
    error('Incorrect number of arguments for cw_pressure. Please see the
    documentation for details on how to use this function.');
end

xdcr_array = varargin{1};
coord_grid = varargin{2};
medium = varargin{3};
ndiv = varargin{4};
f0 = varargin{5};

if nargin < 6
    method = 'fnm';
```

```
else
    method = varargin{6};
end

if strfind(method,'fnm')
    if strfind(method, 'sse')
        % Round ndiv up to the nearest multiple of 4
        ndiv = ceil(ndiv/4)*4;
        pressure = fnm_cw_sse(xdcr_array, coord_grid, medium, ndiv, f0, 0);
    else
        pressure = fnm_call(xdcr_array, coord_grid, medium, ndiv, f0, 0);
    end
elseif strfind(method, 'farfield')
    pressure = farfield_cw(xdcr_array, coord_grid, medium, ndiv, f0, 0);
elseif strfind(method, 'rayleigh')
    if strfind(method, 'sse')
        % Round ndiv up to the nearest multiple of 4
        ndiv = ceil(ndiv/4)*4;
        pressure = rayleigh_cw_sse(xdcr_array, coord_grid, medium, ndiv, f0, 0);
    else
        pressure = rayleigh_cw(xdcr_array, coord_grid, medium, ndiv, f0, 0);
    end
else
    error('Unsupported calculation method. See the documentation for cw_pressure for
    valid values.');
end
end

function Pressure=fnm_call(xdcr,cg,medium,ndiv,f0,dflag,nthreads)
% Description
%   This function is the gateway between the Matlab and C++ binary. It does minimal
%   error checking to ensure enough arguments are being passed.
% Usage
%   pressure = fnm_call(transducer, cg, medium, ndiv, f0, dflag);
% Arguments
%   transducer: A FOCUS transducer array.
%   cg: A FOCUS coordinate grid.
%   medium: A FOCUS medium.
```

```
%   ndiv: The number of integral points to use.
%   f0: Frequency of the array in Hz.
%   dflag: Display flag, 1 = display, 0 = suppress.
% Output Parameters
%   pressure: A 3-d array representing the complex pressure at each point
% Notes
%   This function prompts for action if the number of calculation points is over
%   20,796,875. This limit is based on the fact that most systems cannot process
%   an array with more than 275x275x275 elements. Users may override this by
%   editing fnm_call.m.
if nargin()< 5 || nargin() > 7
    Pressure=[];
error('fnm_call requires between 5 and 7 arguments')
end
if nargin < 6
    dflag = 0;
end
if nargin < 7
    nthreads = 8;
elseif nthreads < 1
    nthreads = 8;
end

if isstruct(xdcr)==0
    Pressure=[];
error('xdcr needs to be a struct, please create it')
end
if isstruct(cg)==0
    Pressure=[];
error('cg needs to be a struct, please use set_coordinate_grid to create it')
end
if isstruct(medium)==0
    Pressure=[];
error('medium needs to be a struct, please use define_media to create several
commonly used media')
end
if isnumeric(ndiv)==0 || ndiv<1
    Pressure=[];
```

```
error('ndiv must be greater then or equal to 1')
end
if isnumeric(f0)==0 || f0<0
    Pressure=[];
error('f0 must be greater then or equal to 0')
end

if dflag >=1
    dflag=1;
else
    dflag=0;
end

if cg.regular_grid == 1,
    nx=(cg.xmax-cg.xmin)/cg.delta(1)+1;
    ny=(cg.ymax-cg.ymin)/cg.delta(2)+1;
    nz=(cg.zmax-cg.zmin)/cg.delta(3)+1;
    nobs=nx*ny*nz;
    if nobs>20796875
sprintf('WARNING: nx= %i, my=%i, nz=%i, total elements=%i',nx,ny,nz,nobs)
        warning('Final answer may exceed the capabilities of a 32-bit system')

        %cont=input('Continue? y/n');
        %if cont=='n' || cont=='N'||cont='no' ||cont==[]
       %     Pressure=[];
       %     error('Aborted by user')
       % end
    end
end
Pressure=fnm_cw(xdcr,cg,medium,ndiv,f0,dflag,nthreads);
```

Appendix I

CMUT array fabrication

The row-column addressed CMUT arrays used in this work were fabricated by Dr. Albert Chen at the Giga-to-Nanoelectronics (G2N) Centre in Waterloo, ON and at the Toronto Nanofabrication Centre (TNFC) in Toronto, ON. The detailed fabrication process can be found in his PhD dissertation [1] but is summarized here.

A three phase process (see Figure I.1) was used to create the RC-CMUT array from a pair of silicon on insulator (SOI) wafers. First both wafers were cleaned and on the device layer of one SOI wafer an oxide insulating layer was grown. The row electrodes were separated by patterning and etching trenches through the buried oxide (BOX) layer. Next, cavities were patterned and etched into the insulation layer. After further cleaning the etched face of the SOI wafer (bottom) was fusion bonded to the device layer of the other SOI wafer (top). Following annealing, the handle and BOX layers of the top wafer were etched completely to release the device layer of the top wafer to form the CMUT membrane. The column electrodes were separated by patterning and etching trenches through the device layer of the top wafer and to the insulating layer before. The row electrodes were exposed through patterning and etching before metal contact pads were deposited.

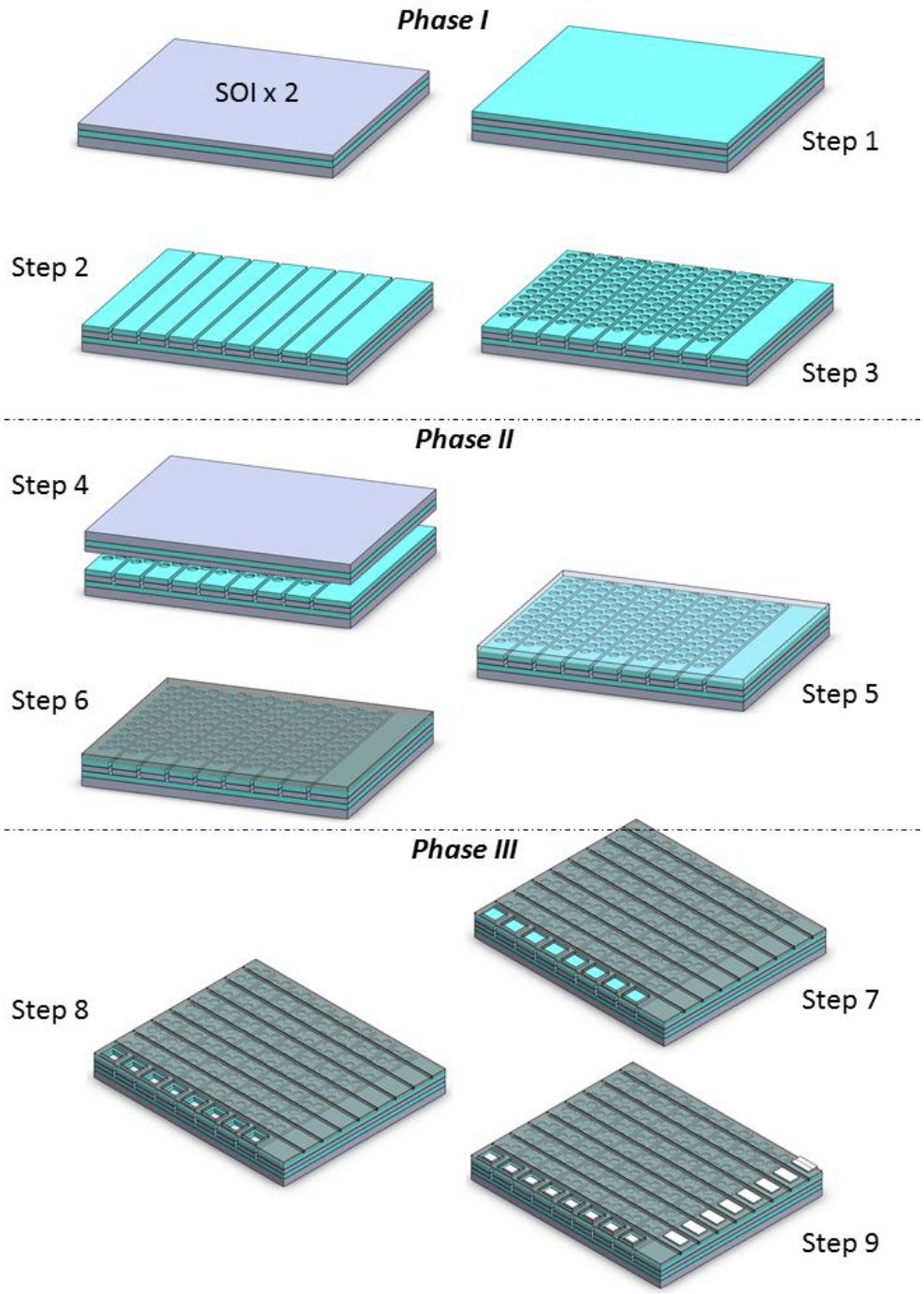

Figure I.1: Fabrication of RC-CMUT array [1]